Physics in Medicine & Biology

IPEM
Institute of Physics and Engineering in Medicine

TOPICAL REVIEW • OPEN ACCESS

Tissue mimicking materials for imaging and therapy phantoms: a review

To cite this article: Conor K McGarry *et al* 2020 *Phys. Med. Biol.* **65** 23TR01

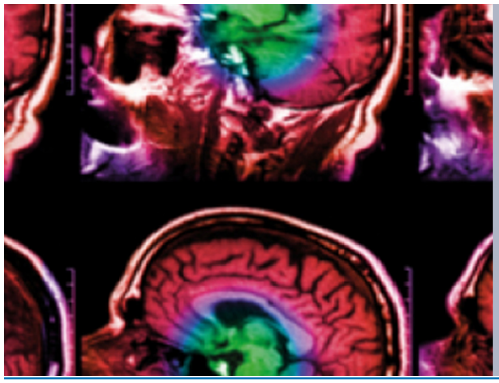

IOP Publishing Phys. Med. Biol. 65 (2020) 23TR01 https://doi.org/10.1088/1361-6560/abbd17

Physics in Medicine & Biology

IPEM Institute of Physics and Engineering in Medicine

OPEN ACCESS

RECEIVED
2 May 2020

REVISED
25 August 2020

ACCEPTED FOR PUBLICATION
30 September 2020

PUBLISHED
16 December 2020

TOPICAL REVIEW

Tissue mimicking materials for imaging and therapy phantoms: a review

Conor K McGarry[1,2], Lesley J Grattan[1], Aoife M Ivory[3], Francesca Leek[3,4], Gary P Liney[5,6,7], Yang Liu[8], Piero Miloro[3], Robba Rai[5,6,7], Andrew P Robinson[3,9,10], Albert J Shih[8], Bajram Zeqiri[3] and Catharine H Clark[3,11,12]

[1] Regional Medical Physics Service, Belfast Health and Social Care Trust, Belfast, United Kingdom
[2] The Patrick G Johnston Centre for Cancer Research, Queen's University Belfast, Belfast, United Kingdom
[3] National Physical Laboratory, Teddington TW11 0LW, United Kingdom
[4] Institute of Nuclear Medicine, University College London, London, United Kingdom
[5] South Western Sydney Clinical School, University of New South Wales, Liverpool, Australia
[6] Liverpool and Macarthur Cancer Therapy Centre, Liverpool, Australia
[7] Ingham Institute for Applied Medical Research, Liverpool, Australia
[8] Mechanical Engineering, University of Michigan, Ann Arbor, Michigan, United States of America
[9] Christie Medical Physics and Engineering (CMPE), The Christie NHS Foundation Trust, Manchester, United Kingdom
[10] Schuster Laboratory, School of Physics and Astronomy, The University of Manchester, Manchester, United Kingdom
[11] Radiotherapy Physics, University College London Hospital, London, United Kingdom
[12] Department of Medical Physics and Biomedical Engineering, University College London, London, United Kingdom

E-mail: c.mcgarry@qub.ac.uk

Keywords: tissue mimicking material, phantoms, imaging, therapy, surgery, MRI, ultrasound, CT, SPECT, PET, radiotherapy, thermal therapy, anthropomorphic

Supplementary material for this article is available online

Abstract

Tissue mimicking materials (TMMs), typically contained within phantoms, have been used for many decades in both imaging and therapeutic applications. This review investigates the specifications that are typically being used in development of the latest TMMs. The imaging modalities that have been investigated focus around CT, mammography, SPECT, PET, MRI and ultrasound. Therapeutic applications discussed within the review include radiotherapy, thermal therapy and surgical applications. A number of modalities were not reviewed including optical spectroscopy, optical imaging and planar x-rays. The emergence of image guided interventions and multimodality imaging have placed an increasing demand on the number of specifications on the latest TMMs. Material specification standards are available in some imaging areas such as ultrasound. It is recommended that this should be replicated for other imaging and therapeutic modalities. Materials used within phantoms have been reviewed for a series of imaging and therapeutic applications with the potential to become a testbed for cross-fertilization of materials across modalities. Deformation, texture, multimodality imaging and perfusion are common themes that are currently under development.

1. Introduction

Tissue mimicking materials (TMMs) have been used in widespread applications in clinical simulations and biomedical research. They are typically contained within a phantom which is defined as a model of the human body or body part. Phantoms play an invaluable role in medical research, modelling idealized tissue to evaluate clinical imaging, therapeutic device performance and medical procedures in a test environment without risk to animal or human subjects.

Reviews have recently been carried out which comprehensively discuss the manufacturing of phantoms using 3D printing with some discussion on the materials (Filippou and Tsoumpas 2018, Glick and Ikejimba 2018, Tino *et al* 2019b). One of the conclusions was that there are not enough materials to mimic all the different tissue properties (Filippou and Tsoumpas 2018) although the increasing flexibility and availability

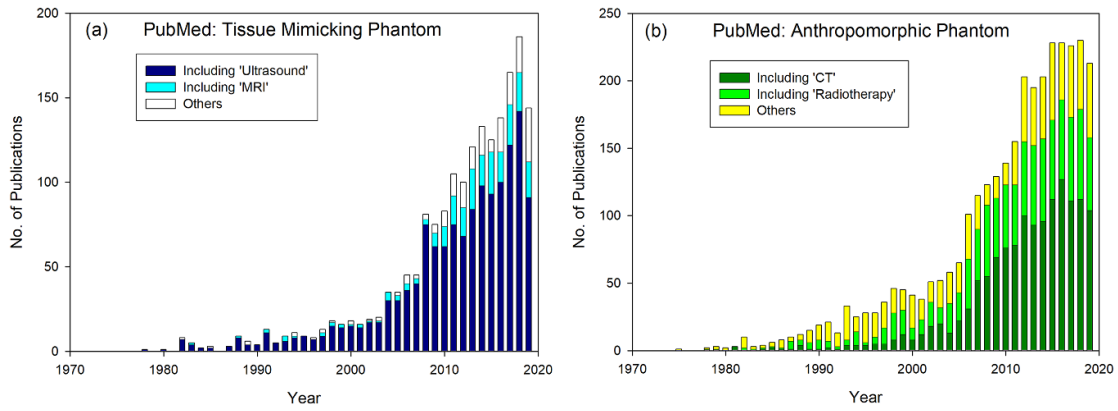

Figure 1. Research articles published per year between 1978 and 2019 in the Pubmed database with search terms (a) Tissue Mimicking Phantom and (b) Anthropomorphic Phantom.

as well as the low cost of additive manufacturing, will result in its increased use within medicine (Tino *et al* 2019b). Similarly, a surgical review has recently investigated the mechanical properties of tissue (Li *et al* 2018). With so many TMMs presented across reviews and with increasing investigations there is an urgent requirement to focus on properties of the materials used for phantoms across imaging and therapeutic modalities.

Digital or 'computational' anthropomorphic phantoms can be developed without the cost of manufacturing (Xu 2014). However, physical phantoms are more likely be used in institution-specific acquisition and procedural protocols which can vary across different manufacturers, models of equipment and applications. The material or TMMs used within physical phantoms is critical to the success of their application. Development of physical phantoms is a flourishing area of research. In Pubmed, the search term 'Tissue Mimicking Phantom' is generally referred to in ultrasound and MRI phantom development as shown in figure 1(a). With a history of more than 40 years, there is still a rise in the number of publications investigating this area. Within the sphere of CT and radiotherapy, the term TMM is not typically used, but TMMs are generally developed for 'Anthropomorphic Phantoms'. Figure 1(b) shows that a significant proportion of recent Anthropomorphic Phantoms articles are associated with ionizing imaging, such as CT, and radiotherapy. Surgery and thermal therapies are typically guided by imaging therefore often overlap both areas. With so many published and emerging articles, it is an ideal time for a review article to summarize this literature to establish the current status of this thriving research area.

This review focuses on the properties of materials designed for a wide range of medical imaging and image-guided therapeutic procedures. Results from investigations into the properties of materials, evaluated against the reference specifications are documented. The scope of this review includes lung, soft tissue and bone TMMs developed within the last 5 years as well as well characterized 'classic' materials often referred to in the literature.

2. Imaging with ionizing radiation

2.1. Specification of material

Figure 2 shows that the key parameters for material specification are the component energy dependent linear attenuation coefficients (LACs) for photoelectric absorption, Compton scattering and Rayleigh scattering for imaging and therapy with x-rays (White *et al* 1989). Physical properties may be required to mimic the physical density and the effective atomic number (Z_{eff}); radiological properties to be taken into account include the electron density and both the mass attenuation (μ/ρ) and mass–energy-absorption (μ_{en}/ρ) coefficients. It is not always necessary to match the atomic composition of the tissue(s) in question for all applications (White *et al* 1989). Indeed, the accuracy to which TMMs need to match the absorption and scattering properties of body tissue depends on the application (White *et al* 1989).

The relative difference of the LAC of tissue relative to that of water is referred to as the CT number measured in Hounsfield Unit (HU). This is often presented at a given tube voltage to characterize the tissue. The drawback to this method of defining the tissue properties is that it is only specific to a particular photon energy (Taylor *et al* 2012) and also the effect of beam hardening due to a patient's size on the HU values of lung and bone tissues can be significant (Ai *et al* 2018). In addition, measured CT numbers are somewhat dependent on scanner-related factors such as calibration and imaging protocol. A set of CT numbers, acquired at 120 kVp which were either presented by, or referenced in articles investigating TMMs over the last 5 years are presented in table 1.

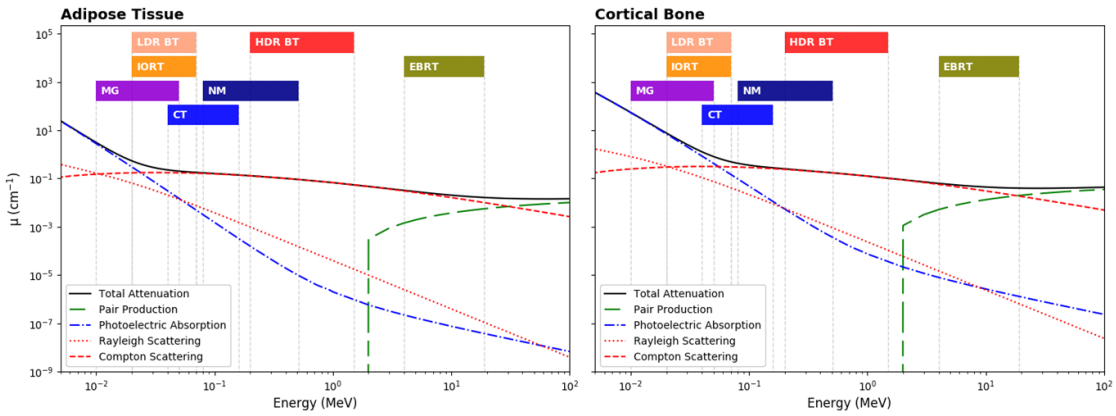

Figure 2. Scattering and absorption LACs for photons in adipose tissue (left) and cortical bone (right). The corresponding energy ranges of ionizing imaging modalities considered in this work are indicated by vertical regions . Cross section data taken from Berger *et al* (2010) with tissues definitions from White *et al* (1989). MG—Mammography, LDR—Low Dose Rate Brachytherapy, IORT—Intra-Operative Radiotherapy, CT—Computed Tomography, NM—Nuclear Medicine, HDR—High Dose Rate Brachytherapy, EBRT—External Beam Radiotherapy.

Table 1. CT properties (HU) of several common types of human tissues from prior studies. Data from (a) Woodard and White (1986), (b) Niebuhr *et al* (2016), (c) Craft and Howell (2017), (d) Konstas *et al* (2009), (e) Makris *et al* (2019), (f) Liao *et al* (2017), (g) Ehrbar *et al* (2019), (h) Sirtoli *et al* (2017), (i) Abdullah *et al* (2018), (j) Thali *et al* (2009), (k) Hamedani *et al* (2018), (l) Mohammed Ali *et al* (2018), (m) Ceh *et al* (2017), (n) Schreiber *et al* (2011), (o) Kobe *et al* (2019), (p) Bottomley *et al* (1984), (q) Hazelaar *et al* (2018), (r) Kalender (1981), (s) Brown *et al* (2015). Generally presented are mean ± standard deviation.

Human tissue	CT number (HU)
Adipose	−95 to-55[(a)], −95 ± 10[(b)]
Breast	−61 ± 47[(c)]
Heart	25 ± 25[(c)]
Brain	20 to 40[(d)], 28 ± 19[(e)]
Spleen	54[(f)]
Liver	58 ± 9, 63[(f)]
Prostate	34[(a)], 45 ± 4[(b)]
Kidney	35 ± 14[(g)], 43[(f)]
Muscle	40 to 44[(a)], 60 ± 30[(h)], 54 ± 7[(b)]
Fat	−80 ± 20[(h)], 90[(i)]
Cortical bone	1454[(j)], 930 ± 156[(k)], 1200 (111 297)[(l)], 1524[(a)], 819 ± 211[(b)], 1042 to 1754[(m)], 1000 to 3000[(n)], 1115 ± 80[(o)]
Skull/Upper jaw	996 ± 167[(e)], 934 ± 228[(e)]
Cancellous bone	262[(l)], 265 ± 135[(h)], 140 ± 170[(p)]
Lung	−378 (−605 to −97)[(q)], −862 ± 90[(c)], −950 to −550[(r)], -836 (m) and −811 (f)[(s)]

Other imaging modalities use much lower energies. Mammography is a low photon energy (<50 keV) x-ray breast imaging modality. At these energies the adipose and glandular tissue components of the breast need to be considered separately when developing suitable breast phantoms (White *et al* 1989). Dedicated breast CT (bCT) typically use higher photon energies up to approx. 100 keV. According to ICRU 44, a single material may be adequate to represent both tissue types above 50 keV (White *et al* 1989). For mammography (and bCT) material characterization is normally specified using the LAC defined over the clinical energy range. For experimental phase contrast mammography, the refractive index decrement (δ) is used for material specification (Esposito *et al* 2019).

Phantoms for nuclear medicine imaging have historically focused on constraining radioactive material in predefined geometries, with a focus on quality control and performance optimization of imaging systems. The majority of these phantoms are designed to contain solutions of radionuclides used for single photon emission computed tomography (SPECT) or positron emission tomography (PET). The relatively short half-life of most isotopes used in nuclear medicine (typically < 1 week) adds an additional requirement that phantoms easily allow regular safe addition and removal of radionuclide solution. Subsequent developments have focused on anthropomorphic phantoms that provide more realistic geometries which better represent clinically observed activity distributions.

These unique requirements of nuclear medicine phantoms, in comparison to other ionizing imaging modalities, has led to a general focus on developing phantoms that can safely contain radionuclide solutions,

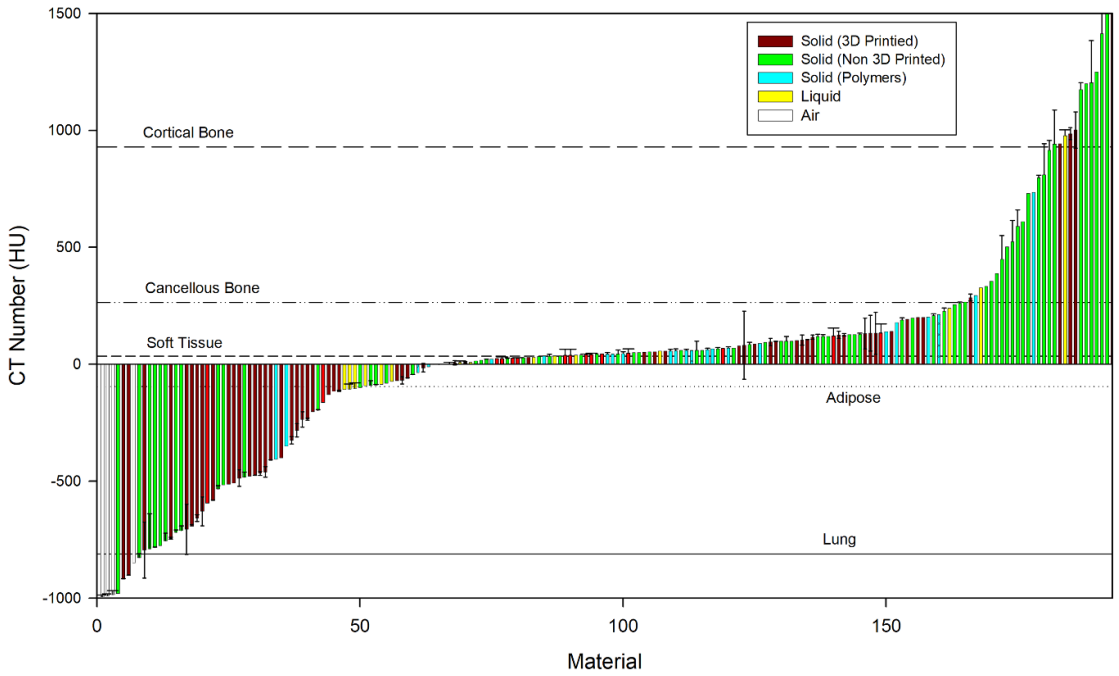

Figure 3. Waterfall plot showing the CT numbers for a variety of materials including solids (3D printed, non-3D printed or Polymers), liquids and air. Error bars represent the standard deviations. Reference lines are shown from typical values in .table 1.

with only secondary consideration of specific tissue equivalence. As with x-ray, CT and mammography imaging the key parameter for tissue material specification is the LAC of the tissue of interest. This is now increasingly important as SPECT and PET imaging is routinely performed with sequential CT imaging for attenuation correction. The energy of photons detected in nuclear medicine imaging is isotope dependent with a nominal range of ~80–511 keV (see figure 2), with 140 keV (^{99m}Tc) being prevalent for clinical SPECT imaging and 511 keV positron annihilation photons for PET.

2.2. CT

2.2.1. Review of materials

2.2.1.1. Commercial phantoms

TMMs used in CT imaging including resins, gels, plastics and a variety of 3D printing materials were presented in (Bliznakova *et al* 2018) and in the recent AAPM Task Group Report 233 (Samei *et al* 2019) with established whole body phantoms such as the resin-based Rando (The Phantom Laboratory), ATOM (CIRS, US), Leeds (Leeds Test Objects, UK), KYOTO (KYOTO Kagaku Co, Japan) phantoms discussed. Although the TMMs within commercial phantoms are typically proprietary, some do present the mass and electron density as well as comparison with recalculated LACs (ATOM® Dosimetry Phantoms Models 701–706 White Paper, https://www.cirsinc.com/products/all/33/atom-dosimetry-verification-phantoms/) at time of publication compared against reference data (Snyder *et al* 1975, Hammerstein *et al* 1979, Woodard and White 1986). Commercial calibration HU phantoms utilize solid resin or liquid TMM inserts (Dancewicz *et al* 2017).

2.2.1.2. In-house phantoms

Articles on in-house phantom materials were retrieved from Google Scholar and Pubmed searches of 'Anthropomorphic Phantom Development CT' over the past 5 years. Articles were excluded if they were investigating computational phantoms or referring only to optimization of imaging parameters, radiation protection or radiotherapy. Other articles have also been sourced from recent reviews on 3D printing (Filippou and Tsoumpas 2018, Tino *et al* 2019b) and also reviews including motion management phantoms (Bertholet *et al* 2019). Figure 3 shows that at least 200 materials have been utilized to mimic tissue over the past 5 years, reporting the HU, typically at 120 kVp. The source data is also presented in supplementary table 1 (available online at https://stacks.iop.org/PMB/65/23TR01/mmedia) with direct references to patient data, supplementary table 2 with direct reference to phantom data and also in supplementary table 3 without direct references.

2.2.1.3. Soft tissue

Materials with particular soft tissue properties have been widely investigated for CT, motivated by the increasing number of investigations into deformable and multi-modality phantoms. Solids such as Polymethyl methacrylate (PMMA) and resins (Perrin *et al* 2017, Mohammed Ali *et al* 2018), and 3D printed materials (Filippou and Tsoumpas 2018, Tino *et al* 2019b) can be used to mimic soft tissue although printed shells filled with liquids or polymers, as shown in figure 3, have become more prevalent with the increasing requirement for MR-CT visualization (section 5.1) and deformation. Liquids mixed with varying concentrations of contrast agents have allowed the development of liquid phantoms with similar imaging contrast properties to a variety of organs and tissues (Niebuhr *et al* 2016, 2019, Fitzgerald *et al* 2017, Abdullah *et al* 2018). Liquids have the advantage that they can fill voids within manufactured phantoms including deformable balloon-like materials (Niebuhr *et al* 2016, 2019, Abdullah *et al* 2018). Gelatin materials have been shown to have similar properties to soft tissue (Gallas *et al* 2015, Steinmann *et al* 2018, Abdullah *et al* 2018) albeit with radiological changes observed over time; although methods to preserve these properties have been developed (Steinmann *et al* 2018, Niebuhr *et al* 2019). Synthetic polymers, such as polyvinyl chloride (PVC) and silicone, do not have water within the structure and therefore generally have more stable properties, as well as a longer shelf life (Li *et al* 2015b). PVC with different softener ratios can result in different HU, allowing the creation of a calibration curve to replicate many organ densities (Liao *et al* 2017, Steinmann *et al* 2018, He *et al* 2019b). Silicone and urethane materials have been used to investigate soft tissue with different silicone types and mixes giving possibilities to tune the concentrations to mimic the relevant HU (Kadoya *et al* 2017, Steinmann *et al* 2018, Hazelaar *et al* 2018, Ehrbar *et al* 2019).

2.2.1.4. Bone

A number of materials have simulated bone. Metal materials infused into 3D printing filament have led to high density materials, although the HU have been much higher than typical cortical bone material, leading to artefacts in some cases (Ceh *et al* 2017, Dancewicz *et al* 2017). However, acrylonitrile butadiene styrene (ABS) pellets doped with barium sulphate are showing promise (Hamedani *et al* 2018) as are other materials (Perrin *et al* 2017, Makris *et al* 2019) although their properties were not described. Gypsum is a dense material that has been widely used for cortical bone (Niebuhr *et al* 2016, 2019, Hazelaar *et al* 2018, Mohammed Ali *et al* 2018). Many other materials have been used for inner bone including Vaseline doped with dipotassium hydrogen phosphate (Niebuhr *et al* 2016, 2019), urethane based materials (Cunningham *et al* 2019, Kobe *et al* 2019), modified resins (He *et al* 2019b) and Teflon® (Hernandez-Giron *et al* 2019). Iodine has a high atomic number and can result in HU similar to cortical bone. This has been used as a solution (Abdullah *et al* 2018) and also placed within ink to print with varying grey-levels onto paper to create a phantom (Jahnke *et al* 2016).

2.2.1.5. Lung

Air has been used to simulate lungs (Craft and Howell 2017, Abdullah *et al* 2018, Hernandez-Giron *et al* 2019) although this is an underestimation of patient lung densities (Kalender 1981, Brown *et al* 2015). Polyurethane (PU) foam has been used as a lung substitute (Perrin *et al* 2017) with (Shin *et al* 2020) adding contrast agents to the foam to increase the density. This material has the advantage that the density varies following compression, which is desirable for dynamic inhale/exhale investigations. The most investigated method of lung mimicking has been through varying the 3D printed materials and infill patterns (Madamesila *et al* 2016, Dancewicz *et al* 2017, Hazelaar *et al* 2018, Hong *et al* 2020). These have typically used rectilinear patterns although other patterns have been investigated (Madamesila *et al* 2016, Dancewicz *et al* 2017) with novel Gyroid structure providing improved isotropy at different scanning orientations (Tino *et al* 2019a).

2.2.2. Limitations

The supplementary tables 1–3 show that density, effective atomic numbers (Z_{eff}), material composition (w%) or LAC curves have also been presented. These are typically compared with values generated from ICRU 44 (White *et al* 1989) or ICRU 46 (White *et al* 1992). Figure 4(a) shows how the linear attenuation curve changes with energy, calculated using a simulation package can be plotted with the CT numbers at different energies for liquid TMMs (Fitzgerald *et al* 2017). A limitation in some of the literature is that these material properties are not always presented. These properties can be important for applications such as radiotherapy where information such as composition can be important for validation of modelling the treatment within planning systems as discussed in section 6.

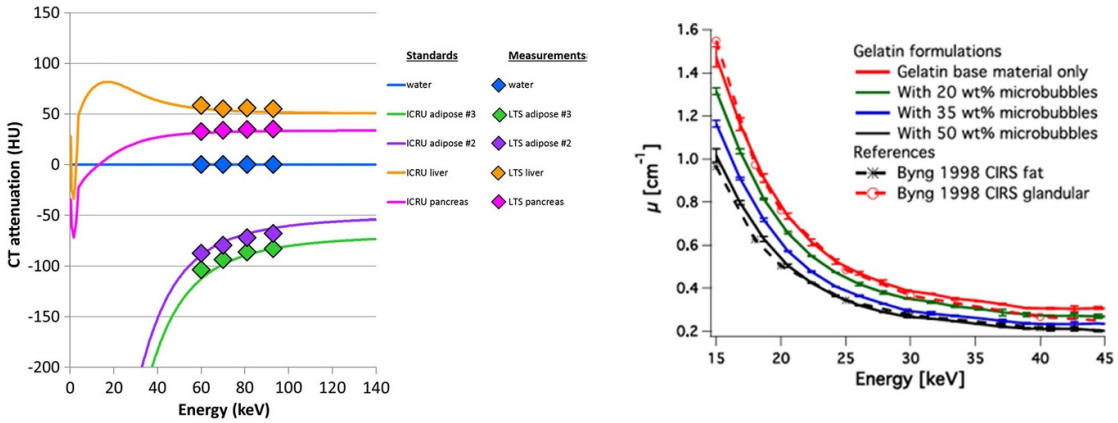

Figure 4. (a) Plot of calculated discrete-energy CT attenuation of selected ICRU tissues (lines) and the measured CT attenuation of the physically produced liquid tissue substitute (LTS) materials (diamonds). Figure license: Fitzgerald *et al* (2017). John Wiley & Sons. © 2017 American Association of Physicists in Medicine. (b) Linear attenuation coefficient of four gelatin-based phantom materials mimicking x-ray attenuation properties of breast glandular and adipose tissues. Reference materials used are CIRS phantoms. Figure license: Reproduced from Dahal *et al* (2018). Not subject to copyright in the USA. Contribution of US Food and Drug Administration. All rights reserved.

2.2.3. Latest developments

2.2.3.1. Texture

In light of the availability and increasing clinical utilization of new CT technologies, it is particularly important to assess image quality using task-specific metrics that are more relevant to predicting the performance of a CT system for specific clinical imaging protocols (Samei *et al* 2019) . The nonlinear nature of emerging reconstruction algorithms results in object-dependent resolution and noise performances. Thus, traditional image quality metrics, such as contrast-to-noise ratio, are not always adequate indicators of clinical imaging performance, instead a requirement for phantoms with 'anatomical' texture and structures (i.e. heterogeneous background) has been suggested e.g. the Lungman phantom from Kyoto Kagaku (Jin *et al* 2019), with Mercury texture inserts (Samei *et al* 2019). With this recent suggestion from AAPM TG 233 that texture phantoms are preferred (Samei *et al* 2019), it is certain that 3D printing will play an important role in the development of heterogeneous phantoms.

With the evolution of advanced image analysis through radiomics, methodologies to ensure the best possible repeatability and reproducibility of features will require more sophisticated phantoms with detailed texture (Kalendralis *et al* 2019). This will place further emphasis on material development for TMMs (Plautz *et al* 2019). A recent study showed that combinations of liquids, gels and solids are typically used for heterogeneous phantoms and that these 'standardization objects' could be critical to ensuring stable radiomics models across institutions (Valladares *et al* 2020).

2.2.3.2. Multi-energy CT

Multi-energy CT has several key applications including enhanced imaging using contrast media and associated quantification of contrast, identification of materials via decomposition, and measurement of electron density for radiotherapy planning applications. Inserts made of materials chosen to represent tissues and contrast agents in either semi-anthropomorphic phantoms (Ehn *et al* 2018) or other geometric phantoms (Ueguchi *et al* 2018) have been used. To determine the accuracy of identifying materials such as calcium compounds and uric acid for diagnosis of renal stones for example, human tissue samples have been utilized within phantoms (Große Hokamp *et al* 2019). Mileto *et al* (2016) produced a phantom containing iodine to simulate an enhanced kidney for example, with solid enhancing lesions. Phantoms made from an epoxy resin with material inserts designed to be spectrally equivalent across the range of virtual energies simulated in dual energy CT have been developed by Nute *et al* (2019). The insert materials included iron (III) oxide for blood, calcium carbonate for calcification and iodobenzene added to epoxy resin at various concentrations for contrast agent.

2.2.3.3. Cardiac CT

Cardiac CT imaging phantoms are typically designed to replicate a selection of the possible features, depending on the clinical question to be investigated. Features may include heart beat movement, perfusion, x-ray attenuation, scatter, and features indicative of disease such as plaques or stenoses. It is not usually possible, or indeed necessary, to combine all these features into a single anthropomorphic phantom.

Boltz *et al* (2010) have developed a comprehensive beating cardiac phantom for an ECG system to 'reasonably duplicate an average patient's cardiac CT exam in terms of scatter, cardiac tissue densities, coronary size, motion, heart rate and contrast material.' The cardiac phantom is designed to fit into a thorax phantom containing TMMs. Attenuation of blood and tissues (soft tissue, bone, lung, myocardium, blood and contrast enhanced blood) was measured and compared with the average from 200 coronary CT angiography patients, providing a useful set of reference values for cardiac CT imaging.

A 3D printed cardiac insert phantom for use with an anthropomorphic thorax phantom was fabricated from ABS by (Abdullah *et al* 2018), with designated spaces filled with tissue-like materials. Comparison of CT numbers were made between patient images and the materials within the printed cardiac phantom when inserted into the thorax phantom. Commercial cardiac phantoms (Cardio CT, Sim4Dcardio with coronary artery phantom, QRM, Germany), have been designed to replicate thoracic tissues and to simulate motion of the coronary arteries. These have recently been used to investigate the accuracy of measurements of coronary stenosis (Papadakis *et al* 2020). Coronary artery stenosis have been mimicked using water-filled tubing of various diameters within a flow phantom (Funama *et al* 2016).

2.2.3.4. 4D imaging and deformation

4D CT has increasingly been used to define tumour motion in radiotherapy and is utilized in diagnostic radiology to investigate joint problems, the cardiac cycle and parathyroid washout of contrast. Increasingly, there is a desire to capture motion and deformation within CT and CBCT, and therefore materials with deformable properties are starting to be developed (Liao *et al* 2017, He *et al* 2019b). A description of dynamic anthropomorphic phantoms has been recently presented in a review by Bertholet *et al* (2019). Materials such as Silicone have been used for the abdomen, with HU values similar to those measured from a patient (Ehrbar *et al* 2019). The need for deformation places new requirements to present or test the mechanical properties of TMMs such as shore hardness (Gallas *et al* 2015, Kadoya *et al* 2017), Poison ratios and elastic moduli (Liao *et al* 2017, He *et al* 2019b). Increasingly, these phantoms have a requirement to be visible on other complementary imaging modalities such as ultrasound and MRI as discussed in section 5.

2.3. Mammography and breast CT

2.3.1. Review of materials

In general, phantoms in diagnostic radiology modalities are developed for the purposes of assessing patient absorbed dose and/or assessing imaging performance. However, recent developments in breast imaging have tended to concentrate on the latter in light of new imaging developments such as digital breast tomosynthesis (DBT), contrast-enhanced/dual energy mammography and breast CT. In particular, the emergence of DBT has driven development away from homogeneous phantoms towards phantoms with textured backgrounds—a feature that is necessary for assessing DBT. DBT is a pseudo-3D imaging technique specifically designed to remove overlying anatomical structure from regions of interest and so, in addition, many new phantoms are being designed with breast-like structure in three dimensions. These factors have in turn driven the choice of phantom manufacturing method and materials.

Within breast phantom development, ICRU 44 (White *et al* 1989), Hammerstein *et al* (1979), and Johns and Yaffe (1987) are typically utilized as standard references, providing elemental composition of breast tissues from which the LACs are calculated. Another commonly used validation approach is to conduct a side-by-side comparison with a material which has been established as a suitable tissue substitute. The commercial CIRS adipose and glandular tissue equivalent resins (cirsinc.com) have often been used as a ground truth for this purpose as shown in figure 4(b). Their accuracy as breast tissue equivalent materials was demonstrated (Byng *et al* 1998) by comparison with published data (Hammerstein *et al* 1979).

2.3.1.1. Commercial phantoms

A range of solid commercial phantoms designed to replicate the attenuation of various glandularities of breast tissue is available for optimization and quality assurance purposes. Whilst some of these phantoms very accurately replicate the attenuation of breast tissues at mammographic energies, limitations centre on the fact that most are either homogeneous or only provide a rough approximation of breast tissue structure. The CIRS BR3D Model 020 phantom (cirsinc.com) uses two resin tissue-equivalent materials which mimic 100% glandular and adipose tissue swirled together in a set of slabs to provide a range of heterogeneous backgrounds. Voxmam from Leeds Test Objects (leedstestobjects.com) has an unspecified textured background which is claimed to simulate breast tissue. These heterogeneous phantoms represent a step forward in breast phantom design, but work continues towards more anthropomorphic representation.

2.3.1.2. In-house phantoms

Articles from PubMed from 2015 to mid-2020 with criteria of 'mammography' and 'anthropomorphic' or 'dual-energy', plus earlier articles considered to provide key reference values, and articles cited in review papers were referenced in this section. Only articles relating to physical phantoms were included. Almost all of the recent physical phantoms aim to match the attenuation properties of the adipose and glandular breast tissues and, in addition, to reproduce the heterogeneous tissue structure. With regard to this second objective, the in-house phantoms fall into two categories: those with a non-anatomical representation of breast texture, and those which are based on either computational breast models or x-ray images of real breasts and aim to provide x-ray images of the phantom which are similar to those of a real breast. The textured, but non-anatomical, representation of breast tissue is typically produced using a 'spheres in water' design. The texture of phantom images is quantified using the beta-index from Noise Power Spectrum measurements and compared with that obtained from breast images (Cockmartin *et al* 2017). A recent example of this type of phantom is given in section 1 of table 2. Phantoms which aim to replicate a real breast are listed in section 2 of table 2. Where possible, the table indicates the percentage of adipose or glandular breast tissue simulated by the material. Most are produced using 3D printing methods and can be compared with their source file for accuracy. One phantom was produced by 2D printing using iodinated ink on parchment paper (Ikejimba *et al* 2017). Several designs employ printing for one tissue type and infill the resulting cavity with the other tissue substitute (Kiarashi *et al* 2015, Mainprize *et al* 2018). Variable height phantoms (Badal *et al* 2018, Schopphoven *et al* 2019) have been made for 2D mammography from clinical images, where the thickness of printed material relates to the spatial attenuation of the breast tissue. Suitable materials to produce low-cost homogeneous phantoms include 3D wood (Alssabbagh *et al* 2017) and a paraffin and boric acid base mix (Cubukcu and Yücel 2016).

Phantoms for use with dual energy mammography need to be sufficiently compositionally accurate to calibrate a dual energy system such that it can decompose the breast into its constituent components, and so quantify breast density. It was found that the commercial glandular and adipose resin phantoms were inadequate for calibration purposes. Instead alternative liquid phantoms (Cho *et al* 2017) were used, which more closely replicated the chemical composition of the breast tissues (section 3 of table 2). Liquid phantoms can be difficult to handle, and so conversion coefficients intended for use with solid water and adipose equivalent phantoms are provided (Cho *et al* 2017). Hwang *et al* 2018 have designed iodine in PMMA phantoms which were used together with the CIRS 'swirl' heterogeneous phantom to demonstrate a method of quantifying iodine concentration in clinical dual energy contrast-enhanced subtraction images.

For higher x-ray photon energies used in breast CT and the experimental modality of phase contrast imaging, both heterogeneous and homogeneous breast phantoms are being developed. A number of materials, including ten polymer resins have been investigated by Ivanov *et al* (2018) for photon energies of 30 keV, 45 kev and 60 keV. These materials were also assessed for use in phase contrast imaging (Esposito *et al* 2019). Gel based breast phantoms have been designed for use across several imaging modalities including CT, MRI and ultrasound (Ruschin *et al* 2016, Coulaud *et al* 2018). They have the advantage of being deformable and have been employed in validating deformable image registration algorithms (Ruschin *et al* 2016).

2.3.2. Limitations

A number of limitations of in-house phantoms are highlighted both in the references in table 2 and in review articles (Glick and Ikejimba 2018, Ivanov *et al* 2018, Bliznakova *et al* 2018). Whilst it has been reported that 3D printing will be able to mimic breast tissue composition and texture with suitable accuracy, challenges still exist. Currently, two of the main challenges associated with this method are the difficulty in finding a suitable adipose tissue equivalent material (Rossman *et al* 2019), and producing a printable structure design with the required resolution. At present, structural compromises are necessary to facilitate the printing process. (Badal *et al* 2018, Schopphoven *et al* 2019) Also, there are challenges associated with printing multi-material phantoms (Esposito *et al* 2019) which is of particular relevance for breast phantoms.

2.3.3. Latest developments

2.3.3.1. Texture

There is an urgent need for phantoms which are suitable for use with DBT, both for a QA programme and for optimization purposes. This is driving the development of textured phantoms discussed in the previous section. 3D printing appears to be the most promising method for producing an accurate and reproducible representation of breast texture and attenuation. Two of the most recent refinements to be employed are the use of modified printers to improve resolution and the use of dithering to produce smooth transitions between materials (Rossman *et al* 2019).

Table 2. Mammography and higher energy x-ray breast imaging—Linear Attenuation Coefficient (LAC) is quoted here for a single energy although most references provide data across the clinical energy range (a) Cockmartin *et al* (2017), (b) Rossman *et al* (2019), (c) Mainprize *et al* (2018), (d) Badal *et al* (2018), (e) Dahal *et al* (2018), (f) Ikejimba *et al* (2017), (g) Kiarashi *et al* (2015), (h) Cho *et al* (2017), (j) Coulaud *et al* (2018),. For reference material: (i) Johns and Yaffe (1987), (ii) Fredenberg *et al* (2016), (iii) Hubbell and Seltzer (2004), (iv) Hammerstein *et al* (1979), (v) Byng *et al* (1998). DM = digital mammography, DBT = digital breast tomosynthesis, CE = contrast enhanced, DE = dual energy, bCT = breast CT. * indicates 3D printed material.

Modality	Energy keV (ave)	Patient or Reference Material	LAC (cm^{-1})	Simulated material	LAC (cm^{-1})
Section 1: Textured mammography phantom, non-anatomical representation					
DM, DBT[(a)]	20	Breast cancerous[i]	0.84	Next*	0.83
		Water[ii] (glandular 100%)	0.80	CIRS BR gland 2066-A-2	0.79
		PMMA[iii]	0.68	PMMA sphere	0.68
		50% adipose—50% glandular tissue[iv]	0.62	75% PMMA + 25% water	0.71
Section 2: Textured mammography phantoms, anatomical representation					
(CE)DM, DBT[(b)]	20	CIRS glandular 100% (measured)	0.67	VeroPureWhite (glandular 92%)	0.65
				Zinc acetate doped Jf Flexible (3 wt %) (glandular 100%)	0.68
				Tungsten-doped Jf Flexible* (1.6 wt %) (glandular 140%)	0.75
		CIRS adipose 100% (measured)	0.44	Jf Flexible* (adipose 64%)	0.53
				TangoPlus* (adipose 64%)	0.56
DM, DBT, bCT[(c)]	20	Glandular tissue[i]	0.80	Water (glandular ~ 90%)	0.76
		Adipose tissue[i]	0.46	Polyamide-12 (adipose ~ 90%)	0.50
DM[(d)]	20	PMMA (measured)	0.65	VeroMagenta* (solid)	0.64
				TangoBlackPlus* (flexible)	0.60
DM, DBT, CT[(e)]	20	CIRS glandular 100%[v]	0.76	Gelatin in glycerine solution (glandular 100%)	0.79
		CIRS adipose 100%[v]	0.51	Addition of expanded thermoplastic microbubbles (50 wt %) (adipose 100%)	0.54
		Glandular tissue[iv]	0.74	Parchment paper + iodinated ink (printer ink with 25% added iohexol by volume) (glandular 100%)	0.83
DM, DBT[(f)]	20				
		Adipose tissue[iv]	0.48	Parchment paper (adipose 100%)	0.61
DM, DBT[(g)]	19	CIRS glandular 64% (measured)	0.66	TangoGray* (flexible) (glandular 64%)	0.66
				VeroWhite* (rigid) (glandular 64%)	0.66
		CIRS adipose 64% (measured)	0.59	TangoPlus* (flexible) (adipose 64%)	0.59
		CIRS adipose 100% (measured)	0.49	Beeswax (adipose 100%)	0.49
				Urethane-based polymer water simulant (QuickWater for Silks^{TM}) (adipose 100%)	0.50
Section 3: Dual energy mammography phantom					
DEDM[(h)]	20	Phantom used to determine % water composition of post-mortem breasts (Ave RMS error water)	3.1%	Water	0.80
				Glyceryl trioleate (Lipid 100%)	0.46
Section 4: Higher energy phantoms/materials					
CT, MRI[(j)]	≥ 50	'Breast' (ICRU 44) @ 50 keV	0.22	EasyDosit (hydrogel of gelatin and disaccharide), Solifer (iron II), water @50 keV	0.23

2.3.3.2. Lesions

Much work has been done in developing mathematical models of clinical breast lesions, and a database containing many examples has recently been established (Bliznakova *et al* 2019). However there has been less success to date in realizing these in a physical form which can be inserted or included in a physical breast phantom. Some examples of realistic lesions inserted into phantoms include microcalcifications made from calcium hydroxyapatite, which is associated with malignant lesions found in clinical breast cancers (Ikejimba *et al* 2019), and 3D printed spiculated and non-spiculated masses from a material closely matching the attenuation of cancerous breast tissue at mammographic energies (Cockmartin *et al* 2017). Rossman *et al* (2019) have recently introduced a new development by fabricating iodinated masses via 3D printing.

2.4. Nuclear medicine

2.4.1. Review of materials

Articles on nuclear medicine phantom materials were retrieved from a Pubmed search of '(Anthropomorphic Phantom) AND (SPECT OR PET OR MRT OR TRT OR radionuclide OR radioactive OR radioactivity)' over the past 5 years. Other articles have also been sourced from recent reviews on 3D printing (Filippou and Tsoumpas 2018, Tino *et al* 2019b).

2.4.1.1. Commercial phantom materials

When considering tissue mimicking properties commercial nuclear medicine phantoms have been divided into four groups: general purpose liquid filled phantoms, often with simple geometrical inserts; specialized phantom inserts and accessories, designed to adapt general purpose phantoms to be more clinically representative; solid radioactive phantoms, primarily using longer lived surrogate radioactive sources for QC; and specialized anthropomorphic and single purpose phantoms.

2.4.1.2. General purpose liquid filled phantoms

Since the design was first published in Jaszczak *et al* (1977) cylindrical and elliptical forms of the 'Jaszczak' phantom have become the standard nuclear medicine phantom. Multiple commercial versions of the phantom (often with a range of fillable and solid inserts with basic geometries) are available, commonly constructed from polymethlmethacrylate (PMMA) as a water equivalent material (*Data Spectrum Corporation, Biodex Medical Systems Products*). The NEMA IEC PET body phantom (NEMA 2007) and other common anthropomorphic phantoms (Hoffman *et al* 1991) also primarily use PMMA to reproduce a LAC close to water rather than any tissue specific properties.

2.4.1.3. Specialized phantom inserts and accessories

The NEMA NU 2–2007 standard specifies the inclusion of an additional cylindrical insert filled with a low atomic number material with an average density of 0.3 ± 0.1 kg m^{-3} to simulate the attenuation of lung (NEMA 2007). Additional inserts for elliptical Jaszczak and torso phantoms add lung chambers which are filled with water containing solid Styrofoam® beads (*Data Spectrum Corporation Products*), simulating lung tissue with density of ~0.3 kg m^{-3} . In addition solid Teflon® rod inserts (*Data Spectrum Corporation, Biodex Medical Systems*) are also available for these phantoms to simulate the spine. Uptake of radionuclide within the spine column can be simulated with a bone equivalent liquid solution (*Data Spectrum Corporation*), commonly based on a solution of K_2HPO_4 calibrated to give a LAC nearly equivalent to skeletal cranium bone over a range of energies from 50 keV to 600 keV (de Dreuille *et al* 1997).

2.4.1.4. Solid radioactive phantoms

The use of solid sources made from encapsulated solutions of radionuclides and epoxy solution for PET-CT QC is now commonplace, however the exact material composition of these sources is often proprietary. Zimmerman and Cessna (2010) and Zimmerman *et al* (2014) have reported on the manufacture of traceable solid ^{68}Ge sources for PET calibration from a solution of $^{68}GeCl_4$ combined with Stycast 1264A/B epoxy (Emerson and Cuming, US) where they note that the magnitude of the corrections for differences in attenuation between the epoxy filled phantom and its liquid filled counterpart could result in additional uncertainties. Similar techniques were also applied in Zimmerman *et al* (2013) to the production of ^{133}Ba sources as a surrogate for ^{131}I imaging.

2.4.1.5. Anthropomorphic phantoms

A range of radiation equivalent and anatomically correct anthropomorphic phantoms for nuclear medicine are available (*Radiology Support Devices Inc*). These phantoms are widely referenced however limited details of the tissue equivalence of materials used in these phantoms is provided (Cheung and Sawant 2015). It is noted that for the head phantom the nasal cavity and maxillary sinuses are filled with foam with a mass density of 0.23 kg m^{-3} (*Radiology Support Devices Inc*).

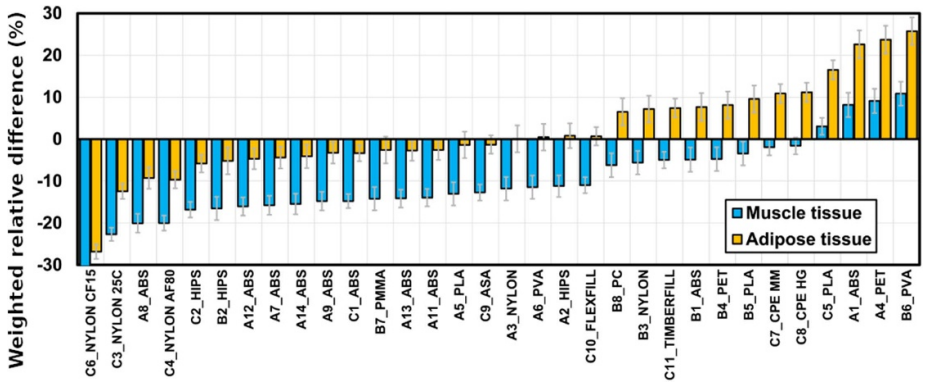

Figure 5. Weighted average between LACs of the printed samples and soft tissues—sorted from the largest negative difference. Material acronyms: ABS (Acrylonitrile butadiene styrene), ASA (Acrylonitrile styrene acrylate), CPE MM (Chlorinated polyethylene, white), CPE HG (Chlorinated polyethylene, natural), FLEXFILL 98A (Thermoplastic polyurethane), HIPS (High impact polystyrene), PC (Polycarbonate), PET (Polyethylene terephthalate), PLA (Polylactic acid), PMMA (Polymethyl methacrylate), PVA (Polyvinyl alcohol), TIMBERFILL (Biodegradable material based on wood). Figure license: Reproduced from Solc *et al* (2018). © 2018 The Author(s). Published by IOP Publishing Ltd on behalf of Sissa Medialab. CC BY 3.0.

2.4.1.6. In-house phantom materials

Widespread access to additive manufacturing techniques (3D printing) in academic and clinical departments has led to a rapid increase in their use in nuclear medicine. This has corresponded to over 20 papers being published in the last 5 years as reported on Pub Med when searching for '3D printing nuclear medicine'. However, many of the materials used have not been characterized and tested to the same extent as commercial tissue equivalent materials and in fact half of the research articles reviewed in (Filippou and Tsoumpas 2018) do not mention the properties of the materials. The predominant focus of these publications has instead been accurate reproduction of 3D spatial distributions of radionuclide solution (Robinson *et al* 2016).

The specific tissue equivalence of 3D printed plastics for nuclear medicine imaging is considered in (Solc *et al* 2018). Measurements were made of the LAC, and HU of 3D-printed test samples of plastic materials. A comparison to values of skeletal muscle tissue and adipose tissue (White *et al* 1989) was made for 32 samples of 12 different materials. The testing was conducted at three photon energies (60 keV, 112 keV, 344 keV) appropriate for quantitative imaging in radionuclide therapy. The relative difference between μ for the samples and the given soft tissue, averaged over each of three photon energies are shown in figure 5.

Gear *et al* (2016) demonstrated the use of powder deposition printing to produce an anthropomorphic torso phantom for quantitative imaging analysis of SIRT (selective internal radiation therapy). In contrast to the majority of applications of 3D printing in nuclear medicine, the torso was constructed entirely from VeroWhite Plus FullCure 835 (Stratasys Ltd., Eden Prairie, MN, USA) rather than being water filled. The HU value of VeroClear was reported as 127 $\pm$ 15 and LACs corresponding to the major emissions from ^{99m}Tc, ^{111}In, ^{131}I and 511 keV photons were also reported.

Subresolution sandwich phantoms for SPECT and PET combining multiple layers of 2D activity distributions, produced with a conventional ink jet printer and radioactive ink solution, with layers of attenuating material, such as PMMA have been developed (Berthon *et al* 2015). The majority of these publications do not consider the tissue equivalence of the materials. Taylor *et al* (2018) report on the development of a 3D printed subresolution sandwich phantom for validation of brain SPECT analysis similar to that previously described (Negus *et al* 2016). The phantom incorporates thin slabs of attenuating material generated through additive manufacturing, and paper sheets with radioactive ink patterns printed on their surface. Soft tissue was manufactured from standard polylactic acid filament printed at 85% infill density and the skull was created using polylactic acid doped with bronze (20% by weight). The printed soft tissue and bone structures had a LAC of 0.168/cm and 0.225/cm respectively at 140 keV.

Realistic phantoms for thyroid imaging require a range of tissue equivalent materials to accurately model the thyroid, trachea and neck. Beaumont *et al* (2017) produced a 3D printed set of age-specific thyroid phantoms (5-, 10-, 15-year old and adult) by taking into account material properties to simulate the attenuation of biological tissues. The phantoms were printed using Objet VeroClear and VeroWhite photo resins with the physical thickness of the materials adjusted so that the attenuation equalled the value of a given tissue of interest (adipose tissue, the spinal cord and the cervical spine). They report a 9% difference between the measured LAC at 356 keV for VeroClear and adipose tissue; and a 18% difference between VeroWhite and cervical spine. Amin *et al* (2020) report the fabrication of an anthropomorphic thyroid-neck phantom made from paraffin wax and sodium chloride (NaCl) compounds. Soft tissue and bone equivalent

materials were prepared using a combination of 75% paraffin wax, and 25% NaCl and 60% paraffin wax and 40% NaCl, respectively. The attenuation coefficients of the materials were evaluated for energies ranging from 59.54 keV to 1330 keV. The relative percentage difference for bone tissue (between 662 keV and 1500 keV) was below 5% when compared to White *et al* (1989). The maximum relative percentage difference reported for soft tissue equivalent material was 7.46%.

2.4.2. Limitations

Many of the historic limitations of TMMs discussed in the previous section can be addressed for a single combination of radionuclide and tissue with custom materials. However, the wide range of emission energies and particle types used in nuclear medicine makes the use of a single TMM for all nuclear medicine imaging problamatic. Furthermore, depending on the adminstered radionuclide, SPECT and PET scanners may detect secondary radiation emissions, produced from the interaction of primary decay radiation in the surrounding tissue (for example bremsstrahlung production or positron annihilation). In the case of PET imaging and SPECT bremsstrahlung imaging these secondary radiations are the principal emissions detected for imaging. TMMs for nuclear medicine imaging should therefore ideally reproduce the interaction cross sections for the production of secondary radiations and not just the bulk attenuation and scattering properties. Identification of suitable analog materials with physical properties that allow the production of phantoms is a complex problem to solve and to date this approach has not been widely adopted in the field.

2.4.3. Latest developments

2.4.3.1. Texture

As with CT and mammography there is an increasing demand for phantoms which provide a benchmark for quantification of tumour characteristics determined from nuclear medicine imaging, specifically texture and heterogeneity. For nuclear medicine the focus has primarily been on producing phantoms with heterogeneous radionuclide activity distributions. Although a range of approaches have been used, water-filled phantoms with solid inserts to provide a heterogeneous activity distribution most commonly used for PET imaging (Valladares *et al* 2020).

2.4.3.2. Positron range

Positron range is generally a minor concern in ^{18}F imaging with whole-body PET systems but for isotopes with higher positron energies, the influence of positron range can result in spatially-variant, absorber material dependent, resolution degradation. The majority of work studying this effect has focused on Monte Carlo simulation studies to determine the positron range effects of different radionuclides in water and other biological materials. These simulations, and subsequent phantom measurements, confirmed that positron range depends on both electron and physical density of the surrounding material. There is a scarcity of publications that have experimentally measured positron range in lung-equivalent materials for different radionuclides. Kemerink *et al* 2011 investigated the effect of positron range on spatial resolution and activity quantification of ^{18}F, ^{68}Ga and ^{124}I in lung-like tissues. Measurements were performed in water, air and in cellular polyethylene (PE foam) with densities between 0.037 g cm^{-3} and 0.164 g cm^{-3}, to simulate various lung pathologies. Alva-Sánchez *et al* 2016 investigated spatial resolution degradation due to the positron range of ^{18}F, ^{13}N and ^{68}Ga in commercially available tissue-equivalent materials ranging in physical density from 0.20 g cm^{-3}, to simulate lung tissue at full inspiration, to 1.93 g cm^{-3}, cortical bone equivalent. With the emergence of high-energy positron emitting radionuclides in PET imaging, the importance of characterising the degradation in spatial resolution and activity quantification due to positron range becomes paramount. Without this, PET images, traditionally considered to reflect activity concentration in the body, may only depict positron annihilation in the different tissues (Alva-Sánchez *et al* 2016)

3. MRI

3.1. Specification of material

This section will focus on proton MRI, for which the predominant source of signal in human tissue is from water and fat. MRI signal and contrast is determined by the magnetisation properties of longitudinal relaxation time (T_1), transverse relaxation time (T_2) and spin density from these two components. For *in vivo* tissue, T_1 is always greater than T_2 and this requires careful consideration of the choice of materials used in tissue mimicking phantoms.

Tissues being replicated are: free water at body temperature (e.g. cerebrospinal fluid (CSF), urine) with long relaxation times, where $T_1 > 4$ s and $T_2 > 2$ s, and high (effectively 100%) proton density; bound water in soft tissue with much shorter relaxation times (e.g. $T_1 = 1100/560$ ms and $T_2 = 92/82$ ms grey/white matter) (Mcrobbie *et al* 2006) and proton densities between 70%–80%; hard tissue (almost exclusively bone)

Table 3. MRI relaxation properties (arranged in approximate order of tissue T1 from highest to lowest). Data taken from (a) Yamashiro *et al* (2019), (b) Niebuhr *et al* (2016), (c) Yuan *et al* (2012), (d) Surry *et al* (2004), (e) Macq *et al* (2017), (f) In *et al* (2017), (g) Liney *et al* (1999), (h) Menikou *et al* (2015), (j) Hellerbach *et al* (2013), (k) Singhrao *et al* (2020a), (l) Mitsouras *et al* (2016), (m) Rai *et al* (2018). For reference material: (i) Rooney *et al* (2007), (ii) De Bazelaire *et al* (2004), (iii) Bottomley *et al* (1984), (iv) Price *et al* (2008), (v) Rakow-Penner *et al* (2006) (vi) Gold *et al* (2004)(vii) Reichert *et al* (2005). N/S—Not Stated.

Tissue	*T*1 (ms)	*T*2 (ms)	Principle materials	*T*1 (ms)	*T*2 (ms)	Field strength
CSF	4070[(i)]		Water + acetone[(a)]	4350	—	1.5
Prostate	1317[(ii)]	88[(ii)]	Agarose 1% + 0.01% Gd [(b)]	1338	82	1.5
Muscle	1206–797	31–47	Gelatine + 10% oil[(c)]	1084.9	64.9	1.5
Various			10% PVA Cryogel[(d)]	1034–718	175–108	1.5
Muscle	856[(iii)]	27[(iii)]	Agarose 3% + 0.02% Gd[(b)]	960	23	1.5
Liver	812[(iv)]	42[(iv)]	Carrageenan + agarose + Gd[(e)]	1252	67	N/S
Liver	812[(iv)]	42[(iv)]	UV-cured silicon[(f)]	620–306	110–54	3.0
Breast	794	—	Gelatine (50%)[(g)]	862	—	1.5
Brain			Agar[(h)]	852	66	1.5
Various			Carbomer-980 + Mn[(j)]	729.9	89.6	3.0
Pelvic bone	586[(ii)]	49[(ii)]	Carrageenan, CaC03 + Gd[(k)]	597	50	3.0
Pelvic bone	549[(ii)]	47[(ii)]	Carrageenan, CaC03 + Gd[(k)]	547	49	1.5
Bone Marrow	549[(ii)]	47[(ii)]	Vaseline + K2HPO4[(b)]	119	48	1.5
Adipose	367[(v)]	68[(ii)]	Carrageenan, glass microspheres[(k)]	353	71.0	3.0
Adipose	310	47	gelatine + 85% oil[(c)]	198	37.3	1.5
Adipose	296[(v)]	151[(vi)]	Carrageenan, glass microspheres[(k)]	285	165	1.5
Adipose	260[(iii)]	84[(iii)]	Olive oil[(b)]	214	122	1.5
Adipose	223	—	Lard[(g)]	205	—	1.5
Vertebral body			High temperature resin[(l)]	193	32	3.0
Cortical bone	140–260[(vii)]	0.4–0.5[(vii)]	Photopolymer resin[(m)]	74	0.4	3.0

with ultrashort relaxation times (<0.1 ms) and lowest proton density of between 10%–40% (Rai *et al* 2018). In the case of cortical bone the signal decay is too fast to capture, rendering this tissue hypointense on most routine images. However, ultrashort echo time (UTE) sequences do produce signal in bone further complicating the requirements of phantoms mimicking this behaviour.

The second principle signal component is fat with relaxation times for T_1 of around 200 ms and $T_2 < 100$ ms, and is found throughout the body as adipose tissue and in various fractions with water in bone marrow. Depending on the imaging parameters used, the contrast between fat and water varies greatly. As well as relaxation time differences there is a difference in resonant frequency of 3.5 ppm (or 148 Hz/Tesla) between water and fat. Some sequences separate or remove water and fat signal so that any phantom replicating this behaviour needs to contain chemically distinct materials.

3.2. Review of materials

The most basic quality assurance phantoms have utilized doped water. These tend to be for uniformity testing and have only a gross approximation of anatomy size and shape. Sometimes they will incorporate additional image quality features, e.g. breast QA phantom with two cavities in each breast well filled with saline and mineral oil with spatial resolution plate (Tuong and Gardiner 2013). For the next level of sophistication, hydrogels, i.e. water plus hydrophilic gelling agents (commonly gelatine, agar/agarose, carrageenan, and synthetic polymers) are used to more closely mimic soft tissue composition and structure.

A systematic review was conducted in PubMed and Scopus of articles relating to MRI published after 2015 on anthropomorphic phantoms relating to MRI. The keywords: 'Phantom', 'Anthropomorphic', 'MRI', 'Magnetic resonance imaging', '3D printing', 'Three-dimensional printing', 'MR guided radiotherapy', 'diffusion weighted imaging', 'MR Linac', 'radiomics phantom' and 'radiotherapy' were used in the search fields of those databases.

Table 3 shows examples of the range of materials that have been investigated together with their measured relaxation times. It is important to remember that T_1 increases with field strength while T_2 remains roughly constant. Gels on their own have similar T_2 values to *in vivo* soft tissue but often quite different T_1 values. Their relaxation properties are further modified by making changes in concentration or doping with a paramagnetic agent or both. To simulate fat, various mineral and vegetable oils or even solid animal fat have been used where the relaxation time and also the chemical shift is important to consider. There has also been use of soya oil and carrageenan emulsions (Bernard *et al* 2008) in an attempt to reproduce intravoxel signal contributions of fat-water, typically found in bone marrow. Another consideration in phantom construction is magnetic susceptibility (Wapler *et al* 2014) of both the material

and its container. Water and perspex are very similar (<0.004 ppm) but larger differences of 1.33 ppm exist between water and air so this needs consideration in terms of composition and manufacture of materials.

3D printing is increasingly used (Filippou and Tsoumpas 2018) to produce complicated anthropomorphic shapes, although this usually still requires the objects to be filled with signal positive materials. Niebuhr *et al* (2016) designed a pelvic phantom with a 3D printed hollow skeleton filled with dipotassium hydrogen phosphate and Vaseline for bone marrow, wrapped with gypsum bandages for harder exterior bone. Soft tissue was agarose doped with gadolinium and vegetable oil for fat. Singhrao *et al* (2020a) used much more simplified ingredients involving carrageenan with $CaCO_3$ and glass microspheres to modify the electron density for CT in a pelvic phantom.

There is an increasing demand for phantoms that simulate physiological motion due to advances such as 4D MRI and MR-guided radiotherapy. In the aforementioned pelvic phantom silicon spheres filled with air and water represented rectum and bladder respectively and these could be filled from an external syringe. de Merxem *et al* 2017 used carrageenan based organ shapes in a container attached to a membrane that was driven pneumatically. Organs included liver, stomach, pancreas and liver tumour with Gadolinium used to modify T_1 and agarose to modify T_2. Other ingredients include NaCl and sodium azide for conductivity and preservation respectively.

3.3. Limitations

One challenge with using water in realistic phantoms is that the $T1/T2$ ratio is unity even if doped with paramagnetic agents. Most paramagnetic solutions exhibit changes with temperature (other than nickel) and for temperatures significantly different to room temperature this needs to be considered. Interestingly, Yamashiro *et al* (2019) used acetone diluted with water at room temperature to increase T_1 to match CSF that would otherwise be lower with pure water at room temperature. Long settling times and intrascan vibrational issues are also another limitation when fluids are used.

Dielectric effects at higher fields (3 T and above), where the shorter wavelength leads to non-uniformities in water and hydrogels, necessitate the use of oil filled phantoms or adjustment of conductivity. In one study (Niebuhr *et al* 2016) the increased salt used in the gelatine, to more accurately match electron densities, created problematic dielectric artefacts. Conversely (Wood *et al* 2017) used a 3D printed head and neck phantom with various compartments filled with different solutions of NaCl (to change conductivity) and ethanol (to change permittivity) to examine the electromagnetic properties at 7 T.

Limitations with gels are often associated with complicated manufacturing e.g. using high temperatures or degassing required to prevent air bubbles. Shelf life is compromized without the use of toxic preservatives. Furthermore, as these are in the main natural products these will be difficult to standardize. Synthetic polymer gels based on polyacrylic acid (Hellerbach *et al* 2013) provide the advantage over more routinely used agar and gelatine materials of significantly improved longevity without the need for toxic preservatives. The gels can be left undoped ($T_1 = 4$ s, $T_2 = 2$ s) or doped with manganese nitrate (e.g. 1000 ms $< T_1 <$ 1800 ms & $T_2 \approx 100$ ms). The pH was modified to change viscosity as required for more complicated uses. In *et al* (2017) further showed the potential use of samples of UV-cured hydrophilic silicone gels which would reduce the high water content present with hydrogels and potentially improve shrinkage and long term stability.

Although trabecular bone can be simulated very effectively, cortical bone is more challenging (Singhrao *et al* 2020a). Increasingly multi-modality phantoms, particularly MR-CT and MR-PET as discussed in section 5, are trying to combine electron dense materials that also have the required MRI signal properties.

3.4. Latest developments

The latest developments in MRI centre around pursuing new materials and/or more complicated phantoms to simulate physiological behaviour in addition to anatomy. An example of this is Mikayama *et al* (2020) who developed a novel diffusion weighted imaging (DWI) phantom using acrylic fine particles suspended in detergents. The study found that the apparent diffusion coefficient, a measure of the magnitude of diffusion (of water molecules) within tissue, decreases with an increase in particle volume ratio, thereby effectively simulating the tumour extracellular space.

Demand for more complicated motion behaviour motivates the use of deformable materials. Tavakoli *et al* (2012) exploited earlier work by using PVA solution in moulds with successive freeze-thaw (FT) cycles to produce a so-called cryogel (PVA-C). This was used to create a two chamber cardiac phantom model that could be dynamically operated by pressure driven balloons inside these chambers. Simutec (Ontario, Canada) has developed motorized heart phantoms that are both CT and MRI compatible (Model:DHP-MRI, Simutec 2018). The phantom features pneumatic control, a tissue equivalent heart and an acrylic tank that can be filled with any liquid.

Chakouch *et al* (2015) developed a phantom that mimics both the functional and structural properties of the thigh muscle for assessment under magnetic resonance elastography (MRE) using a mixture of a softener and a plastisol, which is a suspension of PVC. The phantom included two components with each side having concentrations of plastisol ranging from 50% and 70% to mimic the relaxed and contracted thigh muscle respectively. These two components were separated with a plastic sheet to mimic the aponeurosis membrane separating the two parts of the muscle. The muscle fibres of the thigh was also subtly simulated by using a Teflon pipe that was threaded through the plastisol suspensions creating a signal void within the muscle tissue. Two pneumatic drivers were used to generate waves within each muscle component in the phantom and successfully mimic the functional properties of the thigh muscle

In the last few years solid resins have been demonstrated that enable the direct 3D printing of objects with MRI-visible signal. Mitsouras *et al* (2016) used these resins for surgical vertebral implant testing/training. This material was further explored as the basis for a range of structured test objects and anthropomorphic phantoms (Rai *et al* 2019). Rai *et al* (2018) used a photopolymer resin that mimics the MRI relaxation properties of cortical bone although this material had a significantly lower electron density making it unsuitable for CT. A novel phantom for radiomics in a multicentre setting has also been developed through 3D printing techniques (Rai *et al* 2020). The phantom was constructed from a solid resin that successfully mimicked various shapes and textures required for radiomics analysis. Two sets of the phantom were 3D printed for the study in two countries, and were used for stability measurements across various MRI systems. The advantage of this method of phantom production is that it will allow for better standardization and quality control of MRI acquisition protocols in radiomics studies across multiple institutions. The Filippou and Tsoumpas (2018) review previously discussed, concluded that as yet only a small number of materials have been examined and this currently restricts these to single modality use. In *et al* (2017) proposed the use of digital light processing (DLP) 3D printing as an alternative to more expensive photo polymerized resins although curing time may set the limit to achievable relaxation times.

4. Ultrasound

4.1. Specification of material

4.1.1. General specifications

Due to the diverse applications of diagnostic ultrasound including, B-mode imaging, elastography, Doppler imaging, contrast enhanced ultrasound (CEUS) and more recently photoacoustic imaging (PAI), many candidate TMM materials are available to mimic relevant properties of biological tissue. The important acoustic and mechanical characteristics of a number of different tissue types are summarized in table 4. It is important to note that the tabulated ex-vivo properties should be regarded as typical values as they can depend on several biological factors, including age, disease state and ethnicity, as well as the employed measurement techniques.

Developing TMMs to specified approximately tissue-like values assists in system calibration and performance management, clinician training and the development of robust techniques. Whilst the most appropriate properties of tissue depend on the particular clinical application of ultrasound, the most frequently reported parameters for tissues and TMMs include the speed of sound, attenuation coefficient, acoustic impedance, density and Young's modulus (where the TMM is to be used for elasticity imaging). Other properties that are important for the TMM to truly represent biological tissue properties are backscatter coefficient (BSC) and nonlinearity. However, the challenge in measuring these quantities accurately means that they are less frequently reported in the literature (Culjat *et al* 2010), perhaps due to the fact that BSC methods have increased variability, can require adjustments of characterisation set-up and involve a higher level of computational complexity (Wear *et al* 2005).The use of BSC measurements has gained increased attention in quantitative ultrasound (QUS), however further research into factors affecting the variability of such measurements is still required (Han *et al* 2018). A number of interlaboratory comparisons of BSC measurements have been carried out with varying degrees of success (Madsen *et al* 1999, Wear *et al* 2005, Anderson *et al* 2010). BSC measurement methods can be dependent on a number of factors including, speed of sound and attenuation of the material, acoustic intensity at the point of interest (Zeqiri *et al* 2010) and radius of curvature of the transducer (meaning often they are dependent on manufacturer supplied details) (Wear *et al* 2005). Additionally a number of methods have been proposed, which can affect the magnitude and frequency dependence of the estimated BSC, thus introducing significant variability in QUS (Lavarello *et al* 2011). Further standardisation of BSC measurement methods is needed to achieve the required up-take of such measurements in TMM characterisation. Materials added to TMMs to produce backscatter include, SiC, Al_2O_3, powdered graphite and glass beads (King *et al* 2011, Cannon *et al* 2011). A review of measurement methods for the acoustic properties of tissue-like materials may be found in Zeqiri *et al* (2010). Thermal properties are also important for some applications including specific heat

Table 4. Acoustic and mechanical characteristics of tissues adapted from IEC 60 601-2-37 (IEC 2007), Culjat *et al* (2010) and Mast (2000) and supplemented with ICRU Report 61 (1998). (a) IEC (2007), (b) ICRU Report 61 (1998), (c) Mast (2000), (d) Li *et al* (2016), (e) Cao *et al* (2017) (f) Culjat *et al* (2010), (g) Cournane *et al* (2011), (h) Doyle *et al* (2017), (i) Taylor and Miller (2004), (j) Budday *et al* (2017), (k) Yeh *et al* (2002), (l) Umale *et al* (2013), (m) Thomas *et al* (1998), (n) Parker *et al* (1993), (o) Kot *et al* (2012). * frequency dependence $f^{1.2}$ ** wide uncertainty has been reported for bone properties *** frequency dependence f.

Tissue type	Speed of sound (ms^{-1})	Attenuation coefficient (dB $cm^{-1}MHz^{-1}$)	Nonlinearity parameter (B/A)	Acoustic impedance (10^6 kgm^{-2} s^{-1})	Elastic modulus (kPa)	Density ($kg\ m^{-3}$)	Backscatter coeffieient 10^{-3} m^{-1} sr^{-1}
Soft tissue[(a),(b)]	1575	0.6–2.24*	7.0	1.66	—	1055	—
Soft tissue Fatty[(a),(b)]	1465	0.4	8.5	1.44	—	985	—
Cortical bone**	3635	14–22	—	6.98	—	1920	—
Muscle[(b), (c),(d),(e)]	1547	1.09	—	1.62	13–32	1050	316 @ 2–10 MHz cardiac, 920 @ 4 MHz skeletal;
Brain[(c),(f), (i),(j)]	1560	0.6	7.1	1.62	0.58,0.33–1.6	1040	—
Breast[(c),(f),(g)]	1510	0.75	—	1.54	25 (healthy) 30–200 (malignant)	1020	—
Liver[(b), (c),(f),(g),(k)]	1595	0.5	6.6	1.69	0.64–1.7	1060	10_- 150 @ 4 MHz
Kidney[(c),(e),(l)]	1560	1.0	7.4	1.64	15 (kidney cortex)	1050	—
Prostate[(f),(h)]	1614	1.86	—	—	38–96, 14–40	—	—
Blood[(b),(c),(f)]	1570	0.1***	6.1	1.68	—	1050	3.4 @ 4 MHz

capacity and thermal conductivity; however, they are not discussed here but rather in section 8, Thermal therapies.

4.1.2. Standardization of TMMs for ultrasound applications

Through International Electrotechnical Commission (IEC) Technical Committee 87: Ultrasonics, various specification standards have been published which refer to TMMs. One of these recommends that TMMs for conventional B-mode imaging should mimic soft tissues and possess a speed of sound of 1540 ms^{-1} and an attenuation coefficient of 0.5–0.7 dB cm^{-1} MHz^{-1} over the frequency range of 2–15 MHz (IEC 2007). Doppler string and band test objects are recommended with an attenuation coefficient in the range 0.5–1 dB cm^{-1} MHz^{-1} in the technical standard for continuous wave Doppler systems (Technical Committee EPL/87 Ultrasonics 1995) and flow phantoms involving blood or blood mimicking fluids (BMFs) are recommended to require a reflected signal level equal to that produced by a blood-vessel wall. IEC 61685:2001 is applicable to continuous wave, pulsed and colour flow doppler systems and requires BMF properties to be similar to those *in vivo*, with a speed of sound of 1570 ± 30 ms^{-1} (Technical Committee EPL/87 Ultrasonics 2001). As yet there are no equivalent standards published for Elastography, CEUS or PAI. In a review of elastography phantoms, values for the mechanical properties for TMMs for background and diseased tissue have been proposed (Cournane *et al* 2011). The IEC have also published a technical standard detailing guidance on methods for characterisation of ultrasound materials (Technical Committee EPL/87 Ultrasonics 2019).

4.2. Review of materials

Commonly used commercial phantoms (manufactured for quality assurance testing and user training by e.g. Gammex RMI Ltd—condensed milk based TMM, ATS Labs Inc—urethane rubber based TMM and CIRS Inc- Zerdine™ TMM (Browne *et al* 2003), Blue phantoms—CAE healthcare, Kyoto Kagaku phantoms) provide good test beds for quality assurance and performance testing, however the ability to tune acoustic properties to mimic various tissue types and to build anthropomorphic phantom test devices is undergoing continuous development in the research community. Additionally, due to the proprietary nature of these commercial phantoms, a full database of constituent materials and their properties is not available. This review generally addresses soft TMMs and focusses primarily on those developed for ultrasound techniques already widely practiced in the clinic; traditional B-mode ultrasound, Doppler ultrasound (BMFs) and Elastography, with some of the materials being applicable for other techniques. Search terms for this review included: 'Ultrasound phantom', 'Ultrasound TMM', 'Ultrasound TMM', 'Acoustic Characterisation of

Table 5. Acoustic and mechanical properties of commonly used TMMs for various ultrasound applications where (a) Rajagopal *et al* (2015), (b) IEC (2007), (c) Cannon *et al* (2011), (d) Browne *et al* (2003), (e) Oudry *et al* (2009), (f) Cabrelli *et al* (2017b), (g) Grillo *et al* (2017), (h) Vieira *et al* (2013), (i) Maneas *et al* (2018a), (j) Cournane *et al* (2010), (k) Fromageau *et al* (2003), (l) Malone *et al* (2020), (m) Vogt *et al* (2017), (n) Fonseca *et al* (2016), (o) Hungr *et al* (2012), (p) Bakaric *et al* (2020), (q) Cournane *et al* (2011) (r) Kagaku Kyoto., (s) Madsen *et al* (2003), (t) Madsen *et al* (2006), (u) Culjat *et al* (2010).

TMM	Speed of sound (ms^{-1})	Acoustic attenuation coefficient ($dB\ cm^{-1}\ MHz^{-1}$)	Acoustic impedance ($10^6\ kg\ m^{-2}\ s^{-1}$)	Density ($kg\ m^{-3}$)	Young's Modulus (kPa)
Agar based [(a),(b) (c)]	1544 ± 3.1 (1–60 MHz),1490–1570	0.5 @ 3 MHz, 0.93 @ 60 MHz,0.1–0.9 @7.5 MHZ	1.6	1050	—
Agar & Gelatine[(q)]	1492–1575	0.1–0.52	—	—	0.5–4.6
Gelatine[(u)]	1520–1650	0.12–1.5	1.6–1.73	1050	—
Oil in Gelatine[(s),(t)]	1496–1538	0.1–0.89 $dBcm^{-1}MHz^{-1}$ @ 2.25 MHz		950–1010	20–70
Condensed Milk based Gammex RMI[(d)]	1540	0.5	—	—	—
Copolymer in oil based[(e),(f),(g)]	1420–1502	0.1–1.2 @ 3.5 MHz	—	760–930	2.2–150
Gel wax based [(h),(i)]	1425–1480	0.04–0.3 @7.5 MHz, 0.2–1 @ 3 MHz, 0.7–2.7 @ 10 MHz	—	—	14.7–34.9
PVAc based (5–20%) [(j),(k),(l)]	1540–1570	0.13–0.67 @7.5 MHz	—	—	1.6–320
PVC based [(m)(n)(o)(p)]	1435–1520, 1360–1400	0.7–2.1 @ 7 MHz	—	1008	3–200
Silicone[(b)]	1201	1.8 @ 3 MHz	1.3	1243	
Urethane Rubber ATS Labs[(d)]	1460	0.5–0.7	—	1310	—
Zerdine™ CIRS Inc[(d)]	1540	0.5–0.7	—	—	—
Kyoto Kagaku QA phantom material[(r)]	1432	0.59	1.38	—	—

'TMM material", 'Commercial Ultrasound phantom', 'Ultrasound BMF', '3D printed Ultrasound phantom'. The soft tissue materials reviewed in greater detail are limited to those that have been developed and commonly used since 2015 along with the current standard material recommended by the International Electrochemical Committee. The reader is directed to (Culjat *et al* 2010, Cournane *et al* 2011) for more deatailed information about other possible materials, such as gelatin and agar-gelatin mixes.

The acoustic properties of commonly used TMMs for these various clinical ultrasound applications are detailed in table 5 with a selection of these being subsequently discussed in greater detail. It should be noted that the properties of attenuation coefficient and speed of sound vary with frequency and temperature. Properties are often reported at room or ambient temperature, and this can vary, particularly when the materials are used in non-temperature controlled environments, for example as would be the case during routine equipment QA in a clinic. In a study of the influence of temperature on TMMs, Browne *et al* (Browne *et al* 2003) noted that if the temperature of the commercial test objects varied between 15 °C and 25 °C the change in speed of sound would result in changes in lateral resolution and slice thickness results in QC and performance tests, especially for phantoms which use distance corrected object placement to compensate for acoustic speed of sound differences (Browne *et al* 2003).

4.2.1. Agar

Agar based TMMs are commonly used. An agar material developed through a European Commission funded collaborative project combines agar with water, glycerol, benzalkonium chloride, SiC and Al2O3 to produce a material with attenuation coefficient 0.5 $dB\ cm^{-1}\ MHz^{-1}$, speed of sound of 1541 ms^{-1} and density of 1054 kgm^{-3} (Teirlinck *et al* 1998, Ramnarine *et al* 2001). The recipe specified in Annex DD IEC 60601-2-37 (IEC 2007) has been reproduced in many studies and extensively characterized (Browne *et al* 2003, Inglis *et al* 2006, Brewin *et al* 2008, Sun *et al* 2012, Rajagopal *et al* 2015). The attenuation coefficient of the material has

a non-linear frequency dependence particularly prevalent above 20 MHz. The speed of sound estimated with an uncertainty of ± 3.1 ms^{-1} was found to vary from 1541 m^{-1} to 1547 m^{-1} in the range of 1–60 MHz (Rajagopal *et al* 2015).The acoustic nonlinearity of IEC agar has been derived (Zeqiri *et al* 2015) using a finite amplitude insertion technique to be 4.5 ± 0.5, which is significantly lower than that reported for soft tissues.

4.2.2. PVAc

Polyvinyl alcohol cryogels (PVAc) have been suggested as potential elastography TMMs (Fromageau *et al* 2003, Cournane *et al* 2010). Through altering concentrations of PVA and varying the number of FT cycles it is possible to achieve different acoustic and mechanical properties. This material has been used for vessel mimicking materials (Malone *et al* 2020). Mix *et al* developed abdominal aorta phantoms using various combinations of different percentage PVAc with calcium carbide for ultrasound elastography (Mix *et al* 2018). Weir *et al* added aluminium oxide to a 10% PVAc to achieve a speed of sound of 1524 ms^{-1} for a transcranial Doppler phantom (Weir *et al* 2015). Additionally, this TMM has been applied to photoacoustic phantoms (Arabul *et al* 2015), through optimizing FT cycles to increase turbidity and adding optical scatterers to tune optical properties.

4.2.3. Gel wax

Gel wax has been used as a TMM with 3D printed moulds for anatomical phantoms for B-mode imaging (Maneas *et al* 2018a) and for multispectral PAI (Maneas *et al* 2018b). Such materials have good longevity as no dehydration occurs. They have been used to prepare a TMM for nerve and vessel phantoms, a heart atrium phantom and a placenta phantom (Maneas *et al* 2018a). Using various concentrations of paraffin wax and glass microspheres as additives to gel wax, attenuation coefficient values of 0.7–2.9 dB cm^{-1} at 3 MHz and speeds of sound 1443–1449 ms^{-1} were achieved (Maneas *et al* 2018a). Gel wax was found to have a Young's modulus of 17.4 ± 1.4 kPa (Maneas *et al* 2018a). The authors suggest that gel wax might be 3D printed for ultrasound phantoms using a similar technique to Dong et al's optical phantom study (Dong *et al* 2015).

4.2.4. Copolymer in oil

The exact compositions of the commercial 'Gel Wax' materials described above is proprietary information (Maneas *et al* 2018b) and batch-to-batch variation is unknown. Similar phantoms have been made using the co-polymer in oil process for both ultrasound (Cabrelli *et al* 2017a) and Photoacoustic applications (Cabrelli *et al* 2015, 2017b, Grillo *et al* 2017). The advantage of such phantoms lies in the ability to develop a standardized recipe due to the non-proprietary nature of the components as well as the potential for better control of the various acoustic parameters using standardized controlled components. Cabrelli *et al* (2017b) have described various studies of co-polymer in oil phantoms using a styrene-ethylene/butylene-styrene and low-density polyethylene in mineral oil combination, reporting control of attenuation coefficient values (0.5–25 dB cm^{-1}) through altering component ratios. Little variation in the speed of sound was noted ($\sim$ 1450–1480 ms^{-1}) (Cabrelli *et al* 2017b). Through the addition of glycerol to the manufacturing process it was possible to alter the speed of sound also, achieving a range of 1423–1502 ms^{-1} (Cabrelli *et al* 2017a). However, such materials have also been noted to have a strong temperature dependence in acoustic speed of sound (Ivory *et al* 2019).

4.2.5. PVCP

Polyvinyl chloride plastisol (PVCP) TMM has been used in ultrasound applications, for breast phantoms (De Carvalho *et al* 2016, De Matheo *et al* 2018) and to mimic needle resistance (Pepley *et al* 2018), as well as in photoacoustics (Fonseca *et al* 2015, Vogt *et al* 2016, Bakaric *et al* 2020). PVCP TMM, commonly referred to in ultrasound and photoacoustics, has also been referred to as PVC TMM in some fields for example in surgical phantoms for needle insertion training (Li *et al* 2015b). Using different quantities of softener, the speed of sound and attenuation coefficient can be altered (Fonseca *et al* 2015) and using various combinations of PVC and binary plasticizer comprising benzyl butyl phthalate and di(2-ethylhexyl) adipate, TMMs mimicking fatty, background, parenchyma/dense breast tissue have been proposed along with other tissues (Vogt *et al* 2017). By adding graphite powder De Carvalho *et al* (2016) mimicked glandular tissue and various lesions, altering the attenuation coefficient (0.29–0.94 dB cm^{-1} MHz^{-1}) and introducing a speckle pattern in the images. The achieved speeds of sound were low (1379.3–1397.9 ms^{-1}) (De Carvalho *et al* 2016). The same group used a dioctyl phthalate plasticizer, graphite and aluminium oxide to produce breast TMMs for lactiferous duct, fat and glandular tissue, the material had a stable speed of sound over 1 year but variations in attenuation coefficient were noted over this time period (De Matheo *et al* 2018). Pepley *et al* (2018) found that PVC, diethyl hexyl adipate plasticizer softener, mineral oil, and chalk powder could be used to provide needle resistance closely resembling cadaveric tissue at 16 mm depth, measuring the axial needle insertion force to support training in ultrasound visualisation procedures (Pepley *et al* 2018).

4.2.6. Blood mimicking fluids

BMFs have been primarily developed for Doppler ultrasound. Like other TMMs, BMFs need to possess acoustic speed of sound, attenuation coefficient and BSC approximating blood, however density, viscosity and particle size are also important factors (Samavat and Evans 2006). The target properties defined by the IEC are viscosity 4.0 ± 0.4 Pa s, speed of sound 1570 ± 30 m s^{-1}, attenuation < 0.1 × 10^{-4} × f dB cm^{-1} MHz^{-1} and density 1050 ± 40 kg m^{-3} (Technical Committee EPL/87 Ultrasonics 2001). Many BMFs are produced in a method similar to that reported by Ramnarine *et al* (1998) and are based on mixtures of Orgasol® (Nylon) particles, water, glycerol, Dextran and Synperonic® N detergent surfactant. This type of BMF is recommended by the IEC technical standards for flow Doppler test objects (Technical Committee EPL/87 Ultrasonics 2001). However, such materials have been noted to aggregate in suspension with scatterers settling out when not in use (Kenwright *et al* 2015). Studies have suggested the use of materials based on combinations of water-soluble silicone oil and glycerine aqueous solution with polystyrene particles as an alternative that avoids such settling (Tanaka *et al* 2012). Poly(4 methylstyrene) particles have also been indicated as suitable scatterers combining distilled water, propylene glycol, and polyethylene glycol in an easy to prepare and low-cost BMF (Oglat *et al* 2018).

4.2.7. 3D printed materials

3D-printing in the manufacture of ultrasound phantoms is predominately used either for printing anthropomorphic casts from clinical datasets or to mimic bone. Maneas *et al* 3D printed moulds for anatomically realistic phantoms, a heart atrium phantom developed from an MRI dataset and a placental phantom was developed from a clinical sample with large vessels digitally traced in two dimensions from a photograph using vector graphics software. This was extended to a 3D model using 3D drawing software and then printed in two parts to prepare a gel-wax phantom (Maneas *et al* 2018a). The same department also produced a 3D printed lung, liver and ribcage phantoms, adding chicken breast and mineral-oil based wax, the ribcage phantom successfully demonstrated shadowing effects in a clinical training tool for ultrasound guided kidney biopsy. Cloonan *et al*, however, 3D printed aortic models from flexible photopolymerizable polymer materials producing phantoms of complex geometry and tortuosity to assess feasibility of 3D printed flow phantoms. The 3D printed models were embedded in 6% gelatin and imaged using pulsed wave imaging (Cloonan *et al* 2014). Vessel mimicking phantoms have also been constructed by 3D printing water-soluble PVA filament vessel cores which were coated in paraffin wax before being encased in PVAc (Dong *et al* 2020). The vessel core was then be dissolved after the PVAc had undergone the appropriate FT cycles to create a walled vessel-mimicking phantom. B-mode and power Doppler imaging were used to confirm the vessel core dissolution, while ultrafast Doppler imaging and shear wave imaging results were verified with fluid-structure interaction simulation results to confirm the phantoms suitability for assessment of blood vessel imaging techniques. Gatto *et al* developed a neonatal skull phantom and embedded fine-wire thermocouples in the phantom to assess thermal rise in tissues during trans-cranial ultrasonic scanning of pre-term neonates (Gatto *et al* 2012). They achieved acoustic properties mimicking neonatal skull by manufacturing a ceramic infiltrated with epoxy resin (6.85 ± 0.7 dB cm^{-1}). With increased use of 3D-printing techniques there is a growing need for acoustic characterisation of materials used. For a further review of 3D printing phantoms for medical imaging the reader is directed to Filippou and Tsoumpas (2018).

4.3. Limitations

The ideal ultrasound TMM should have: independently tuneable acoustic properties, tuneable mechanical properties, good longevity and structural integrity, the ability to hold inclusions/lesions, well characterized temperature and frequency dependence and the ability to mimic different anthropometric structures. The recipe for IEC agar (IEC 2007) is easy to fabricate, used extensively, well characterized in the literature and is stable in terms of acoustic properties and mechanical stability over long time periods when stored correctly. Additionally, the formulation may be tailored to produce various acoustic properties to mimic specific tissue types. However, the longevity, in addition to potential dehydration and microbial invasion if not stored in the correct preserving fluid, a water/glycerol mixture (IEC 2007), is dependent on handling and usage due to the fragility of the TMM. PVAc materials involve a complex and lengthy fabrication process but the tunability of the acoustic and mechanical properties, structural rigidity and longevity are extremely beneficial. Commercial PVCP and Gel Wax formulations are proprietary information and the batch-to-batch variation is unknown, which may result in variations of acoustic properties (Vogt *et al* 2016, Ivory *et al* 2019). In general, the manufacture of PVCP is challenging as it requires high temperatures and the high attenuation coefficient may limit use to lower frequencies. Speed of sound of Copolymer in oil, Gel Wax and many PVCP formulations is low and may restrict their use to specific ultrasound applications for fatty tissue such as breast. Further characterisation of many of the cited materials is necessary in order to derive the variation of the key acoustic and mechanical properties with temperature.

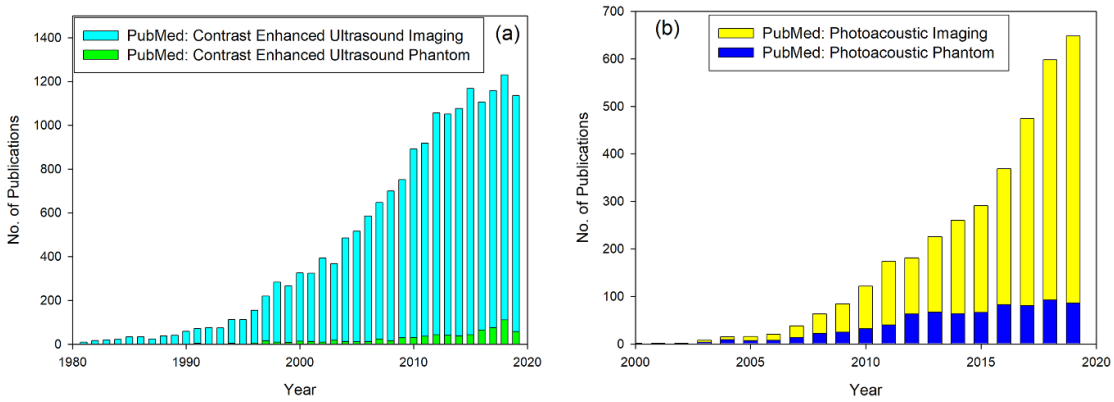

Figure 6. (a) The number of returned articles with search phrase 'contrast enhanced ultrasound phantom' on Pubmed by year, (b) the number of returned articles with search phrase 'Photoacoustic imaging' and 'photoacoustic phantom' on Pubmed by year.

4.4. Latest developments

CEUS phantoms are primarily focused on flow and do not necessarily need to mimic the same acoustic properties as other ultrasound phantoms. For example, phantoms for testing imaging techniques quantifying blood perfusion must have a complex flow and perfusion system and should simulate spatially distributed small vessels with various different flow directions (Eriksson *et al* 1995). Literature cited phantoms include those using several tubes knotted together in a cluster (Eriksson *et al* 1995), dialysis cartridges (Veltmann *et al* 2002) and reticulated foam phantoms (Ivory 2018). As the primary tissue mimicking characteristic of such phantoms (i.e. perfusion) differs significantly from other ultrasound techniques, further discussion is not included in this review, however as is apparent from the low count of papers when searching for CEUS phantom (figure 6(a)), which shows an approximately exponential increase over time, there is certainly room for growth in this area. An overview of perfusion phantoms including US, MRI, CT and PET applications has recently been published (Kamphuis *et al* 2020). Due to the nature of the main targeted tissue mimicking property, perfusion, in this case often different approaches are suitable for more than one imaging technique.

PAI, which combines optical contrast with the good penetration depth of ultrasound by detecting ultrasound signals generated in tissue illuminated by a short laser pulse, is a relatively new technique and, as can be seen in figure 6(b), the number of citations on Pubmed for the search phrase 'Photoacoustic Imaging' has been steadily growing over the past 20 years. The number of papers found with search phrase 'Photoacoustic phantom' is comparably much lower, with only seven papers when searching 'Photoacoustic Tissue Mimicking Material'. This may be due to the challenge in developing appropriate materials because of the number of characteristics which must be considered; not only the acoustic characteristics discussed earlier but also optical characteristics such as absorption and scattering coefficients and the thermoelastic efficiency, the Grüneisen parameter. Clearly there is likely to be significant growth in this area in relation to standardization and the development of materials for use as phantoms, as evidenced by efforts to develop a standardized Photoacoustic TMM within the International Photoacoustic Standardization Consortium (Bohndiek 2019).

5. Multi-modality imaging

5.1. MR-CT

The increasing use of MRI planned radiotherapy has led to the need for MR-CT modality phantoms. Depending on their utilisation, these can range from simplistic end-to-end registration type test objects to full imaging and dosimetry use on hybrid MR-Linear accelerators. Singhrao *et al* (2020a) extended their pelvic phantom (Singhrao *et al* 2020b) with the addition of an opening for an ionisation chamber. This was used to plan and simulate an IMRT treatment with images acquired on CT, MRI and a CBCT. Previously discussed dynamic phantoms such as that by Perrin *et al* (2017) are starting to be modified to become MR visible (Colvill *et al* 2020). Others are investigating flexible 3D printed materials, ideal for these type of modifications (Neumann *et al* 2019). Pappas *et al* (2019) used a 3D printed skull that was CT equivalent and filled with a radiosensitive gel dosimeter to successfully show radiation delivery on an MRI-Linac. This will be discussed in further detail in section 6.

Figure 7 shows example images acquired for a prototype head and neck phantom that was specifically commissioned for MR-CT planned radiotherapy (PureImaging phantoms, UK). The phantom has realistic anatomical details (brain with tumour, ventricles, skull, orbits, trachea and spinal cord) and is made from

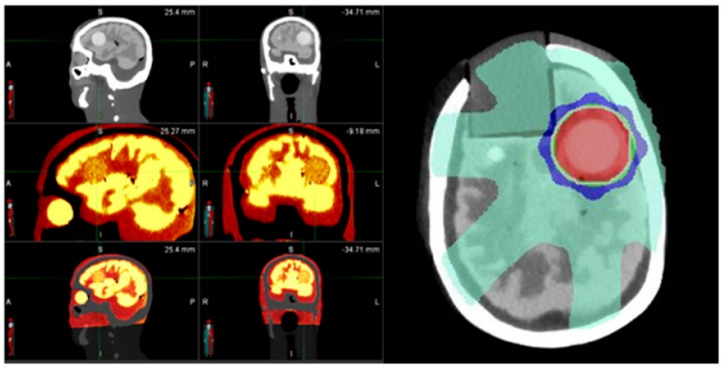

Figure 7. (top) CT and MRI (colour) overlay acquired in a prototype phantom made from solid materials. This version has several anatomical features with equivalent bone electron density and realistic T2 values in grey and white matter. (bottom) Two tumour targets were also included, the larger of which is the subject of this simulated radiotherapy plan (right).

entirely solid materials including PU resin (Yunker *et al* 2013) for soft tissues and ceramic-reinforced epoxy for bones. This achieves CT equivalence with HU equal to 1500 (cortical bone) and −25 (soft tissue). Measured T2 values of grey and white matter (80 ms and 90 ms) are also realistic although CSF was found to be too low (100 ms). Images show fusion of CT and 3.0 Tesla T2-weighted datasets and a subsequent treatment plan created for the large tumour (plan courtesy of Natalia Roberts, Ingham Institute). Interestingly, there was some signal generated on UTE sequences in the cortical bone material (not shown). This degree of realism in cortical bone is crucial for various MR-only (without CT) methods where a synthetic CT (sCT) is generated from a single MRI scan. There are various methods to generate a sCT such as atlas based electron density mapping (Dowling *et al* 2012), however this relies on image registration of the MRI to an atlas of generic anatomical contours which can have a degree of uncertainty particularly for atypical anatomy. Alternative methods utilize UTE imaging which facilitate voxel modelling (Johansson *et al* 2011) where all MRI voxel values are converted into HU. This removes the need for reliance on image registration achieving more accurate representation of the unique density values of tissue as each individual voxel is assigned a HU.

5.2. PET/MRI

As clinical PET/MRI systems become more widely available there is a need for hybrid phantoms which allow assessment of system performance across multiple sites. Recent recommendations for a minimum set of QC procedres have been developed to ensure the proper functioning of whole-body PET/MRI systems (Valladares *et al* 2019) however these generally use separate phantoms for each modality and do not consider tissue equivalence. Chandramohan *et al* (2020) report the development of bone material analogues based on a gypsum plaster cement ($CaSO_4 \cdot 2H_2O$) that can be used in construction of phantoms for simultaneous PET/MRI systems. The water used to form the plaster was doped with three materials, each targeting a separate imaging parameter; an iodinated CT contrast, Iohexol (Omnipaque, GE), used to increase attenuation; a gadolinium-based MR contrast agent, Gadodiamide (Omniscan, GE), used to shorten the MR T1 and T2* relaxation times, along with copper sulfate ($CuSO_4 \cdot nH_2O$). They report that the undoped plaster has a 511 keV attenuation coefficient (0.14 cm^{-1}) similar to cortical bone (0.10–0.15 cm^{-1}), but slightly longer $T1$ (∼500 ms) and $T2^*$ (∼1.2 ms) MR parameters compared to bone ($T1$ ∼300 ms, $T2^*$ ∼0.4 ms). Doping with the iodinated agent resulted in increased attenuation with minimal perturbation to the MR parameters, doping with a gadolinium chelate greatly reduced $T1$ and $T2^*$ while the attenuation coefficient was unchanged. Doping with copper sulfate was more selective for $T2^*$ shortening and achieved comparable $T1$ and $T2^*$ values to bone (after 1 week of drying), while the attenuation coefficient was unchanged. O'Doherty *et al* (2017) report the use of an in-house designed and built myocardial perfusion phantom with simultaneous infection of ^{18}F and gadolinium based contrast agent (GBCA) (Gadovist R, Bayer HealthCare, Germany) to reproduce ground-truth myocardial perfusion rates measured with both PET and MR imaging.

5.3. MRI-US

Due to the high content of water, hydrogels based TMMs are suitable for both MRI and ultrasound. On the other hand, for the opposite reason, 3D printed materials and plastics have been used to mimic bones in multi-modality MRI/US phantoms. The use of PVC has been suggested for multimodality phantoms, by Li *et al* (2016) where a regression model was developed to design soft PVC with targeted mechanical and

medical imaging properties through variations in the mass ratio of softener to PVC polymer solution, the mass fraction of the mineral oil and the mass fraction of glass bead additives (Li *et al* 2016). A multimodal breast phantom was also developed using PVC including various targets mimicking tumours, micocalcifications and fibrous lesions and tested with mammography, MR and US imaging techniques (He *et al* 2019a). Caldwell *et al* (2019) developed a novel prostate phantom for MRI/US fusion biopsy. Similar to Hungr *et al* (2012) (table 7) the phantom is constructed from a combination of materials including polyvinylchloride-plastisol (PVCP) for the body of the prostate and plastina non-hardening clay for the intraprostatic lesions. Non-hardening clay was favoured over the hardening type as it allows more realistic retrieval of biopsy samples. PVA based phantoms (Vidal *et al* 2019) for mimicking ovarian endometriosis and multi-purpose gelatine based phantoms (Walter *et al* 2018) have been recently suggested as a tool for image fusion and needle biopsy training.

Menikou *et al* (2015) developed a MRI compatible head phantom from a 3D print of an adult brain CT scan using agar-evaporated milk-silica gel to mimic cerebral tissue and ABS plastic to mimic the skull to assess heating effects in MRI guided FUS for treating brain cancer (Menikou *et al* 2015). (Hofstetter *et al* 2020) also developed a tissue mimicking phantom for MRI guided High-intensity focused ultrasound (HIFU) to assess temperature changes using shear-wave (SWE). SWE can be used to detect changes in the mechanical properties of tissues following HIFU sonications (see section 8). Their phantom was constructed from a mixture of 50% evaporated milk, 50% degassed deionized water, gelatin, preservatives and varying concentration of psyllium husk (0.15–4.8 g). The addition of psyllium husk was to minimise MRI susceptibility artefacts and to increase US scattering.

Finally, Eranki *et al* (2019) developed a phantom using an acrylamide-based TMM material (table 10) with added silicon dioxide and bovine serum albumin (BSA) for MRI-guided HIFU. The added silicon dioxide and BSA was included to impart ultrasound attenuation and MRI signal and thermochromic ink was also included as it changes colour from white to magenta allowing for visualisation of temperature changes following HIFU sonications. They reported the material to have T2 MRI properties similar to human tissue before heating (225 $\pm$ 14 ms at 1.5 T and 152 $\pm$ 8 ms at 3.0 T) with a decrease in relaxation times (97 $\pm$ 5 ms at 1.5 T and 86 $\pm$ 5 ms at 3.0 T) post heating.

6. Radiotherapy

6.1. Specification of material

Radiotherapy is a highly effective treatment for many cancer types. It can be delivered with either external beam radiotherapy using high energy photon, electron or hadron beams, or by placing radioactive sources inside or beside the tumor. Calibrations are commonly performed in water or water equivalent phantoms although correction factors may be required for the exact equivalency of these homogeneous water equivalent phantoms (e.g. Seco and Evans 2006, Hill *et al* 2010, Lourenço *et al* 2016, 2017, Schoenfeld *et al* 2017). These homogeneous phantoms may be employed for verifying treatment delivery although materials with electron densities and shapes that mimic patients are typically utilized for validation of techniques using anthropomorphic phantoms. For characterizing TMMs, with respect to radiation interactions, the radiation transport of both primary and secondary particles in the energy range of interest must be considered (White *et al* 1989). Interaction coefficients such as attenuation coefficients, absorption coefficients and stopping powers (SPs) have been published for body tissue and TMMs at the energies associated with radiotherapy (Snyder *et al* 1975, White *et al* 1977, Hammerstein *et al* 1979, Woodard and White 1986). These coefficients are highly dependent on material composition (Taylor *et al* 2012); ICRU 44 recommended that the chemical composition should be presented in all dosimetry reports. Figure 2 shows scattering and absorption LACs for adipose tissue and cortical bone at the energies relevant to external beam, brachytherapy and intraoperative radiotherapy.

Radiotherapy treatments are typically designed with some form of image guidance and plans are typically based on a CT image which uses a calibration curve to convert HU to relative electron density (RED) or SP. These calibration curves are typically created using TMMs. The magnitude of difference in HU or calibration curve can have a significant effect on the radiotherapy dose delivered to the patient (Thomas 1999, Seco and Evans 2006, Yohannes *et al* 2012).

6.2. Review of materials

The most advanced commercial radiotherapy phantoms specify electron densities and differences from reference attenuation coefficients across a range of materials and energies (White *et al* 1977, Snyder *et al* 1975, Hammerstein *et al* 1979, Woodard and White 1986). The limitations of these commercial phantoms can be the cost and they typically require inserts for specific dosimeters, of which there are many different types (Seco *et al* 2014, Kron *et al* 2016). Although there can be a range of phantom sizes, it is often the case

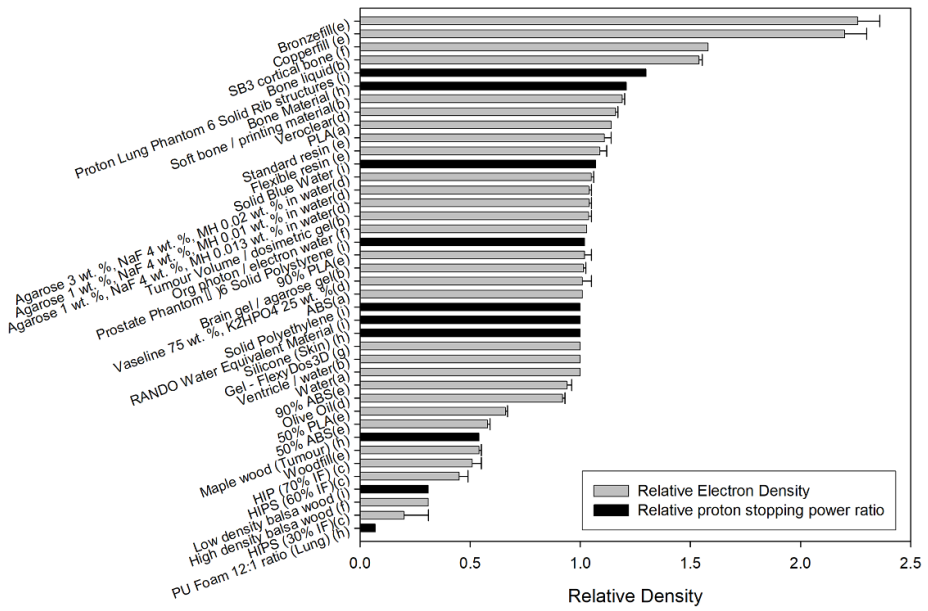

Figure 8. Relative electron densities (RED) and Relative proton stopping power ratios to water plotted for a series of TMMs where (a) Burleson *et al* (2015), (b) Gallas *et al* (2015), (c) Madamesila *et al* (2016), (d) Niebuhr *et al* (2016), (e) Dancewicz *et al* (2017), (f) Kostiukhina *et al* (2017), (g) Du *et al* (2019), (h) Perrin *et al* (2017), (i) Taylor *et al* (2016). Raw data is available in supplemetary table 4.

that the phantom will be an average human size to ensure that they are commercially viable, yet still applicable to the task. Additive manufacturing provides researchers with the tools to create bespoke radiotherapy phantoms and many of the processes in creating 3D printed radiotherapy phantoms were recently described by Tino *et al* (2019b).

Articles on in-house phantom materials were retrieved from Google Scholar and Pubmed searches of 'Anthropomorphic Phantom Development Radiotherapy' over the past 5 years. Articles were excluded if they were investigating computational phantoms or did not describe the material properties within the phantoms. Other articles have also been sourced from recent reviews on 3D printing (Filippou and Tsoumpas 2018, Tino *et al* 2019b). Figure 8 shows some materials which have been characterized in terms of RED (Burleson *et al* 2015, Gallas *et al* 2015, Niebuhr *et al* 2016, Madamesila *et al* 2016, Kostiukhina *et al* 2017, Dancewicz *et al* 2017) although in some cases Z_{eff} and mass attenuation coefficients across energy ranges are also quoted (Huamani *et al* 2019). For protons a series of relative linear stopping powers (RLSP) have been presented for phantoms used by the imaging and radiation oncology Core Houston (Taylor *et al* 2016) for audit purposes and for a motion phantom presented by Perrin *et al* (2017) (figure 8). Other methods of analysis have been characterization of the differences in measured depth dose curves compared to calculations for photons, electrons (Craft *et al* 2018, Steinmann *et al* 2018) and protons (Kim *et al* 2018a).

Radiotherapy end-to-end tests commonly use a phantom to go through the entire patient pathway from radiation treatment simulation to planning and delivery (Lehmann *et al* 2018). End-to-end tests can give confidence that the plan has been delivered to within a specified tolerance. As shown in table 5, the results can be presented using a variety of metrics, depending on the dosimeter employed (Kamomae *et al* 2017, Yea *et al* 2017, Perrin *et al* 2017, Kostiukhina *et al* 2017, Zhang *et al* 2019, Ehrbar *et al* 2019, Cunningham *et al* 2019). These metrics, include distance to agreement (DTA) between calculated and measured depth dose curves (mm), dose difference (%) or gamma analysis (%/mm). Gamma analysis is a method of comparing 2D and 3D measured and calculated dose distributions, combining the dose and space domain (Diamantopoulos *et al* 2019).

Comparison of doses recalculated on a manufactured patient specific anthropomorphic phantom with doses calculated on the original patient has also been performed (Kim *et al* 2017, Hazelaar *et al* 2018) although this does not place the same requirement on tissue characterization as when a measurement is taken as part of the end-to-end testing. In both the phantom and patient calculation the same treatment planning algorithm is used rather than performing an independent measurement. Makris *et al* 2019 performed this comparison and reported a Gamma pass rate of >97% for 1%/1 mm which was significantly better than >90% for 3%/1 mm when compared again a film measurement.

End-to-end tests are particularly useful for multi-centre audits (Clark *et al* 2015, Lambrecht *et al* 2019, Wesolowska *et al* 2019) and have shown that they are useful for comparing the magnitude of dose differences

due to effects such as motion (de Jong *et al* 2017, Kostiukhina *et al* 2017, Perrin *et al* 2017, Pallotta *et al* 2018, Ehrbar *et al* 2019) or magnetic fields (Steinmann *et al* 2019a, 2020), see table 6. Reported absolute differences can be variable depending on the dosimeter employed (Kostiukhina *et al* 2017), although it may be challenging to disassociate errors due the treatment planning system, treatment delivery, detector limitations or the material characteristics. Careful characterization of the material properties can allow explanation of the uncertainties associated with this component of any overall differences observed (Taylor *et al* 2016, Steinmann *et al* 2018). It has been demonstrated that in fact the HU-to-density calibration curve for many 3D printed materials cannot be appropriately modelled without overriding the HU (Burleson *et al* 2015, Craft *et al* 2018) and that the HU can also change over time (Craft *et al* 2018).

The radiation transport in tissue of low energy photons emitted from brachytherapy sources (e.g. ^{192}Ir, ^{137}Cs and ^{60}Co, ^{169}Yb, ^{106}Pd, ^{131}Cs and ^{125}I) and from kilovoltage x-ray generators typical in interoperative radiotherapy (Hill *et al* 2010), is governed by a superposition of the photoelectric effect and Compton scatter (Schoenfeld *et al* 2015, 2017). The different Z dependencies of LACs associated with the photoelectric effect and Compton effect (figure 2) can result in challenges in finding appropriate tissue mimicking or even water equivalent materials (Schoenfeld *et al* 2017). In brachytherapy, TG186 has placed an emphasis on the inclusion of tissue heterogeneity within dose calculations (Beaulieu *et al* 2012) with commercial planning systems starting to follow model based dose calculation algorithms. Validations have been carried out using homogeneous phantoms (Díez *et al* 2017) although the development of phantoms mimicking clinical scenarios was one of the recommendations from TG186 (Beaulieu *et al* 2012).

6.3. Limitations

Although there have been a number of authors who have investigated the chemical composition and material properties of TMMs within the radiotherapy energy range, many publications fail to present detailed material analysis before incorporating the material into end-to-end phantoms. This can leave these studies vulnerable to uncertainties due to insufficient material characterization. Density overrides within the treatment planning system can be a solution although this may not be viewed as faithfully testing the entire treatment process. As many of the phantoms are being used for CT purposes also, the advancement of heterogeneous phantoms will require better material characterization, as demostrated by Tino *et al* (2019a).

Table 6 shows a variety of reporting methods. Characterization in the form of RED for photons and RLSP for protons appears to be a uniform way to compare materials. End-to-end testing and percentage depth dose (PDD) comparison with treatment planning systems can depend on an accurately modelled dose calculation algorithm. An emerging trend to publish, or at least refer to, the composition of the material retrieved through Monte-Carlo databases or to attain the composition through scanning electron microscopes (SEM) is a hugely positive development (Huamani *et al* 2019, Steinmann *et al* 2019b). This returns to the ICRU 44 recommendation that *'the chemical composition should be included in all dosimetry and other measurement reports'* for TMMs.

6.4. Latest developments

6.4.1. MR guided radiotherapy

As discussed in section 5.1, MR guided radiotherapy exploits the superior soft tissue contrast in MR compared to current verification methods such as cone-beam CT. There has been an influx of phantoms that are compatible with CT and MR with reported properties equivalent to tissue for measuring radiation dose (Steinmann *et al* 2019b, 2019a, Gallas *et al* 2015, Ruschin *et al* 2016, Steinmann *et al* 2018, Cunningham *et al* 2019, Singhrao *et al* 2020a). Some of the materials discussed in the multi-modality section were MR and CT visible and materials were characterized in terms of RED (Gallas *et al* 2015, Niebuhr *et al* 2016, 2019). Others have carried out end-to-end testing of radiotherapy with (Cunningham *et al* 2019, Steinmann *et al* 2020) or without (Singhrao *et al* 2020a) magnetic fields.

Steinmann *et al* (2018) carried out extensive CT (HU) and MR visibility testing on a large number of materials. A number of these materials were used to test the dosimetric properties in the form of PDD film measurement comparisons with a treatment planning systems. Table 6 shows that the average DTAs were typically less than 2 mm for standard beams. Monte Carlo simulations were carried out with elemental composition obtained from SEM or previous studies and compared to film and TLD measurements (Steinmann *et al* 2019b). These TMMs formed the basis of anthropomorphic phantoms for MR guided Radiotherapy (MRgRT) dosimetry audits in the USA (Steinmann *et al* 2019a, 2020). This work was an exemplar of detailed material characterization before development of anthropomorphic phantoms for dosimetry purposes. MR only planning has the advantage of not requiring a CT scan and this places even more emphasis on the requirement for TMMs that are visible on MRI (Owrangi *et al* 2018). This is further described in section 5.1.

Table 6. Phantom measurements with anthropomorphic phantoms and TMMs where: (a) Kim *et al* (2018a) (Gammex 467 Tissue Characterization Phantom), (b) Steinmann *et al* (2018), (c) Craft and Howell (2017), (d) Kamomae *et al* (2017), (e) Zhang *et al* (2019), (f) Yea *et al* (2017), (g) Cerviño *et al* (2017), (h) Ehrbar *et al* (2019), (i) Kostiukhina *et al* (2017), (j) Perrin *et al* (2017), (k) Liao *et al* (2017), (l) Mann *et al* (2017), (m) Cunningham *et al* (2019), (n) Gholampourkashi *et al* (2018), (o) Makris *et al* (2019), (p) Pappas *et al* (2019), (q) Pallotta *et al* (2018). PDD—Percentage Depth Dose, IC—Ionization Chamber, PSD -, MC—Monte Carlo, TLD—thermoluminescent dosimeter, TPS—Treatment Planning System, E2E—End-to-end testing.

TMM	Comparison	Metric	Deviation
LN 300[(a)]	PDD, IC Array v MC/TPS	Minimum/maximum difference in measured v MC or TPS calculated Range	−1.5 mm/-21.9 mm
Adipose[(a)]			0.3 mm/1.8 mm
Breast[(a)]			−0.6 mm/-0.4 mm
Solid Water[(a)]			1.1 mm/0.3 mm
Brain[(a)]			−0.5 mm/2.8 mm
Liver[(a)]			−0.3 mm/1.7 mm
Bone material[(a)]			−0.6 mm/0.2 mm
CB2-50%[(a)]			−1.5 mm/2.6 mm
Compressed cork[(b)]	PDD, Gafchromic Film v TPS ($10x10cm^2$)	Mean deviation ($6x6cm^2$ and $3x3cm^2$ fields also presented)	1.9 ± 1.12 mm
Petroleum/Styrofoam mix[(b)]			1.0 ± 2.0 mm
Polysyrene[(b)]			1.8 ± 1.67 mm
Clear ballistic Gel #20[(b)]			0.6 ± 0.46 mm
M-F manufacture liquid PVC plastic[(b)]			1.2 ± 1.03 mm
Pt Specific Thorax Phantom—(PLA)[(c)]	PDD, IC- Exradin A1SL	Dose/Distance to Agreement	Photon < 2%, Electron < 2 mm
RANDO Head Phantom—(PLA)[(d)]	v RANDO, glass dosimeters	Dose	< ± 5% of RANDO
Pt Specific Lung Phantom[(e)]	E2E, IC	Dose	<0.5% Tumour, < 10% Spinal cord
Pt Specific Head Phantom (ABSplus)[(f)]	E2E, Gafchromic Film	Gamma	Gamma, 98%, 3%3 mm
ABS Insert for Dynamic Phantom[(g)]	E2E, IC	Gamma	<3% Static, < 5% Motion
Pt Specific Dynamic Abdominal Phantom (Silicone)[(h)]	E2E, Gafchromic Film E2E, PSD	Dose	−41%- −1% without tracking −5% +1% with tracking <2.7cGy without tracking <1.4 Gy with tracking
Dynamic Heterogeneous Lung Phantom[(i)]	E2E, IC/Gafchromic Film/TLD	Dose	<7.6% variation across detectors
Dynamic Heterogeneous Lung Phantom[(j)]	E2E, Gafchromic Film	Gamma	>90%, 4%4 mm
Pt Specific Abdominal Phantom (PVC)[(k)]	E2E, IC	Dose	<3.8% Low dose gradient <4.3% High dose gradient
Dynamic Ex-vivo Lung Phantom[(l)]	E2E, Gel	Dose	5.5 ± 6.1%
Pt Specific Pelvic Phantom[(m)]	E2E, IC	Dose	<1.5%
Dynamic Foam[(n)] (dampened sponge- 0.17 ± 0.02 kg/m^3), Silicon rubber[(n)] (1.05 ± 0.04 $kg\,m^{-3}$)	E2E, MC/Gafchromic Film	Dose/Gamma	<2% inside, < 5% outside tumour, Gamma, 94% within 2%2 mm
Pt Specific Brain Phantom[(o)]	E2E, Gafchromic Film	Gamma	>90%, 3%1 mm
Pt Specific Brain Phantom[(p)]	E2E, Gel/Gafchromic Film	Gamma	>90%, 2%2 mm
Dynamic Heterogeneous Lung Phantom[(q)]	E2E, IC/Gafchromic Film	Dose/Gamma	<1%/Gamma, >90%, 3%2 mm

6.4.2. Dynamic and deformable phantoms

Steidl *et al* 2012 developed a series of specifications for dynamic radiotherapy phantoms, one of which was to include inhomogeneities such as rib structures. Many dynamic lung phantoms have been developed with inhomogeneities (Mann *et al* 2017, Pallotta *et al* 2018, Kostiukhina *et al* 2017, Perrin *et al* 2017, Gholampourkashi *et al* 2018, Bertholet *et al* 2019). The main method of investigations with these phantoms was again end-to-end testing, although material density and relative proton SPs or relative water equivalent density measured in proton beams was also characterized in a number of studies (Perrin *et al* 2017, Kostiukhina *et al* 2017).

With abdominal dynamic or deformable phantoms, large inhomogeneities are less of an issue but soft tissue contrast across different imaging modalities can become a factor. Deformable materials such as Silicon (Ehrbar *et al* 2019) and PVC with softener (Liao *et al* 2017) have been used as abdominal TMMs with HU values similar to those measured from a reference patient. Liao *et al* (2017) investigated mechanical and HU properties for multiple PVC-softener ratios. Real-time measurements were carried out within the dynamically dEformable Liver PHAntom (ELPHA) phantom (Ehrbar *et al* 2019) where end-to-end testing demonstrated clear improvements in dose delivery accuracy following motion mitigation techniques (Ehrbar *et al* 2019). Adaptive radiotherapy is the adaption of treatment based on anatomical changes such as deformation. Phantoms such as ELPHA and that presented by Cunningham *et al* (2019) show that this is a flourishing area of phantom development, placing new requirements on TMM properties.

The results from a trial investigating Cardiac radioablation for ventricular tachycardia has shown promising results (Robinson *et al* 2019). There is no doubt that this type of treatment will require phantoms using similar materials to those described elsewhere for CT investigations (Abdullah *et al* 2018) with the added challenge of trying to measure dose using appropriate dosimeters.

6.4.3. Detectors

As well as the challenge of creating voids within phantoms to place detectors, the detectors themselves also need to be tissue equivalent or they will require correction factors (Kron *et al* 2016). Kron *et al* 2016 suggested that in terms of tissue equivalence scintillators, calorimeters and alanine are considered best with ionization chambers and diamond also rating highly. Luminesce detectors were considered variable and semi-conductor detectors were considered to have poor tissue equivalent properties. The properties associated with gel dosimeters (Baldock *et al* 2010) lend themselves to measuring volumetric dose and radiological properties demonstrated (Gorjiara *et al* 2010, Du *et al* 2019).

7. Therapeutic surgery

7.1. Specification of material

TMMs have been widely used to make surgical phantoms to facilitate clinical education, training, research, and medical device development. To simulate surgical procedures, the phantoms need to have realistic mechanical responses (force, deformation, fracture, etc) to the action of surgical tools. Such realistic mechanical responses are essential to provide haptic feedback similar to real human tissues to train clinicians and simulate the mechanical interaction between tissues and surgical tools for research. The mechanical responses depend on the mechanical properties of human tissues. Table 7 summarizes the most-commonly measured mechanical properties (Young's modulus, strength, and friction) for soft (brain, liver, prostate, kidney, muscle, and fat) and hard (cortical and cancellous bone, and calcified plaque) human tissues which can be used to guide the selection and tuning of TMMs. However, mechanical properties of human tissue are much more complex, such as hyperelasticity, viscoelasticity, and heterogeneity, and quantitative comparison on the surgical performance of the TMMs to that of human tissue are required for validation.

7.2. Review of materials

Phantom materials for theraputic surgies were divided into two groups: soft TMMs and hard TMMs. A literature search was performed in Google Scholar and Pubmed over the past 5 years although well characterized 'classic' materials often referred to in the literature were also included. For the soft TMMs, the search keywords were 'tissue phantom', 'tissue surrogate', 'tissue analogue', 'simulator', and 'needle insertion'. For the hard TMMs, the search keywords were 'bone surrogate', 'bone analogue', 'bone simulator', and 'plaque analogue'. Articles were excluded if they only studied the surgical process without detailed description of the phantom specifications.

7.2.1. TMM for soft tissue in surgical procedures

Both biopolymers and synthesized polymers are used to mimic soft tissue to make surgical phantoms. The biopolymers, such as PVA, gellan gum, agar, and gelatin, have similar mechanical properties to the soft

Table 7. Mechanical properties of seven common types of human tissues from prior studies. Data taken from (a) Taylor and Miller (2004), (b) Zwirner *et al* (2019), (c) Yeh *et al* (2002), (d) Brunon *et al* (2010), (e) de Jong *et al* (2017), (f) Thomas *et al* (1998), (g) Parker *et al* (1993), (h) Umale *et al* (2013), (i) Snedeker *et al* (2005), (j) Kot *et al* (2012), (k) Fukushima and Naemura (2014), (l) Iivarinen *et al* (2014), (m) Chong *et al* (2007b), (n) Bayraktar *et al* (2004), (o) Giesen *et al* (2001), (p) Schoenfeld *et al* (1974) and (p) Riel *et al* (2014).

Human tissue	Elastic modulus (kPa)	Strength (MPa)	Friction force in needle insertion (N m^{-1})
Brain	0.58[(a)]	7 (brain dura)[(b)]	—
Liver	0.64–1.7[(c)]	1.9 (liver capsule)[(d)]	0.011, 1.3 mm needle[(e)]
Prostate	38–96[(f)], 14–40[(g)]	—	—
Kidney	15 (kidney cortex)[(h)]	9.0 (kidney capsule)[(i)]	—
Muscle	13–32[(j)]	—	0.15, 1.6 mm needle (porcine)[(j)]
Fat	2.5 [(l)]	—	—
Cortical bone	1.3×10^7–1.8×10^7 [(m)], 2.0×10^7 [(n)]	58–132[(m)]	—
Cancellous bone	1.3×10^5-4.3×10^5 [(o)]	0.1–13[(q)], 1.6–4.5[(o)]	
Calcified plaque	—	62[(p)]	

tissues as both have high water content (Chen and Shih 2013). However, such biopolymers may suffer from degradation due to water evaporation. Mechanical properties of biopolymers may change over time and changes with temperature. They also suffer from toxic additives, which are added in order to increase the shelf life. On the contrary, synthetic polymers, such as PVC and silicone, do not have water within the structure and therefore generally have more stable properties, as well as a longer shelf life. However, the lack of water often resulted in a higher friction coefficient compared to that of soft tissues, requiring the addition of lubricant, such as mineral oil as part of the composition (Li *et al* 2015b, 2016). For both biopolymers and synthetic polymers, additives, such as glass beads, are usually added to TMMs to enhance the scattering effect to better mimic the imaging apperance of biological tissues (Li *et al* 2015b, 2016). A summary of the soft TMMs discussed is shown in table 8.

PVA is a biocompatible hydrogel that has been widely used in tissue engineering (Kumar and Han 2017). PVA phantoms to simulate needle insertion on different organs (liver, kidney, and prostate) have been developed at Tianjin University (Jiang *et al* 2011, 2013, Li *et al* 2015a, 2018). PVA polymer solution is made by dissolving PVA powder in water and heating to about 90 °C (Forte *et al* 2016, Li *et al* 2018). The solution is then cooled down, transferred to a mould, and applied with FT cycles, which change the hydrogel structure and cure PVA (Vrana *et al* 2008). The Young's modulus increases with PVA concentration and FT cycle number (Melnyk *et al* 2019), making PVA capable to mimic a range of soft tissues by varying the concentration and FT cycle numbers. PVA is also transparent and has been used to study the tissue deformation in the needle insertion procedures (Jiang *et al* 2011). In the same study, PVA's micro-structure, tensile strength, and needle insertion were studied and showed a great similarity to those of porcine liver.

Recent studies have investigated composite hydrogel by mixing PVA with different ratios in order to produce soft tissue phantoms with a large range of applications. A group in Imperial College London mixed PVA with phytagel (PHY) to make brain phantoms to mimic the brain incision and the brain shift due to the loss of cerebrospinal fluid during neurosurgical procedures for surgical trainings (Forte *et al* 2016, 2018). By adjusting the ratios between PVA and PHY, they were able to manufacture TMMs to mimic brain, lung, and liver (Tan *et al* 2018). Due to the low curing temperature of PVA and PHY, 3D cryogenic printing with such mixture is also possible and the 3D printed parts demonstrated similar mechanical properties compared to the casted ones (Tan *et al* 2017). Besides PHY, PVA can also be mixed with agar at different concentrations to mimic cancerous, normal, and benign prostate hyperplasia for the transurethral resection of the prostate (TURP) procedure (Choi *et al* 2020). Another two biopolymers for soft surgical phantoms are gellan gum and gelatin. Gellan gum was mixed with propylene glycol and NaCl at different concentrations to match the mechanical, thermal, and electrical properties of porcine spinal cord and liver (Chen and Shih 2013), making gellan gum a good TMM for electrosurgery. Gelatin has shown to be a good TMM for needle insertion in brain (Leibinger *et al* 2016) and the Young's modulus can be tuned from 3 kPa to 25 kPa by varying its concentration (Forte *et al* 2015).

For synthetic polymers, PVC and silicone have been studied. PVC has high transparency, making it ideal to observe the tissue interaction with surgical tools, such as the deformation of needle during biopsy procedure (Li *et al* 2020). To prepare the PVC phantom, vinyl chloride solution is heated to 150 °C to promote optimum polymerization (Li *et al* 2016). The solution is then poured to a mould to cool down and cast the shape of a specific tissue. To fabricate phantoms with different elastic modulus, softener was added and resulted in elastic modulus of 3–200 kPa (Hungr *et al* 2012). The mechanical and imaging properties of

Table 8. TMMs for soft tissue used to simulate surgical procedures where (a) Jiang *et al* (2011), (b) Jiang *et al* (2013), (c) Li *et al* (2015a), (d) de Jong *et al* (2017), (e) Melnyk *et al* (2019), (f) Forte *et al* (2016), (g) Leibinger *et al* (2016), (h) Tan *et al* (2018), (i) Choi *et al* (2020), (j) Chen and Shih (2013), (k) Leibinger *et al* (2016), (l) Hungr *et al* (2012), (m) Li *et al* (2015b, 2016), (n) silicone (Wang *et al* 2014), (o) Hollensteiner *et al* (2014). DMSO: dimethyl-sulfoxide, ECH: epichlorohydrin, TURP: transurethral resection of the prostate, PPG: propylene glycol.

Tissue sample	TMM	Surgical procedure	Young's modulus (kPa)	Concentration/ preparation	Additives
Porcine liver[a]	PVA	Needle insertion	3.6–11	3%, 1–5 FT cycles	DMSO
Porcine kidney[b]	PVA	Needle insertion	30–116	8 g dl^{-1}, 7 FT cycles	DMSO and NaCl
Human prostate[c]	PVA	Needle insertion	—	3%, 7 FT cycles	DMSO, NaCl, NaOH, ECH
Human liver[d]	PVA	Needle insertion	—	4%, 2 FT cycles	—
Porcine kidney[e]	PVA	Nephrectomy	81–101	7-10%, 1–3 FT cycles	—
Porcine brain[f]	Composite hydrogel	Cutting	—	3% PVA + 0.4% PHY; 1% + 0.4% PHY	—
Porcine brain[g]	Composite hydrogel	Needle insertion	1.4	1.5% PVA + 0.4% PHY	Resin beads
Porcine brain, lung, and liver[h]	Composite hydrogel	Needle insertion	0.5–10	0–2.5% PVA + 1.3%-7.5% PHY	—
Human prostate (no tests)[i]	Composite hydrogel	TURP	35–155	0.8% PVA + 0.8%-1.8% agar	Glass beads
Porcine spinal cord and liver[j]	Gellan gum	Electrosurgery	4.7–17	1%-4% gellan gum + 0%–40% PPG + 0.05%-0.2% NaCl	Sodium propionate
Porcine brain[k]	Gelatin	Needle insertion	1.4	3.4% gelatin powder	—
Human prostate[l]	PVC	Needle insertion	3–200	PVC + 0%–90% softener	—
Human muscle and prostate[m]	PVC	Needle insertion	6–45	PVC + 0%–100% softener	1%–5% mineral oil and 0%–1% glass beads
Porcine fat, liver, and muscle[n]	Silicone	Needle insertion	10–21	—	0%–40% mineral oil
Human muscle[o]	Silicone	Needle insertion	—	—	40%-60% silicone oil

Table 9. TMMs for hard tissues used to simulate surgical procedures. Data taken from (a) O'Neill *et al* (2012), (b) Fuerst *et al* (2012), (c) Hollensteiner *et al* (2015), (d) Acker *et al* (2016), (e) Macavelia *et al* (2012), (f) Hollensteiner *et al* (2017, 2018, 2019), (g) Tai *et al* (2015, 2016, 2018), (h) Riel *et al* (2014), Lyu *et al* (2019).

TMM	Surgical procedure	Tissue sample	TMM specification
Sawbones[(a)]	Bone screw implant	Human femoral head	0.16 and 0.08 g cm^{-3} PU foam
Sawbones[(b)]	Vertebroplasty and kyphoplasty	Human vertebrae	0.16–0.48 g cm^{-3} PU foam
Sawbones[(c)]	Kyphoplasty	Human trabecular bone	0.08–0.24 g cm^{-3} PU foam
Sawbones[(d)]	Bone screw implant	-	0.48 g cm^{-3} PU foam
Sawbones [(e)]	Bone drilling	Human femur	0.27 g cm^{-3} PU foam/epoxy coating
PU-based composite[(f)]	Bone drilling, milling, sawing, and screw implant	Human parietal bone	PU with 0%–50% calcium-carbonate
3D polymer-infiltrated composite[(g)]	Bone drilling and grinding	Human tibia bone, bovine cortical bone	VisiJet® PXL Core plaster (calcium sulfate hemihydrate) + RBC® 3200 epoxy
Plaster[(h)]	Percutaneous intervention	Human calcified plaque	Ultracal® 30 plaster (calcium sulfate hemihydrate)

PVC have been studied and showed a good potential as a multimodal (to mimic both imaging and mechanical properties) TMM (Li *et al* 2016).

Another type of synthetic polymers for soft tissue is silicone, which has the combined advantages for PVA and PVC of being both biocompatible and stable. In addition, silicone is room-temperature vulcanizing and therefore the preparation of silicone is much easier compared to PVA and PVC, without the need of freezing or heating. However, the friction between surgical tools and silicone is very high. Therefore, mineral oil (Wang *et al* 2014) or silicone oil (Hollensteiner *et al* 2014) was added to reduce the coefficient of friction for TMM silicone. As much as 40 wt% of mineral oil was used in order to match the needle insertion forces and tissue elastic modulus (Wang *et al* 2014). This high mineral oil concentration is close to the saturation point and could add to the manufacturing difficulty.

7.2.2. TMM for hard tissue in surgical procedures

Table 9 summarizes the TMMs used for two types of hard tissue: bone and calcified plaque. One of the most widely used TMMs for bone is the commercial product Sawbones® developed by Pacific Research Laboratory (Vashon Island, Washington USA). The modulus, strength, and fatigue property of the commercial femur and tibias bone analogs have shown to be similar to that of human bones (Chong *et al* 2007a, Heiner 2008). The Sawbones® TMMs have a porous inner layer made of PU foam to mimic the cancellous bone and an outer layer made of epoxy mixed with e-glass fibers to mimic the cortical bone. The outer layer has similar elastic modulus (10–17 GPa) and strength (93–157 MPa) to those of human cortical bone (Sawbones 2016). In Europe, the PU foam Synbone® TMMs are popular for surgical simulation. The density of the PU foam can be adjusted to mimic normal and osteoporotic bones (O'Neill *et al* 2012, Fuerst *et al* 2012, Hollensteiner *et al* 2015, Acker *et al* 2016) with Young's modulus of 0.02–1.1 GPa and strength of 0.6–48 MPa (Sawbones 2016). However, the Sawbones® is still weaker than human femur in the bone drilling process (Macavelia *et al* 2012). This discrepancy may be due to the inherent differences between epoxy and human cortical bone. Hollensteiner *et al* (2017, 2018, 2019) proposed another PU foam-based bone analog with the inner cancellous layer made from PU foam filled with water and the outer cortical layer made from PU foam with mineral-based fillers. This bone analog demonstrated similar performance in drilling, milling, sawing, and screw implant compared to the haptic responses of human parietal bone. For both of PU foam-based bone analogs, the shape is either standard block or molded into pre-defined anatomical geometry, limiting the flexibility of making patient-specific geometries.

To fill the gap, another bone analog was developed by a 3D printing process called binder jetting. In this process, binder is deposited on a thin layer of plaster powder. Layer-by-layer, a porous structure is fabricated. This porous structure was then strengthened by soaking in salt water, cyanoacrylate, or epoxy (Tai *et al* 2018). The final product is a 3D polymer-infiltrated composite (3DPIC) and its Young's modulus (2.5–6.2 GPa) and strength (3.6–12 MPa) are within the range of human cortical and cancellous bone, and its similarity to human tibia bone has been validated by drilling and grinding studies (Tai *et al* 2015, 2016, 2018).

Another TMM for hard tissue is the calcified plaque analog used for research in percutaneous interventions to open narrowed blood vessels. Riel *et al* (2014) used plaster to mold an analog and it demonstrated a similar Young's modulus (15 GPa), compressive strength (36 MPa), and porosity to those of human calcified plaque. Such calcified plaque analog has been used to study the plaque grinding in atherectomy (Lyu *et al* 2019).

7.3. Limitations

Three limitations exist in TMMs for surgical phantoms. First, the aforementioned TMMs, except the 3DPIC TMMs for bone, all have isotropic structures while the human tissues are naturally anisotropic. Both soft tissue (Holzapfel *et al* 2004) and bone (Giesen *et al* 2001) have demonstrated higher modulus and strength along the fibre direction compared to that perpendicular to the fibre direction. Second, TMMs mostly are homogenous while the human tissues are heterogenous, as indicated by the range of mechanical properties shown in table 7. The mechanical properties of the same piece of tissue maybe different at different locations. Finally, most of the TMMs are molded to a designed shape. It can be time-consuming and costly for fabrication TMMs to patient-specific geometries. In addition, replicating geometric features of human tissue, such as internal structures of an organ, is challenging using the molding technique.

7.4. Latest developments

Future work should be focussed in three directions. First, 3D printing is the emerging method to print different printable TMMs to patient-specific geometries. Second, the heterogeneity of human tissues should be quantified and replicated by 3D printing to fabricate surgical phantoms. Additives, such as glass beads, used to enhance the imaging properties of TMMs may also be used to increase the heterogeneity of TMM but the effect on mechanical properties and heterogeneity need to be quantified to match that of human tissue. Finally, new 3D printable TMMs could be developed to print phantoms with anisotropic and heterogeneous properties in patient-specific geometries for customized healthcare research and services.

Table 10. Thermal properties at room temperature for soft tissues and bone. Values for thermal conductivity and specific heat capacity have been taken from the IT'IS database and reported as mean values ± standard deviation (Hasgall *et al* 2018). Data taken from (a) Giering *et al* (1995), (b) El-Brawany *et al* (2009), (c) Rossmann and Haemmerich (2014), (d) Rodríguez *et al* (2002).

Tissue type	Thermal conductivity (W m^{-1} K^{-1})	Specific heat capacity (J kg^{-1} K^{-1})	Thermal diffusivity (mm^2 s^{-1})
Skin[(a)]	0.37 ± 0.06	3391 ± 233	0.04–0.16
Muscle[(b)]	0.49 ± 0.04	3421 ± 460	0.16
Brain[(a)]	0.51 ± 0.02	3630 ± 74	0.13–0.14
Breast[(c)]	0.21	2348 ± 372	0.14
Liver[(c)]	0.52 ± 0.03	3540 ± 119	0.14
Bone[(d)]	0.32 ± 0.03	1313 ± 295	0.44–0.54

8. Thermal therapies

8.1. Specification of material

Thermal therapies are treatments which use heat to generate a therapeutic effect. Thermal therapies can be divided in two main categories: hyperthermia and thermal ablation. In hyperthermia, the temperature is increased up to levels of 43 °C–45 °C for a time generally in the order of minutes. Hyperthermia has been shown to improve healing (Ibelli *et al* 2018) or increase sensitivity to radiotherapy and chemotherapy in cancer treatment (Durando *et al* 2019).

In thermal ablation, the temperature of the target region is increased to higher levels (generally above 56 °C) for a short time, usually in the order of seconds, to cause cell death through mechanisms such as autophagy, apoptosis and necroptosis (Mouratidis *et al* 2015). Ablation therapies have been used in different clinical applications, including the treatment of atrial fibrillation (Marrouche *et al* 2018), treatment of phantom limbs after amputation (Guo *et al* 2019), tumours (Rodrigues *et al* 2015) and uterine fibroids (Napoli *et al* 2017), as well as neurosurgery (Quadri *et al* 2018) .

Thermal treatments can be applied with minimally invasive techniques though needles or catheters or using externally applied generators. The most common sources of energy are ultrasound, a technique referred to as high-intensity focused ultrasound (*HIFU*) or focused ultrasound surgery (FUS), or electromagnetic, radiofrequency, microwave, or optical, through the employment of laser radiation (Dabbagh *et al* 2014b).

The recent growing interest in such strategies have spurred the development of different materials to test and validate ablation therapies. Apart from the obvious capability of withstanding ablation temperatures, the materials need to mimic all the properties required for the relevant application method and, at least, the thermal properties to mimic the deposition of energy conduction and diffusion of heat. In addition to the acoustic properties referred in section 4, ablation phantoms should mimic properties relevant for high intensity exposures, such as the non-linearity parameter (Zeqiri *et al* 2015) and the cavitation threshold.

Electrical conductivity and permittivity, as well as electrical impedance and relaxation time may influence the efficiency of electromagnetic therapies, while penetration depth and optical scattering are relevant parameters for laser induced thermal treatments (Dabbagh *et al* 2014b). Reference values for thermal conductivity, specific heat capacity and thermal diffusivity for five soft tissues and bone are presented in table 10.

8.2. Review of materials

Articles were retrieved from Google Scholar and Pubmed searches of the words 'Tissue Mimicking Materials' and 'Phantoms' in combination with the words 'Hyperthermia', 'Thermal therapies', 'HIFU', 'Thermochromic', 'Ablation'. The focus was on articles published over the past 5 years. TMMs for thermal therapies are used for quality assurance on equipment in clinical use, or to verify the deposition and distribution of heat for new techniques or devices. Two main categories can be identified: the TMMs which use external measurement techniques for real time monitoring of the temperature or those with embedded thermocouples (King *et al* 2011) and thermochromic materials. TMMs are generally based on hydrogels, such as agar or gellan gum (Chen and Shih 2013), Multimodality phantoms are also used to mimic both acoustic and electromagnetic properties of tissues, sometimes with the addition of salt (Fiaschetti *et al* 2018). In table 11, the values of thermal conductivity, specific heat capacity and thermal diffusivity for some soft tissues TMMs used for ablation therapies are reported.

8.2.1. TMMs for real time measurements

Real-time temperature measurement experiments play a significant role in the maintenance of equipment and in the development and assessment of new ablation techniques. The current gold standard for real-time monitoring is MR-thermometry (Rieke and Butts Pauly 2008) which uses temperature sensitive MR

Table 11. Thermal properties at room temperature for soft tissues mimicking material. Data taken from (a) Hanks *et al* (2019), (b) Ikejimba *et al* (2016), (c) Choi *et al* (2013), (d) Dunmire *et al* (2013) (e) Farrer *et al* (2015), (f) Tai *et al* (2018), (g), Menikou and Damianou (2017), (h) Dabbagh *et al* (2014a), (i) un-house material. * Properties reported as function of temperature, **MJ/mm^{3}K.

Soft tissue mimicking material	Thermal conductivity (W m^{-1} K^{-1})	Specific heat capacity (J kg^{-1} K^{-1})	Thermal diffusivity (mm^2 s^{-1})
Thermochromic ink polyacrylamide[a,b]	0.59	3939	0.143 ± 0.002
BSA polyacrylamide[c]	0.654 ± 0.033	3597 ± 540	0.182 ± 0.025
Agar/Gelatine[d] *	0.0025 T + 0.5484	$-6e^5T^2$ + 0.0115 T + 3.1867**	0.0004 T + 0.1679
Gelatine[e]	–	3635 ± 88	0.143 ± 0.003
Gellan Gum[f]	0.483 ± 0.012	3550 ± 46	0.133 ± 0.003
Agar—evaporated milk[g]	0.57 ± 0.10	4090	0.13 ± 0.01
NIPAM[h]	0.60 ± 0.02	3680 ± 220	—
IEC 60601-2-37 Agar[i]	0.58 ± 0.058	3770 ± 377	0.15 ± 0.015

parameters such as the proton resonance frequency, the diffusion coefficient, $T1$ and $T2$ relaxation times, magnetization transfer and the proton density. Examples of TMMs for MR-thermometry are based on evaporated milk and ballistic gel (Farrer *et al* 2015), agar-silica soft tissue mimic (Menikou *et al* 2016) and PVA-based soft-tissue mimic (Cao *et al* 2019). These TMMs show similar acoustic properties, along with MR ($T1$ and $T2^*$), mechanical and thermal properties and are widely used for QA of MRgFUS (Menikou *et al* 2015) as discussed in section 5.3. They can be used to manufacture anthropomorphic phantoms which are compatible with different imaging modalities, such as CT and diagnostic ultrasound (Lindner *et al* 2010). 3D-printed materials such as ABS have been used to mimic bone (Menikou *et al* 2015). TMMs are in use to validate thermal therapies that use diagnostic ultrasound as monitoring techniques (Alvarenga *et al* 2017). These techniques are based on the variation of speed of sound and BSC with temperature and are therefore reliant on the presence of ultrasound scatterers which are mimicked by the inclusion of micro-nano particles such as aluminium oxide and silicon carbide to hydrogels (IEC 2007). Finally, the IEC agar material has been used to produce phantoms for visualization of the thermal field generated by ultrasound transducers using infrared cameras (Miloro *et al* 2016), due to the similarity of infrared emissivity of the gel to soft tissues.

8.2.2. Thermochromic materials

Thermochromic materials change colour when they reach a specific temperature. The change can be either reversible or permanent. Reversible changes must be recorded immediately after exposure, while irreversible colour variations offer more time for analysis at the cost of single use of the gels. These materials have the capability to provide 3D visualization of the heat deposition, even if only the maximum temperature reached is visible and temporal information is lost.

Thermochromic TMMs with permanent change in temperature must be based on jellification processes occurring at low temperatures, to avoid the activation of the thermochromic agent. Silicone-based materials have been developed (Costa *et al* 2016). However, polyacrylamide-based gels, formed of acrylamide monomer cross-linked using a polymerization agent are the most common base for thermochromic TMMs (Choi *et al* 2013). The resulting gel shows similar thermal properties as soft tissues (thermal conductivity 0.65 W m^{-1} K^{-1}, specific heat capacity 3300 J kg^{-1} K^{-1}, thermal diffusivity 0.18 mm^2 s^{-1}) and is optically transparent. However, while polyacrylamide is safe, its monomer is a neurotoxic substance, likely to be carcinogenic (Besaratinia and Pfeifer 2007).

Thermochromic agents are added before jellification. Natural proteins such as BSA are commonly used. When the denaturation temperature of the protein is reached, the gels turn opaque, allowing a 3D visualization of the target region. The denaturation temperature can be adjusted by modifying the pH of the gel (Brodin *et al* 2016). Eggs albumin is also used in the fabrication of TMMs, as it shows favourable properties for testing laser ablation (Geoghegan *et al* 2019). In recent years, thermochromic inks such as MB Magenta NH 60 °C concentrate (LCR Hallcrest, LLC, USA) have gained success for both electromagnetic (Negussie *et al* 2016) and ultrasound thermal therapies (Eranki *et al* 2019), even with the use of endoscopes (Hanks *et al* 2019). The resulting phantoms lose their transparency, but the colour change is gradual over a temperature range (usually around 10 °C–20 °C) and reaches saturation at temperatures between 50 °C and 90 °C, depending on the ink employed.

Reversible changes have been obtained using non-ionic surface-active agents such as N-isopropylacrylamide (NIPAM) and PolyNIPAM (Dabbagh *et al* 2014a). These copolymers exhibit cloud points near physiologically relevant temperatures. The resulting colour change is reversible but present a large hysteresis allowing more time for the image analysis (Shieh *et al* 2014).

8.3. Limitations

The main limitation of the existing experimental setups is the lack of perfusion. In fact, blood perfusion in living organs plays a significant role in heat deposition and temperature distribution (Wang *et al* 2019). Although efforts are going in this direction (Kamphuis *et al* 2020) the complexity of mimicking such a condition is still a big challenge.The variation of all the material properties with temperature is extremely important (Rossmann and Haemmerich 2014) due to the nature of the application. However, the availability of these data on tissues is very limited due to challenges in performing the experiments (Guntur *et al* 2013). This implies that the mimicking capabilities reduce as temperature changes and the differences can be significant for large temperature variations or when denaturation occurs.

8.4. Latest devopments

TMMs designed for HIFU exposure are commercially available (Onda Corporation, Sunnyvale, USA). This material has acoustic (speed of sound 1600 m s^{-1}, acoustic attenuation 0.6 dB cm^{-1} MHz^{-1}) and thermal (thermal conductivity 0.55 W m^{-1} K^{-1}, specific heat capacity 3850 J kg^{-1} K^{-1}) properties that mimic soft tissue and changes colour when the temperature exceeds 70 °C. Thermosensitive nanomaterials present a natural evolution and an interesting field of research for thermal therapy phantoms. Recently, liposomes sensitive to temperature have been used in hydrogels (Kim *et al* 2018b). The change of colour is almost linear between 40 °C and 70 °C. Contrast agents with signal enhancement proportional to the temperature have been studied (Maruyama *et al* 2016), but their use in phantoms is still limited. Hydrogels in combination with sheets of liquid crystal (Thipayawat *et al* 2019) have also been recently explored.

9. Conclusions and outlook

This review has summarized the recent TMMs that have been developed for phantoms involving a diverse range of the latest imaging and therapeutic applications. Over 250 TMMs have been discussed in this review. Common themes have emerged and it is clear that materials such as plastics, gels, silicones, PVC, resins and liquids are typically employed to mimic soft tissue. Bone and lung have mostly been studied in surgery and ionizing imaging applications although investigations are becoming more common in other areas. Each imaging and therapeutic modality has specifications which are specific to not only the modality, but also the application. Combining these specifications is being increasingly investigated with the upsurge of multimodality imaging and image guidance in therapeutic procedures.

The emergence of 3D printing has resulted in materials which could be classed as TMMs (Filippou and Tsoumpas 2018, Tino *et al* 2019b). However, many of the phantoms created using 3D printing technology actually use voids to fill with TMMs due to the time required to print large volumes and also the limtations of material properties. Print times are now reducing and new materials being developed. However, as also mentioned in previous reviews, the development of materials could be more focussed towards TMMs.

Commercial phantoms have the advantage of having reproducible stable material properties although these should continue to be tested robustly across phantoms which are marketed to have the same material. However, with increasing materials and manufacturing techniques, the potential to create in-house patient specific phantoms has often been realised. It is important that the materials used within these phantoms are investigated to an appropriate standard to allow future investigations and progress to be made in further development of materials published. Validation across batches of materials and tests over time are just some of the conditions that should be investigated although many tests are application dependent and have been discussed in detail in each section of this review.

The development of materials with different concentrations is not a new concept. However, not all researchers publish the development of the specific material investigated. With the emergence of more materials, further ‘mixtures’ are being developed by varying concentrations of different materials. Many examples are presented in the surgery section and a recent review (Li *et al* 2018) provides guidance on robust development and testing of materials. The mechanical properties of many materials with incremental additives have been investigated although the addition of futher materials to allow visibility in imaging also requires validation. Ultrasound has shown that publishing detailed properties of materials and imaging results can aide in the development TMMs. In ionizing imaging investigations have been carried out to vary concentrations of softener within PVC (Liao *et al* 2017), and also iodine within ink (Jahnke *et al* 2016) resulting in a variation in the material densities and therefore the CT numbers (HU). Within 3D printing, infusing different materials (Filippou and Tsoumpas 2018, Tino *et al* 2019b) and investigating different infills (Madamesila *et al* 2016, Dancewicz *et al* 2017, Tino *et al* 2019a) have been investigated. Within thermal therapies, TMMs have been investigated with different contrast agent concentrations (Maruyama *et al* 2016) and ultrasound scatterers reporting changes with temperature. It is important that these experiments are carried out under the correct environmental conditions and over time. Factors such as temperature can

significantly affect the experimental results as demonstrated in ultrasound. Publishing the concentrations, calibration data and environmental conditions allows other researchers to reproduce the experiment to validate the material under specified conditions.

There is no perfect material to simulate tissue. With the variation in tissue composition across different humans, the aim to replicate tissue seems an impossible task. However, with each innovation in manufacturing technology and material science, new possibilities are presented to develop materials that may come closer to human tissue. Each TMM developed has properties which are highly dependent on the application. Many TMMs aim to simulate tissue from an 'average human' although others have aimed to replicate properties of a specific patient or cohort of patients, again depending on the application. Typical values depend on biological factors, including age, disease state and ethnicity, as well as the measurement or imaging techniques employed. Similarly, mechanical properties of human tissue are extremely complex with a wide variation in hyperelasticity, viscoelasticity, and heterogeneity across patients, organs and even within organs.

Multi-modality imaging is becoming routine in a number of disciplines and is emerging in others. This has resulted in new requirements for the visibilty of materials across different imaging modalities. The improved soft tissue definition in imaging, offered by MR and ultrasound, is being used during radiotherapy treatments and many phantoms have been developed to ensure optimal visualization of tissue that was not previously possible. Similarly, in surgery additives, such as glass beads, are usually added to TMMs to enhance the scattering effect to better mimic the imaging apperance of biological tissues (Li *et al* 2015b, 2016). As therapeutic applications rely even further on imaging, it is clear that more collaboration across modalities is required.

As imaging moves towards the capture of function over time, including movement and deformation of organs through 4D imaging, more effort is necessary to characterize the materials in many more ways than previously required. Much can be learned from surgery where mechanical properties are part of the fabric of testing TMMs. Other functional aspects such as perfusion are also presenting challenges in developing TMMs in many disciplines (Kamphuis *et al* 2020). Phantoms for testing imaging techniques quantifying blood perfusion must have a complex flow and perfusion system and should simulate spatially distributed small vessels with various different flow directions (Eriksson *et al* 1995). An overview of perfusion phantoms including ultrasound, MRI, CT and PET applications has recently been published (Kamphuis *et al* 2020).

In ionizing imaging and MR, there is now more of a requirement for phantoms with 'anatomical' texture and structures. A recent study showed that combinations of liquids, gels and solids are typically used for heterogeneous phantoms and that these 'standardization objects' could be critical to ensuring stable radiomics models across institutions (Valladares *et al* 2020). Texture has been inherent within most mammography and ultrasound TMMs and although this is being advanced with techniques such as DBT, much can be learned from the experience of both developing and testing textured materials. The emergence of radiomics (Kalendralis *et al* 2019) may be a way to match the heterogeneity of the investigated material with tissue, although more traditional methods such as comparisons with the Noise Power Spectrum (Cockmartin *et al* 2013) may be investigated in the first instance.

Although a wide range of imaging and therapeutic modalities have been discussed within this review, not all modalities could be covered. Pogue and Patterson (2006) published TMMs for on optical spectroscopy, imaging, and dosimetry and, although beyond the scope of this review, there is no doubt that an updated review in this area would be welcome. The review that we have presented investigates CT although modalities such as planar x-rays have not been investigated. Similarly, existing imaging and therapeutic modalities are constantly evolving, with improving hardware and software. With this evolution it is important that the TMM specifications that are developed in the future are appropriate for the application, with the ultimate aim of improving patient care.

In many established and emerging imaging and therapeutic fields there is a lack of a 'gold standard' for comparison. Indeed the need for standardization is a key conclusion that has come from this review. In ultrasound a set of standards (IEC 2007) are typically referenced in the development of TMMs. However, even within the ultrasound modality, the emergence of new modalities such as CEUS will require new specifications. Imaging with ionising radiation and radiotherapy rely on key references such as NIST databases, ICRU 44 and ICRU 46 for comparing attenuation coefficients of TMMs developed (White *et al* 1989, 1992, Berger *et al* 2010). Simulations of the effect of variable energies on the properties of reference or investigated materials has been facilitated by software, although the material composition is also required (Taylor *et al* 2012, Fitzgerald *et al* 2017). MRI, surgery or thermal therapies do not have offical standards under which to create TMMs. Only surgery has published guidance on developing TMMs (Li *et al* 2018). Within this review, we have presented a series of specifications that have been utilized by researchers in recent years. These have been highly dependent on the application of the therapy or imaging involved. The

specifications are by no means standards, but it is hoped that this review will facilitate the discussion on the requirement standards for developing TMMs, such as those available for ultrasound.

Looking forward, it is hoped that this review will serve as a testbed for cross-fertilization of materials. There is commonality in approaches in developing and testing materials. It is clear that repurposing of materials across modalities is something that should not only be encouraged but will also become essential as multimodality imaging and image guided therapeutic technologies continue to evolve. As discussed throughout the review, new imaging and therapeutic modalities are emerging during this technological revolution. The quest to develop the most realistic TMMs continues although this review has shown that collaboration, setting standards and publishing the experiments rather than just the final TMM will advance this fluorishing area of material development for tissue phantoms.

Acknowledgments

This work was supported by the National Measurement System of the UK's Department for Business, Energy and Industrial Strategy. Thanks to Dr Christina Agnew for helpful comments on the manuscript.

ORCID iDs

Yang Liu https://orcid.org/0000-0002-9132-0258
Piero Miloro https://orcid.org/0000-0001-6809-2296
Catharine H Clark https://orcid.org/0000-0003-2287-8212

References

Abdullah K A, Mcentee M F, Reed W and Kench P L 2018 Development of an organ-specific insert phantom generated using a 3D printer for investigations of cardiac computed tomography protocols *J. Med. Radiat. Sci.* **65** 175–83

Acker W B, Tai B L, Belmont B, Shih A J, Irwin T A and Holmes J R 2016 Two-finger tightness: what is it? Measuring torque and reproducibility in a simulated model *J. Orthop. Trauma* **30** 273–7

Ai H A, Meier J G and Wendt R E 2018 HU deviation in lung and bone tissues: characterization and a corrective strategy *Med. Phys.* **45** 2108–18

Alssabbagh M, Tajuddin A A, Abdulmanap M and Zainon R 2017 Evaluation of 3D printing materials for fabrication of a novel multi-functional 3D thyroid phantom for medical dosimetry and image quality *Radiat. Phys. Chem.* **135** 106–12

Alvarenga A V, Wilkens V, Georg O and Costa-Félix R P B 2017 Non-invasive estimation of temperature during physiotherapeutic ultrasound application using the average gray-level content of B-mode images: a metrological approach *Ultrasound Med. Biol.* **43** 1938–52

Alva-Sánchez H, Quintana-Bautista C, Martínez-Dávalos A, Ávila-Rodríguez M A and Rodríguez-Villafuerte M 2016 Positron range in tissue-equivalent materials: experimental microPET studies *Phys. Med. Biol.* **61** 6307

Amin N A B, Abualroos N J and Zainon R 2020 Fabrication of anthropomorphic thyroid-neck phantom for dosimetry study in nuclear medicine *Radiat. Phys. Chem.* **166** 108462

Anderson J J *et al* 2010 Interlaboratory comparison of backscatter coefficient estimates for tissue-mimicking phantoms *Ultrason. Imaging* **32** 48–64

Arabul M U, Heres H M, Rutten M, van de Vosse F N and Lopata R G P. 2015 Optical absorbance measurements and photoacoustic evaluation of freeze-thawed polyvinyl-alcohol vessel phantoms *Proc. SPIE* vol **9323**

Badal A, Clark M and Ghammraoui B 2018 Reproducing two-dimensional mammograms with three-dimensional printed phantoms *J. Med. Imaging.* **5** 33501

Bakaric M, Miloro P, Zeqiri B, Cox B T and Treeby B E 2020 The effect of curing temperature and time on the acoustic and optical properties of PVCP *IEEE Trans. Ultrason. Ferroelectr. Freq. Control.* **67** 505–12

Baldock C, De Deene Y, Doran S, Ibbott G, Jirasek A, Lepage M, Mcauley K B, Oldham M and Schreiner L J 2010 Polymer gel dosimetry *Phys. Med. Biol.* **55** R1

Battula S, Schoenfeld A, Vrabec G and Njus G O 2006 Experimental evaluation of the holding power/stiffness of the self-tapping bone screws in normal and osteoporotic bone material *Clin. Biomech.* **21** 533–7

Bayraktar H H, Morgan E F, Niebur G L, Morris G E, Wong E K and Keaveny T M 2004 Comparison of the elastic and yield properties of human femoral trabecular and cortical bone tissue *J. Biomech.* **37** 27–35

Beaulieu L, Carlsson Tedgren Å, Carrier J, Davis S D, Mourtada F, Rivard M J, Thomson R M, Verhaegen F, Wareing T A and Williamson J F 2012 Report of the Task Group 186 on model-based dose calculation methods in brachytherapy beyond the TG-43 formalism: current status and recommendations for clinical implementation *Med. Phys.* **39** 6208–36

Beaumont T, Ideias P C, Rimlinger M, Broggio D and Franck D 2017 Development and test of sets of 3D printed age-specific thyroid phantoms for 131I measurements *Phys. Med. Biol.* **62** 4673–93

Berger M J, Hubbell J H, Seltzer S, Chang J, Coursey J S, Sukumar R, Zucker D S and Olsen K 2010 XCOM: photon cross section database (version 1.5) *NIST Stand. Ref. Database* **8** 87–3597

Bernard C P, Liney G P, Manton D J, Turnbull L W and Langton C M 2008 Comparison of fat quantification methods: A phantom study at 3.0T *J. Magn. Reson. Imaging.* **27** 192–7

Bertholet J *et al* 2019 Real-time intrafraction motion monitoring in external beam radiotherapy *Phys. Med. Biol.* **64** 15TR01

Berthon B, Marshall C, Holmes R and Spezi E 2015 A novel phantom technique for evaluating the performance of PET auto-segmentation methods in delineating heterogeneous and irregular lesions *EJNMMI Phys.* **2** 1–17

Besaratinia A and Pfeifer G P 2007 A review of mechanisms of acrylamide carcinogenicity *Carcinogenesis* **28** 519–28

Bliznakova K, Buliev I and Bliznakov Z 2018 *Anthropomorphic Phantoms in Image Quality and Patient Dose Optimization; A EUTEMPE Network Book* ed K Bliznakova, I Buliev and B Zhivko (Bristol, UK: IOP ebooks, IOP Publ.)
Bliznakova K, Dukov N, Feradov F, Gospodinova G, Bliznakov Z, Russo P, Mettivier G, Bosmans H, Cockmartin L and Sarno A 2019 Development of breast lesions models database *Phys. Med.* **64** 293–303
Bohndiek S E 2019 Addressing photoacoustic standards *Nat. Photon.* **13** 298
Boltz T, Pavlicek W, Paden R, Renno M, Jensen A and Akay M 2010 An anthropomorphic beating heart phantom for cardiac X-ray CT imaging evaluation *J. Appl. Clin. Med. Phys.* **11** 191–9
Bottomley P A, Foster T H, Argersinger R E and Pfeifer L M 1984 A review of normal tissue hydrogen NMR relaxation times and relaxation mechanisms from 1–100 MHz: dependence on tissue type, NMR frequency, temperature, species, excision, and age *Med. Phys.* **11** 425–48
Brewin M P, Pike L C, Rowland D E and Birch M J 2008 The acoustic properties, centered on 20 MHZ, of an IEC agar-based tissue-mimicking material and its temperature, frequency and age dependence *Ultrasound Med. Biol.* **34** 1292–306
Brodin N P, Partanen A, Asp P, Branch C A, Guha C and Tomé W A 2016 A simple method for determining the coagulation threshold temperature of transparent tissue-mimicking thermal therapy gel phantoms: validated by magnetic resonance imaging thermometry *Med. Phys.* **43** 1167–74
Brown R H, Wise R A, Kirk G, Drummond M B and Mitzner W 2015 Lung density changes with growth and inflation *Chest* **148** 995–1002
Browne J E, Ramnarine K V, Watson A J and Hoskins P R 2003 Assessment of the acoustic properties of common tissue-mimicking test phantoms *Ultrasound Med. Biol.* **29** 1053–60
Brunon A, Bruyère-Garnier K and Coret M 2010 Mechanical characterization of liver capsule through uniaxial quasi-static tensile tests until failure *J. Biomech.* **43** 2221–7
Budday S *et al* 2017 Mechanical characterization of human brain tissue *Acta Biomater.* **48** 319–40
Burleson S, Baker J, Hsia A T and Xu Z 2015 Use of 3D printers to create a patient-specific 3D bolus for external beam therapy *J. Appl. Clin. Med. Phys.* **16** 166–78
Byng J W, Yaffe M J, Jong R A, Shumak R S, Lockwood G A, Tritchler D L and Boyd N F 1998 Analysis of mammographic density and breast cancer risk from digitized mammograms *Radiographics* **18** 1587–98
Cabrelli L C, Grillo F W, Sampaio D R T, Carneiro A A O and Pavan T Z 2017a Acoustic and elastic properties of glycerol in oil-based gel phantoms *Ultrasound Med. Biol.* **43** 2086–94
Cabrelli L C, Pelissari P I B G B, Deana A M, Carneiro A A O and Pavan T Z 2017b Stable phantom materials for ultrasound and optical imaging *Phys. Med. Biol.* **62** 432–47
Cabrelli L C, Sampaio D R T, Uliana J H, Carneiro A A O, Pavan T Z and De Ana A M 2015 Copolymer-in-oil phantoms for photoacoustic imaging *2015 IEEE Int. Ultrason. Symp. IUS 2015* pp 5–8
Caldwell B, Greenwald D, Moreira D, Tain R W, Coogan C, Xie K, Mar W, Pfanner P and Abern M 2019 Constructing and pilot testing a novel prostate magnetic resonance imaging/ultrasound fusion biopsy phantom *Urology* **124** 33–37
Cannon L M, Fagan A J and Browne J E 2011 Novel tissue mimicking materials for high frequency breast ultrasound phantoms *Ultrasound Med. Biol.* **37** 122–35
Cao R, Huang Z, Nabi G and Melzer A 2019 Patient-specific 3-dimensional model for high-intensity focused ultrasound treatment through the rib cage: a preliminary study *J. Ultrasound Med.*
Cao Y, Li G Y, Zhang X and Liu Y L 2017 Tissue-mimicking materials for elastography phantoms: a review *Extreme Mech. Lett.* **17** 62–70
Ceh J, Youd T, Mastrovich Z, Peterson C, Khan S, Sasser T A, Sander I M, Doney J, Turner C and Leevy W M 2017 Bismuth infusion of ABS enables additive manufacturing of complex radiological phantoms and shielding equipment *Sensors (Switzerland)* **17** 1–11
Cerviño L, Soultan D, Cornell M, Yock A, Pettersson N, Song W Y, Aguilera J, Advani S, Murphy J and Hoh C 2017 A novel 3D-printed phantom insert for 4D PET/CT imaging and simultaneous integrated boost radiotherapy *Med. Phys.* **44** 5467–74
Chakouch M K, Charleux F and Bensamoun S F 2015 Development of a phantom mimicking the functional and structural behaviors of the thigh muscles characterized with magnetic resonance elastography technique *Proc. Annu. Int. Conf. IEEE Eng. Med. Biol. Soc. EMBS* (2015-November) pp 6736–9
Chandramohan D, Cao P, Han M, An H, Sunderland J J, Kinahan P E, Laforest R, Hope T A and Larson P E Z 2020 Bone material analogues for PET/MRI phantoms *Med. Phys.* **47** 2161–70
Chen R and Shih A 2013 Multi-modality gellan gum-based tissue-mimicking phantom with targeted mechanical, electrical, and thermal properties *Phys. Med. Biol.* **58** 5511–25
Cheung Y and Sawant A 2015 An externally and internally deformable, programmable lung motion phantom *Med. Phys.* **42** 2585–93
Cho H M, Ding H, Kumar N, Sennung D and Molloi S 2017 Calibration phantoms for accurate water and lipid density quantification using dual energy mammography *Phys. Med. Biol.* **62** 4589–603
Choi E, Adams F, Palagi S, Gengenbacher A, Schlager D, Müller P F, Gratzke C, Miernik A, Fischer P and Qiu T 2020 A high-fidelity phantom for the simulation and quantitative evaluation of transurethral resection of the prostate *Ann. Biomed. Eng.* **48** 437–46
Choi M J, Guntur S R, Lee K I L, Paeng D G and Coleman A 2013 A tissue mimicking polyacrylamide hydrogel phantom for visualizing thermal lesions generated by high intensity focused ultrasound *Ultrasound Med. Biol.* **39** 439–48
Chong A C M, Friis E A, Ballard G P, Czuwala P J and Cooke F W 2007a Fatigue performance of composite analogue femur constructs under high activity loading *Ann. Biomed. Eng.* **35** 1196–205
Chong A C M, Miller F, Buxton M and Friis E A 2007b Fracture toughness and fatigue crack propagation rate of short fiber reinforced epoxy composites for analogue cortical bone *J. Biomech. Eng.* **129** 487–93
Clark C H, Aird E G A, Bolton S, Miles E A, Nisbet A, Snaith J A D, Thomas R A S, Venables K and Thwaites D I 2015 Radiotherapy dosimetry audit: three decades of improving standards and accuracy in UK clinical practice and trials *Br. J. Radiol.* **88** 20150251
Cloonan A J, Shahmirzadi D, Li R X, Doyle B J, Konofagou E E and Mcgloughlin T M 2014 3D-printed tissue-mimicking phantoms for medical imaging and computational validation applications *3D Print. Addit. Manuf.* **1** 14–23
Cockmartin L, Bosmans H and Marshall N W 2013 Comparative power law analysis of structured breast phantom and patient images in digital mammography and breast tomosynthesis *Med. Phys.* **40** 081920
Cockmartin L *et al* 2017 Design and application of a structured phantom for detection performance comparison between breast tomosynthesis and digital mammography *Phys. Med. Biol.* **62** 758–80
Colvill E *et al* 2020 Anthropomorphic phantom for deformable lung and liver CT and MR imaging for radiotherapy *Phys. Med. Biol.* **65** 07NT02

Costa R M, Alvarenga A V, Costa-Felix R P B, Omena T P, von Krüger M A and Pereira W C A 2016 Thermochromic phantom and measurement protocol for qualitative analysis of ultrasound physiotherapy systems *Ultrasound Med. Biol.* **42** 299–307
Coulaud J, Brumas V, Fiallo M *et al* 2018 Tissue-inspired phantoms: a new range of equivalent tissue simulating breast, cortical bone and lung tissue *Biomed. Phys. Eng. Express* **4** 2–7
Cournane S, Cannon L, Browne J E and Fagan A J 2010 Assessment of the accuracy of an ultrasound elastography liver scanning system using a PVA- cryogel phantom with optimal acoustic and mechanical properties *Phys. Med. Biol.* **55** 595–5983
Cournane S, Fagan A J and Browne J E 2011 Review of ultrasound elastography quality control and training test phantoms *Ultrasound* **20** 16–23
Craft D F and Howell R M 2017 Preparation and fabrication of a full-scale, sagittal-sliced, 3D-printed, patient-specific radiotherapy phantom *J. Appl. Clin. Med. Phys.* **18** 285–92
Craft D F, Kry S F, Balter P, Salehpour M, Woodward W and Howell R M 2018 Material matters: analysis of density uncertainty in 3D printing and its consequences for radiation oncology *Med. Phys.* **45** 1614–21
Cubukcu S and Yücel H 2016 Characterization of paraffin based breast tissue equivalent phantom using a CdTe detector pulse height analysis *Australas. Phys. Eng. Sci. Med.* **39** 877–84
Culjat M O, Goldenberg D, Tewari P and Singh R S 2010 A review of tissue substitutes for ultrasound imaging *Ultrasound Med. Biol.* **36** 861–73
Cunningham J M, Barberi E A, Miller J, Kim J P and Glide-Hurst C K 2019 Development and evaluation of a novel MR-compatible pelvic end-to-end phantom *J. Appl. Clin. Med. Phys.* **20** 265–75
Dabbagh A, Abdullah B J J, Abu Kasim N H and Ramasindarum C 2014a Reusable heat-sensitive phantom for precise estimation of thermal profile in hyperthermia application *Int. J. Hyperth.* **30** 66–74
Dabbagh A, Abdullah B J J, Ramasindarum C and Abu Kasim N H 2014b Tissue-mimicking gel phantoms for thermal therapy studies *Ultrason. Imaging* **36** 291–316
Dahal E, Badal A, Zidan A, Alayoubi A, Hagio T, Glick S, Badano A and Ghammraoui B 2018 Stable gelatin-based phantom materials with tunable x-ray attenuation properties and 3D printability for x-ray imaging *Phys. Med. Biol.* **63** 09NT01
Dancewicz O L, Sylvander S R, Markwell T S, Crowe S B and Trapp J V 2017 Radiological properties of 3D printed materials in kilovoltage and megavoltage photon beams *Phys. Med.* **38** 111–8
De Bazelaire C M J, Duhamel G D, Rofsky N M and Alsop D C 2004 MR imaging relaxation times of abdominal and pelvic tissues measured in vivo at 3.0 T: preliminary results *Radiology* **230** 652–9
De Carvalho I M, De Matheo L L, Costa Júnior J F S, Borba C D M, Von Krüger M A, Infantosi A F C and Pereira W C D A 2016 Polyvinyl chloride plastisol breast phantoms for ultrasound imaging *Ultrasonics* **70** 98–106
de Dreuille O, Strijckmans V, Ameida P, Loc'h C and Bendriem B 1997 Bone equivalent liquid solution to assess accuracy of transmission measurements in SPECT and PET *IEEE Trans. Nucl. Sci.* **44** 1186–90
de Jong T L, Pluymen L H, van Gerwen D J, Kleinrensink G J, Dankelman J and van den Dobbelsteen J J 2017 PVA matches human liver in needle-tissue interaction *J. Mech. Behav. Biomed. Mater.* **69** 223–8
De Matheo L L, Geremia J, Calas M J G, Costa-Júnior J F S, da Silva F F F, Krüger M A and de Albuquerque Pereira W C 2018 PVCP-based anthropomorphic breast phantoms containing structures similar to lactiferous ducts for ultrasound imaging: a comparison with human breasts *Ultrasonics* **90** 144–52
de Merxem A G, Lechien V, Thibault T, Dasnoy D and Macq B 2017 Design and implementation of a MRI compatible and dynamic phantom simulating the motion of a tumor in the liver under the breathing cycle *Proc. SPIE 10572, 13th International Conference on Medical Information Processing and Analysis* (17 November 2017) p 105720X
Diamantopoulos S, Platoni K, Patatoukas G, Karaiskos P, Kouloulias V and Efstathopoulos E 2019 Treatment plan verification: A review on the comparison of dose distributions *Phys. Med.* **67** 107–15
Díez P, Aird E G A, Sander T, Gouldstone C A, Sharpe P H G, Lee C D, Lowe G, Thomas R A S, Simnor T and Bownes P 2017 A multicentre audit of HDR/PDR brachytherapy absolute dosimetry in association with the INTERLACE trial (NCT015662405) *Phys. Med. Biol.* **62** 8832
Dong E, Zhao Z, Wang M, Xie Y, Li S, Shao P, Cheng L and Xu R X 2015 Three-dimensional fuse deposition modeling of tissue-simulating phantom for biomedical optical imaging *J. Biomed. Opt.* **20** 1213.11
Dong J, Zhang Y and Lee W-N 2020 Walled vessel-mimicking phantom for ultrasound imaging using 3D printing with a water-soluble filament: design principle, fluid-structure interaction (FSI) simulation, and experimental validation *Phys. Med. Biol.* **65** 85006
Dowling J A, Lambert J, Parker J, Salvado O, Fripp J, Capp A, Wratten C, Denham J W and Greer P B 2012 An atlas-based electron density mapping method for magnetic resonance imaging (MRI)-alone treatment planning and adaptive MRI-based prostate radiation therapy *Int. J. Radiat. Oncol. Biol. Phys.* **83** e5–11
Doyle A J, King D M and Browne J E 2017 A review of the recommendations governing quality assurance of ultrasound systems used for guidance in prostate brachytherapy *Phys. Med.* **44** 51–57
Du Y, Wang R, Wang M, Yue H, Zhang Y, Wu H and Wang W 2019 Radiological tissue equivalence of deformable silicone-based chemical radiation dosimeters (FlexyDos3D) *J. Appl. Clin. Med. Phys.* **20** 87–99
Dunmire B, Kucewicz J C, Mitchell S B, Crum L A and Sekins K M 2013 Characterizing an agar/gelatin phantom for image guided dosing and feedback control of high-intensity focused ultrasound *Ultrasound Med. Biol.* **39** 300–11
Durando G, Miloro P, Wilkens V, Karaboce B, de Pooter J, van Rhoon G, Ter Haar G, Caccia B, Spinelli A and Denkova A 2019 RaCHy-radiotherapy coupled with hyperthermia-18HLT06 EURAMET EMPIR Project *2019 IEEE Int. Symp. on Medical Measurements and Applications (MeMeA)* (IEEE) pp 1–5
Ehn S *et al* 2018 Assessment of quantification accuracy and image quality of a full-body dual-layer spectral CT system *J. Appl. Clin. Med. Phys.* **19** 204–17
Ehrbar S *et al* 2019 ELPHA: dynamically deformable liver phantom for real-time motion-adaptive radiotherapy treatments *Med. Phys.* **46** 839–50
El-Brawany M A, Nassiri D K, Terhaar G, Shaw A, Rivens I and Lozhken K 2009 Measurement of thermal and ultrasonic properties of some biological tissues *J. Med. Eng. Technol.* **33** 249–56
Eranki A, Mikhail A S, Negussie A H, Katti P S, Wood B J and Partanen A 2019 Tissue-mimicking thermochromic phantom for characterization of HIFU devices and applications *Int. J. Hyperth.* **36** 518–29
Eriksson R, Persson H W, Dymling S O and Lindström K 1995 A microcirculation phantom for performance testing of blood perfusion measurement equipment *Eur. J. Ultrasound* **2** 65–75
Esposito G *et al* 2019 Investigation of the refractive index decrement of 3D printing materials for manufacturing breast phantoms for phase contrast imaging *Phys. Med. Biol.* **64** 075008

Farrer A I, Odéen H, de Bever J, Coats B, Parker D L, Payne A and Christensen D A 2015 Characterization and evaluation of tissue-mimicking gelatin phantoms for use with MRgFUS *J. Ther. Ultrasound* **3** 1–11
Fiaschetti G, Browne J E, Cavagnaro M, Farina L and Ruvio G 2018 Tissue mimicking materials for multi-modality breast phantoms *2018: 2nd URSI Atl. Radio Sci. Meet. AT-RASC 2018* pp 1–6
Filippou V and Tsoumpas C 2018 Recent advances on the development of phantoms using 3D printing for imaging with CT, MRI, PET, SPECT, and ultrasound *Med. Phys.* **45** e740–60
Fitzgerald P F, Colborn R E, Edic P M, Lambert J W, Bonitatibus P J and Yeh B M 2017 Liquid tissue surrogates for X-ray and CT phantom studies *Med. Phys.* **44** 6251–60
Fonseca M, Zeqiri B, Beard P and Cox B 2015 Characterisation of a PVCP-based tissue-mimicking phantom for quantitative photoacoustic imaging *Proc. SPIE* **9539** 953911
Fonseca M, Zeqiri B, Beard P C and Cox B T 2016 Characterisation of a phantom for multiwavelength quantitative photoacoustic imaging *Phys. Med. Biol.* **61** 4950–73
Forte A E, D'Amico F, Charalambides M N, Dini D and Williams J G 2015 Modelling and experimental characterisation of the rate dependent fracture properties of gelatine gels *Food Hydrocoll.* **46** 180–90
Forte A E, Galvan S and Dini D 2018 Models and tissue mimics for brain shift simulations *Biomech. Model. Mechanobiol.* **17** 249–61
Forte A E, Galvan S, Manieri F, Rodriguez y Baena F and Dini D 2016 A composite hydrogel for brain tissue phantoms *Mater. Des.* **112** 227–38
Fredenberg E, Kilburn-Toppin F, Willsher P, Moa E, Danielsson M, Dance D R, Young K C and Wallis M G 2016 Measurement of breast-tissue x-ray attenuation by spectral mammography: solid lesions *Phys. Med. Biol.* **61** 2595
Fromageau J, Brusseau E, Vray D, Gimenez G and Delachartre P 2003 Characterization of PVA cryogel for intravascular ultrasound elasticity imaging *IEEE Trans. Ultrason. Ferroelectr. Freq. Control.* **50** 1318–24
Fuerst D, Stephan D, Augat P and Schrempf A 2012. Foam phantom development for artificial vertebrae used for surgical training *Annual Int. Conf. of the IEEE Engineering in Medicine and Biology* Society, *EMBS* (IEEE) pp 5773–6
Fukushima Y and Naemura K 2014 Estimation of the friction force during the needle insertion using the disturbance observer and the recursive least square *Robomech. J.* **1** 1–8
Funama Y, Utsunomiya D, Oda S, Shimonobo T, Nakaura T, Mukunoki T, Kidoh M, Yuki H and Yamashita Y 2016 Transluminal attenuation-gradient coronary CT angiography on a 320-MDCT volume scanner: effect of scan timing, coronary artery stenosis, and cardiac output using a contrast medium flow phantom *Phys. Med.* **32** 1415–21
Gallas R R, Hünemohr N, Runz A, Niebuhr N I, Jäkel O and Greilich S 2015 An anthropomorphic multimodality (CT/MRI) head phantom prototype for end-to-end tests in ion radiotherapy *Z. Med. Phys.* **25** 391–9
Gatto M, Memoli G, Shaw A, Sadhoo N, Gelat P and Harris R A 2012 Three-dimensional printing (3DP) of neonatal head phantom for ultrasound: thermocouple embedding and simulation of bone *Med. Eng. Phys.* **34** 929–37
Gear J I, Cummings C, Craig A J, Divoli A, Long C D C, Tapner M and Flux G D 2016 Abdo-Man: a 3D-printed anthropomorphic phantom for validating quantitative SIRT *EJNMMI Phys.* **3** 17
Geoghegan R, Santamaria A, Priester A, Zhang L, Wu H, Grundfest W, Marks L and Natarajan S 2019 A tissue-mimicking prostate phantom for 980 nm laser interstitial thermal therapy *Int. J. Hyperth.* **36** 993–1002
Gholampourkashi S, Cygler J E, Lavigne B and Heath E 2018 Development of a deformable phantom for experimental verification of 4D Monte Carlo simulations in a deforming anatomy *Phys. Med.* **51** 81–90
Giering K, Minet O, Lamprecht I and Muller G 1995 Review of thermal properties of biological tissues *SPIE Opt. Eng. Press.* **044** 45–65
Giesen E B W, Ding M, Dalstra M and Van Eijden T M G J 2001 Mechanical properties of cancellous bone in the human mandibular condyle are anisotropic *J. Biomech.* **34** 799–803
Glick S J and Ikejimba L C 2018 Advances in digital and physical anthropomorphic breast phantoms for x-ray imaging *Med. Phys.* **45** e870–85
Gold G E, Han E, Stainsby J, Wright G, Brittain J and Beaulieu C 2004 Musculoskeletal MRI at 3.0 T: relaxation times and image contrast *Am. J. Roentgenol.* **183** 343–51
Gorjiara T, Hill R, Kim J-H, Kuncic Z, Adamovics J and Baldock C 2010 Study of dosimetric water equivalency of PRESAGE® for megavoltage and kilovoltage x-ray beams *J. Phys. Conf. Ser.* **250** 12053
Grillo F, Cabrelli L, Sampaio D, Carneiro A and Pavan T 2017 Glycerol in oil-based phantom with improved performance for photoacoustic imaging *IEEE Int. Ultrason. Symp. IUS* pp 1–4
Große Hokamp N, Abdullayev N, Persigehl T, Schlaak M, Wybranski C, Holz J A, Streichert T, Alkadhi H, Maintz D and Haneder S 2019 Precision and reliability of liver iodine quantification from spectral detector CT: evidence from phantom and patient data *Eur. Radiol.* **29** 2098–106
Guntur S R, Lee K I, Paeng D-G, Coleman A J and Choi M J 2013 Temperature-dependent thermal properties of *ex vivo* liver undergoing thermal ablation *Ultrasound Med. Biol.* **39** 1771–84
Guo S, Mansour R and Henderson Slater D 2019 Ultrasound-guided continuous radiofrequency ablation of painful residual limb neuroma in individuals with limb amputation– A retrospective case series. *Can. Prosthet. Orthot. J* **2** 4
Hamedani B A, Melvin A, Vaheesan K, Gadani S, Pereira K and Hall A F 2018 Three-dimensional printing CT-derived objects with controllable radiopacity *J. Appl. Clin. Med. Phys.* **19** 317–28
Hammerstein G R, Miller D W, White D R, Masterson M E, Woodard H Q and Laughlin J S 1979 Absorbed radiation dose in mammography *Radiology* **130** 485–91
Han A, Andre M P, Deiranieh L, Housman E, Erdman J W Jr , Loomba R, Sirlin C B and O'Brien W D Jr 2018 Repeatability and reproducibility of the ultrasonic attenuation coefficient and backscatter coefficient measured in the right lobe of the liver in adults with known or suspected nonalcoholic fatty liver disease *J. Ultrasound Med.* **37** 1913–27
Hanks B, Azhar F, Frecker M, Clement R, Greaser J and Snook K 2019 A deployable multi-tine endoscopic radiofrequency ablation electrode: simulation validation in a thermochromic tissue phantom *Front. Biomed. Devices, BIOMED - 2019 Des. Med. Devices Conf. DMD 2019* pp 16–18
Hasgall P, Di Gennaro F, Baumgartner C, Neufeld E, Lloyd B, Gosselin M, Payne D, Klingenböck A and Kuster N 2018 IT'IS Database for thermal and electromagnetic parameters of biological tissues Version 4
Hazelaar C, Van Eijnatten M, Dahele M, Wolff J, Forouzanfar T, Slotman B and Verbakel W F A R 2018 Using 3D printing techniques to create an anthropomorphic thorax phantom for medical imaging purposes *Med. Phys.* **45** 92–100
He Y *et al* 2019a 3D-printed breast phantom for multi-purpose and multi-modality imaging *Quant. Imaging Med. Surg.* **9** 63–74
He Y *et al* 2019b Characterizing mechanical and medical imaging properties of polyvinyl chloride-based tissue-mimicking material *J. Appl. Clin. Med. Phys.* **20** 176–83

Heiner A D 2008 Structural properties of fourth-generation composite femurs and tibias *J. Biomech.* **41** 3282–4
Hellerbach A, Schuster V, Jansen A and Sommer J 2013 MRI phantoms – are there alternatives to agar? *PloS One* **8** e70343
Hernandez-Giron I, den Harder J M, Streekstra G J, Geleijns J and Veldkamp W J H 2019 Development of a 3D printed anthropomorphic lung phantom for image quality assessment in CT *Phys. Med.* **57** 47–57
Hill R, Kuncic Z and Baldock C 2010 The water equivalence of solid phantoms for low energy photon beams *Med. Phys.* **37** 4355–63
Hoffman E J, Cutler P D, Guerrero T M, Digby W M and Mazziotta J C 1991 Assessment of accuracy of PET utilizing a 3-D phantom to simulate the activity distribution of [18F]fluorodeoxyglucose uptake in the human brain *J. Cereb. Blood Flow Metab.* **11** A17–A25
Hofstetter L W, Fausett L, Mueller A, Odéen H, Payne A, Christensen D A and Parker D L 2020 Development and characterization of a tissue mimicking psyllium husk gelatin phantom for ultrasound and magnetic resonance imaging *Int. J. Hyperth.* **37** 283–90
Hollensteiner M, Augat P, Fürst D, Schrödl F, Esterer B, Gabauer S and Schrempf A 2019 Bone surrogates provide authentic onlay graft fixation torques *J. Mech. Behav. Biomed. Mater.* **91** 159–63
Hollensteiner M, Fuerst D and Schrempf A 2014 Artificial muscles for a novel simulator in minimally invasive spine surgery *36th Annual Int. Conf. of the IEEE Engineering in Medicine and Biology Society, EMBC 2014* (IEEE) pp 506–9
Hollensteiner M, Fürst D, Esterer B, Augat P, Schrödl F, Hunger S, Malek M, Stephan D and Schrempf A 2017 Novel bone surrogates for cranial surgery training *J. Mech. Behav. Biomed. Mater.* **72** 49–51
Hollensteiner M, Malek M, Augat P, Fürst D, Schrödl F, Hunger S, Esterer B, Gabauer S and Schrempf A 2018 Validation of a simulator for cranial graft lift training: face, content, and construct validity *J. Cranio-Maxillofacial Surg.* **46** 1390–4
Hollensteiner M, Samrykit M, Hess M, Fuerst D and Schrempf A 2015 Development of trabecular bone surrogates for kyphoplasty-balloon dilatation training *Annual Int. Conf. of the IEEE Engineering in Medicine and Biology* Society, *EMBS* vol 2015 *Novem* (IEEE) pp 5106–9
Holzapfel G A, Sommer G and Regitnig P 2004 Anisotropic mechanical properties of tissue components in human atherosclerotic plaques *J. Biomech. Eng.* **126** 657–65
Hong D, Lee S, Kim G B, Lee S M, Kim N and Seo J B 2020 Development of a CT imaging phantom of anthromorphic lung using fused deposition modeling 3D printing *Med. (United States)* **99** e18617
Huamani T Y, Mullisaca P A, Apaza V G, Chen F and Vega R J 2019 Construction and characterization of materials equivalent to the tissues and organs of the human body for radiotherapy *Radiat. Phys. Chem.* **159** 70–75
Hubbell J H and Seltzer S M 2004 Tables of X-Ray mass attenuation coefficients and mass energy-absorption coefficients (version 1.4) National Institute of Standards and Technology, Gaithersburg. Orig. Publ. as NISTIR vol 5632 available: http://physics.nist.gov/xaamdi
Hungr N, Long J-A-A, Beix V and Troccaz J 2012 A realistic deformable prostate phantom for multimodal imaging and needle-insertion procedures *Med. Phys.* **39** 2031–41
Hwang Y S, Cheung Y C, Lin Y Y, Hsu H L and Tsai H Y 2018 Susceptibility of iodine concentration map of dual-energy contrast-enhanced digital mammography for quantitative and tumor enhancement assessment *Acta Radiol.* **59** 893–901
Ibelli T, Templeton S and Levi-Polyachenko N 2018 Progress on utilizing hyperthermia for mitigating bacterial infections *Int. J. Hyperth.* **34** 144–56
ICRU 1998 Report 61 Tissue substitutes, phantoms and computational modelling in medical ultrasound *Int. Comm. Radiat. Units Meas.*, (Bethseda, MD)
IEC 2007 IEC 60601-2-37:2007 Particular requirements for the basic safety and essential performance of ultrasonic medical diagnostic and monitoring equipment
Iivarinen J T, Korhonen R K and Jurvelin J S 2014 Experimental and numerical analysis of soft tissue stiffness measurement using manual indentation device - significance of indentation geometry and soft tissue thickness *Ski. Res. Technol.* **20** 347–54
Ikejimba L C, Glick S J, Choudhury K R, Samei E and Lo J Y 2016 Assessing task performance in FFDM, DBT, and synthetic mammography using uniform and anthropomorphic physical phantoms *Med. Phys.* **43** 5593–602
Ikejimba L C, Graff C G, Rosenthal S, Badal A, Ghammraoui B, Lo J Y and Glick S J 2017 A novel physical anthropomorphic breast phantom for 2D and 3D x-ray imaging *Med. Phys.* **44** 407–16
Ikejimba L C, Salad J, Graff C G, Ghammraoui B, Cheng W C, Lo J Y and Glick S J 2019 A four-alternative forced choice (4AFC) methodology for evaluating microcalcification detection in clinical full-field digital mammography (FFDM) and digital breast tomosynthesis (DBT) systems using an inkjet-printed anthropomorphic phantom *Med. Phys.* **46** 3883–92
In E, Walker E and Naguib H E 2017 Novel development of 3D printable UV-curable silicone for multimodal imaging phantom *Bioprinting* **7** 19–26
Inglis S, Ramnarine K V, Plevris J N and Mcdicken W N 2006 An anthropomorphic tissue-mimicking phantom of the oesophagus for endoscopic ultrasound *Ultrasound Med. Biol.* **32** 249–59
Ivanov D *et al* 2018 Suitability of low density materials for 3D printing of physical breast phantoms *Phys. Med. Biol.* **63** 175020
Ivory A 2018 Development of an optimised subharmonic dynamic contrast-enhanced ultrasound imaging technique for liver cancer www.tara.tcd.ie/handle/2262/83757
Ivory A M, Shah A, Rajagopal S and Zeqiri B 2019 Development and investigation of the acoustic properties of tissue-mimicking materials for photoacoustic imaging techniques *IEEE Trans. Ultrason. Ferroelectr. Freq. Control* pp 1489–92
Jahnke P, Limberg F R P, Gerbl A, Ardilla Pardo G L, Braun V P B, Hamm B and Scheel M 2016 Realistic CT Phantoms 1 *Radiology* **282** 569–75
Jaszczak R J, Murphy P H, Huard D and Burdine J A 1977 Radionuclide emission computed tomography of the head with 99mCc and a scintillation camera *J. Nucl. Med.* **18** 373–80
Jiang S, Liu S and Feng W 2011 PVA hydrogel properties for biomedical application *J. Mech. Behav. Biomed. Mater.* **4** 1228–33
Jiang S, Su Z, Wang X, Liu S and Yu Y 2013 Development of a new tissue-equivalent material applied to optimizing surgical accuracy *Mater. Sci. Eng.* C **33** 3768–74
Jin L, Sun Y and Li M 2019 Use of an anthropomorphic chest model to evaluate multiple scanning protocols for high- definition and standard-definition computed tomography to detect small pulmonary nodules *Med. Sci. Monit.* **25** 2195–205
Johansson A, Karlsson M and Nyholm T 2011 CT substitute derived from MRI sequences with ultrashort echo time *Med. Phys.* **38** 2708–14
Johns P C and Yaffe M J 1987 X-ray characterisation of normal and neoplastic breast tissues *Phys. Med. Biol.* **32** 675
Kadoya N *et al* 2017 Evaluation of deformable image registration between external beam radiotherapy and HDR brachytherapy for cervical cancer with a 3D-printed deformable pelvis phantom: *Med. Phys.* **44** 1445–55
Kalender W 1981 Monte Carlo calculations of x-ray scatter data for diagnostic radiology *Phys. Med. Biol.* **26** 835
Kalendralis P *et al* 2019 Multicenter CT phantoms public dataset for radiomics reproducibility tests *Med. Phys.* **46** 1512–8

Kamomae T et al 2017 Three-dimensional printer-generated patient-specific phantom for artificial in vivo dosimetry in radiotherapy quality assurance Phys. Med. 44 205–11
Kamphuis M E, Greuter M J W, Slart R H J A and Slump C H 2020 Quantitative imaging: systematic review of perfusion/flow phantoms Eur. Radiol. Exp. 4 15
Kemerink G J, Visser M G W, Franssen R, Beijer E, Zamburlini M, Halders S G E A, Brans B, Mottaghy F M and Teule G J J 2011 Effect of the positron range of 18 F, 68 Ga and 124 I on PET/CT in lung-equivalent materials Eur. J. Nucl. Med. Mol. Imaging 38 940–8
Kenwright D A, Laverick N, Anderson T, Moran C M and Hoskins P R 2015 Wall-less flow phantom for high-frequency ultrasound applications Ultrasound Med. Biol. 41 890–7
Kiarashi N, Nolte A C, Sturgeon G M, Segars W P, Ghate S V, Nolte L W, Samei E and Lo J Y 2015 Development of realistic physical breast phantoms matched to virtual breast phantoms based on human subject data Med. Phys. 42 4116–26
Kim D-H, Cho S, Jo K, Shin E, Hong C-S, Han Y, Suh T-S, Lim D H and Choi D H 2018a Proton range verification in inhomogeneous tissue: treatment planning system vs. measurement vs. Monte Carlo simulation PloS One 13 e0193904
Kim M J, Lee S R, Lee M Y, Sohn J W, Yun H G, Choi J Y, Jeon S W and Suh T S 2017 Characterization of 3D printing techniques: toward patient specific quality assurance spine-shaped phantom for stereotactic body radiation therapy PloS One 12 e0176227
Kim Y T, Ma D, Sim J K and Kim S H 2018b Simultaneous evaluation of thermal and non-thermal effects of high-intensity focused ultrasound on a tissue-mimicking phantom Ultrasound Med. Biol. 44 1799–809
King R L, Liu Y, Maruvada S, Herman B A, Wear K A and Harris G R 2011 Development and characterization of a tissue-mimicking material for high-intensity focused ultrasound IEEE Trans. Ultrason. Ferroelectr. Freq. Control. 58 1397–405
Kobe A, Zadory M, Hamie Q M, Froehlich J M, Klarhöfer M, Elsässer T, Pfammatter T and Guggenberger R 2019 Development of an anthropomorphic spine phantom suitable for fusion of MR neurography with interventional flat-panel CT Eur. J. Radiol. 112 153–60
Konstas A A, Goldmakher G V, Lee T Y and Lev M H 2009 Theoretic basis and technical implementations of CT perfusion in acute ischemic stroke, Part 2: technical implementations Am. J. Neuroradiol. 30 885–92
Kostiukhina N et al 2017 Advanced Radiation DOSimetry phantom (ARDOS): A versatile breathing phantom for 4D radiation therapy and medical imaging Phys. Med. Biol. 62 8136–53
Kot B C W, Zhang Z J, Lee A W C, Leung V Y F and Fu S N 2012 Elastic modulus of muscle and tendon with shear wave ultrasound elastography: variations with different technical settings PloS One 7 2–7
Kron T, Lehmann J and Greer P B 2016 Dosimetry of ionising radiation in modern radiation oncology Phys. Med. Biol. 61 R167–205
Kumar A and Han S S 2017 PVA-based hydrogels for tissue engineering: a review Int. J. Polym. Mater. Polym. Biomater. 66 159–82
Lambrecht M L, Eaton D J, Sonke -J-J, Nestle U, Peulen H, Weber D C, Verheij M and Hurkmans C W 2019 Results of a multicentre dosimetry audit using a respiratory phantom within the EORTC LungTech trial Radiother. Oncol. 138 106–13
Lavarello R J, Ghoshal G and Oelze M L 2011 On the estimation of backscatter coefficients using single-element focused transducers J. Acoust. Soc. Am. 129 2903–11
Lehmann J et al 2018 Dosimetric end-to-end tests in a national audit of 3D conformal radiotherapy Phys. Imaging Radiat. Oncol. 6 5–11
Leibinger A, Forte A E, Tan Z, Oldfield M J, Beyrau F, Dini D and Rodriguez y Baena F 2016 Soft tissue phantoms for realistic needle insertion: a comparative study Ann. Biomed. Eng. 44 2442–52
Li A D-R, Plott J, Chen L, Montgomery J S and Shih A 2020 Needle deflection and tissue sampling length in needle biopsy J. Mech. Behav. Biomed. Mater. 104 103632
Li P, Jiang S, Yu Y, Yang J and Yang Z 2015a Biomaterial characteristics and application of silicone rubber and PVA hydrogels mimicked in organ groups for prostate brachytherapy J. Mech. Behav. Biomed. Mater. 49 220–34
Li P, Yang Z and Jiang S 2018 Tissue mimicking materials in image-guided needle-based interventions: a review Mater. Sci. Eng. C 93 1116–31
Li W, Belmont B, Greve J M, Manders A B, Downey B C, Zhang X, Xu Z, Guo D and Shih A 2016 Polyvinyl chloride as a multimodal tissue-mimicking material with tuned mechanical and medical imaging properties Med. Phys. 43 5577–92
Li W, Belmont B and Shih A 2015b Design and manufacture of polyvinyl chloride (PVC) tissue mimicking material for needle insertion Procedia Manuf. 1 866–78
Liao Y et al 2017 An anthropomorphic abdominal phantom for deformable image registration accuracy validation in adaptive radiation therapy Med. Phys. 44 2369–78
Lindner U, Lawrentschuk N, Weersink R A, Raz O, Hlasny E, Sussman M S, Davidson S R, Gertner M R and Trachtenberg J 2010 Construction and evaluation of an anatomically correct multi-image modality compatible phantom for prostate cancer focal ablation J. Urol. 184 352–7
Liney G P, Tozer D J and Turnbull L W 1999 A simple and realistic tissue-equivalent breast phantom for MRI J. Magn. Reson. Imaging 10 968–71
Lourenço A et al 2017 Evaluation of the water-equivalence of plastic materials in low- and high-energy clinical proton beams Phys. Med. Biol. 62 3883–901
Lourenço A, Wellock N, Thomas R, Homer M, Bouchard H, Kanai T, Macdougall N, Royle G and Palmans H 2016 Theoretical and experimental characterization of novel water-equivalent plastics in clinical high-energy carbon-ion beams Phys. Med. Biol. 61 7623–38
Lyu J J, Wu X, Liu Y, Liu Y, Li A D, Zheng Y and Shih A J 2019 A miniature nickel-diamond electroplated wheel for grinding of the arterial calcified plaque 47th SME North American Manufacturing Research Conf. (Erie, PA) (https://doi.org/10.1016/j.promfg.2019.06.142)
Macavelia T, Salahi M, Olsen M, Crookshank M, Schemitsch E H, Ghasempoor A, Janabi-Sharifi F and Zdero R 2012 Biomechanical measurements of surgical drilling force and torque in human versus artificial femurs J. Biomech. Eng. 134 1–9
Macq B M, Geelhand de Merxem A, Lechien V, Thibault T and Dasnoy D 2017 Design and implementation of a MRI compatible and dynamic phantom simulating the motion of a tumor in the liver under the breathing cycle Proc. SPIE 10572 105720X
Madamesila J, Mcgeachy P, Villarreal Barajas J E and Khan R 2016 Characterizing 3D printing in the fabrication of variable density phantoms for quality assurance of radiotherapy Phys. Med. 32 242–7
Madsen E L et al 1999 Interlaboratory comparison of ultrasonic backscatter, attenuation, and speed measurements J. Ultrasound Med. 18 615–31
Madsen E L, Frank G R, Krouskop T A, Varghese T, Kallel F and Ophir J 2003 Tissue-mimicking oil-in-gelatin dispersions for use in heterogeneous elastography phantoms Ultrason. Imaging 25 17–38
Madsen E L, Hobson M A, Frank G R, Shi H, Jiang J, Hall T J, Varghese T, Doyley M M and Weaver J B 2006 Anthropomorphic breast phantoms for testing elastography systems Ultrasound Med. Biol. 32 857–74

Mainprize J, Carton A-K, Klausz R, Li Z, Muller S L, Hunter D M, Yaffe M J and Mawdsley G E 2018 Development of a physical 3D anthropomorphic breast texture model using selective laser sintering rapid prototype printing *Proc. SPIE* **10573** 105730A
Makris D N, Pappas E P, Zoros E, Papanikolaou N, Saenz D L, Kalaitzakis G, Zourari K, Efstathopoulos E, Maris T G and Pappas E 2019 Characterization of a novel 3D printed patient specific phantom for quality assurance in cranial stereotactic radiosurgery applications *Phys. Med. Biol.* **64** 105009
Malone A J, Cournane S, Naydenova I G, Fagan A J and Browne J E 2020 Polyvinyl alcohol cryogel based vessel mimicking material for modelling the progression of atherosclerosis *Phys. Med.* **69** 1–8
Maneas E *et al* 2018a Anatomically realistic ultrasound phantoms using gel wax with 3D printed moulds *Phys. Med. Biol.* **63** aa9e2c
Maneas E *et al* 2018b Gel wax-based tissue-mimicking phantoms for multispectral photoacoustic imaging *Biomed. Opt. Express* **9** 1151
Mann P, Witte M, Moser T, Lang C, Runz A, Johnen W, Berger M, Biederer J and Karger C P 2017 3D dosimetric validation of motion compensation concepts in radiotherapy using an anthropomorphic dynamic lung phantom *Phys. Med. Biol.* **62** 573–95
Marrouche N F, Brachmann J, Andresen D, Siebels J, Boersma L, Jordaens L, Merkely B, Pokushalov E, Sanders P and Proff J 2018 Catheter ablation for atrial fibrillation with heart failure *New Engl. J. Med.* **378** 417–27
Maruyama S, Ueda J, Kimura A and Murase K 2016 Development and characterization of novel LipoCEST agents based on thermosensitive liposomes *Magn. Reson. Med. Sci.* **15** 324–34
Mast T D 2000 Empirical relationships between acoustic parameters in human soft tissues *Acoust. Res. Lett.* **1** 37–42
Mcrobbie D W, Moore E A, Graves M J and Prince M R 2006 *MRI from Picture to Proton* (Cambridge: Cambridge University Press) (https://doi.org/10.1017/CBO9780511545405)
Melnyk R, Ezzat B, Belfast E, Saba P, Farooq S, Campbell T, Mcaleavey S, Buckley M and Ghazi A 2019 Mechanical and functional validation of a perfused, robot-assisted partial nephrectomy simulation platform using a combination of 3D printing and hydrogel casting *World J. Urol.* **38** 1631–41
Menikou G, Dadakova T, Pavlina M, Bock M and Damianou C 2015 MRI compatible head phantom for ultrasound surgery *Ultrasonics* **57** 144–52
Menikou G and Damianou C 2017 Acoustic and thermal characterization of agar based phantoms used for evaluating focused ultrasound exposures *J. Ther. Ultrasound* **5** 14
Menikou G, Yiannakou M, Yiallouras C, Ioannides C and Damianou C 2016 *MRI-compatible Bone Phantom for Evaluating Ultrasonic Thermal Exposures Ultrasonics* **71** 12–19
Mikayama R, Yabuuchi H, Matsumoto R, Kobayashi K, Yamashita Y, Kimura M, Kamitani T, Sagiyama K and Yamasaki Y 2020 Development of a new phantom simulating extracellular space of tumor cell growth and cell edema for diffusion-weighted magnetic resonance imaging *Magn. Reson. Mater. Phys. Biol. Med.* **33** 507–13
Mileto A, Barina A, Marin D, Stinnett S S, Choudhury K R, Wilson J M and Nelson R C 2016 Virtual monochromatic images from dual-energy multidetector CT: variance in CT numbers from the same lesion between single-source projection-based and dual-source image-based implementations *Radiology* **279** 269–77
Miloro P, Civale J, Rivens I and Shaw A 2016 The Feasibility of Thermal Imaging as a Future Portal Imaging Device for Therapeutic Ultrasound *Ultrasound Med. Biol.* **42** 2033–8
Mitsouras D, Lee T C, Liacouras P, Ionita C N, Pietilla T, Maier S E and Mulkern R V 2016 Three-dimensional printing of MRI-visible phantoms and MR image-guided therapy simulation *Magn. Reson. Med.* **622** 613–22
Mix D S, Stoner M C, Day S W and Richards M S 2018 Manufacturing abdominal aorta hydrogel tissue-mimicking phantoms for ultrasound elastography validation *J. Vis. Exp.* **19** 57984
Mohammed Ali A, Hogg P, Johansen S and England A 2018 Construction and validation of a low cost paediatric pelvis phantom *Eur. J. Radiol.* **108** 84–91
Mouratidis P X E, Rivens I and Ter Haar G 2015 A study of thermal dose-induced autophagy, apoptosis and necroptosis in colon cancer cells *Int. J. Hyperth.* **31** 476–88
Napoli A, Scipione R, Anzidei M, Andrani F, Dababou S and Catalano C 2017 Uterine fibroids treated with MRI-guided high-intensity focused ultrasound (MRgFUS): clinical outcomes in comparison to current therapeutic strategies *European Congress of Radiology 2017*
Negus I S, Holmes R B, Jordan K C, Nash D A, Thorne G C and Saunders M 2016 Technical Note: development of a 3D printed subresolution sandwich phantom for validation of brain SPECT analysis *Med. Phys.* **43** 5020–7
Negussie A H, Partanen A, Mikhail A S, Xu S, Abi-Jaoudeh N, Maruvada S and Wood B J 2016 Thermochromic tissue-mimicking phantom for optimisation of thermal tumour ablation *Int. J. Hyperth.* **32** 239–43
NEMA. 2007. National Electrical Manufacturers Association Standards Publication NU 2-2007, Performance measurements of positron emission tomographs
Neumann W, Pusch T P, Siegfarth M, Schad L R and Stallkamp J L 2019 CT and MRI compatibility of flexible 3D-printed materials for soft actuators and robots used in image-guided interventions *Med. Phys.* **46** 5488–98
Niebuhr N I, Johnen W, Echner G, Runz A, Bach M, Stoll M, Giske K, Greilich S and Pfaffenberger A 2019 The ADAM-pelvis phantom - An anthropomorphic, deformable and multimodal phantom for MRgRT *Phys. Med. Biol.* **64** 04NT05
Niebuhr N I, Johnen W, Güldaglar T, Runz A, Echner G, Mann P, Möhler C, Pfaffenberger A, Jäkel O and Greilich S 2016 Technical Note: radiological properties of tissue surrogates used in a multimodality deformable pelvic phantom for MR-guided radiotherapy *Med. Phys.* **43** 908–16
Nute J L, Jacobsen M C, Stefan W, Wei W and Cody D D 2019 Development of a dual-energy computed tomography quality control program: characterization of scanner response and definition of relevant parameters for a fast-kVp switching dual-energy computed tomography system *Med. Phys.* **45** 1444–58
O'Doherty J *et al* 2017 Feasibility of simultaneous PET-MR perfusion using a novel cardiac perfusion phantom *Eur. J. Hybrid Imaging* **1** 4
O'Neill F, Condon F, Mcgloughlin T, Lenehan B, Coffey C and Walsh M 2012 Validity of synthetic bone as a substitute for osteoporotic cadaveric femoral heads in mechanical testing *Bone Jt. Res.* **1** 50–55
Oglat A A, Suardi N, Matjafri M Z, Oqlat M A, Abdelrahman M A and Oqlat A A 2018 A review of suspension-scattered particles used in blood-mimicking fluid for Doppler ultrasound imaging *J. Med. Ultrasound* **26** 68–76
Oudry J, Bastard C, Miette V, Willinger R and Sandrin L 2009 Copolymer-in-oil phantom materials for elastography *Ultrasound Med. Biol.* **35** 1185–97
Owrangi A M, Greer P B and Glide-Hurst C K 2018 MRI-only treatment planning: benefits and challenges *Phys. Med. Biol.* **63** 05TR01
Pallotta S, Calusi S, Foggi L, Lisci R, Masi L, Marrazzo L, Talamonti C, Livi L and Simontacchi G 2018 ADAM: a breathing phantom for lung SBRT quality assurance *Phys. Med.* **49** 147–55

Papadakis A E, Perisinakis K and Damilakis J 2020 The effect of heart rate, vessel angulation and acquisition protocol on the estimation accuracy of calcified artery stenosis in dual energy cardiac CT: a phantom study *Phys. Med.* **70** 208–15
Pappas E P, Kalaitzakis G, Boursianis T, Zoros E, Zourari K, Pappas E P, Makris D, Seimenis I, Efstathopoulos E and Maris T G 2019 Dosimetric performance of the Elekta Unity MR-linac system: 2D and 3D dosimetry in anthropomorphic inhomogeneous geometry *Phys. Med. Biol.* **64** 225009
Parker K J, Huang S R, Lerner R M, Lee F J, Rubens D and Roach D 1993 Elastic and ultrasonic properties of the prostate *1993 Proc. IEEE Ultrason. Symp* vol **2** 1035–1038
Pepley D F, Sonntag C C, Prabhu R S, Yovanoff M A, Han D C, Miller S R and Moore J Z 2018 Building ultrasound phantoms with modified polyvinyl chloride: a comparison of needle insertion forces and sonographic appearance with commercial and traditional simulation materials *Simul. Healthcare* **13** 149–53
Perrin R L *et al* 2017 An anthropomorphic breathing phantom of the thorax for testing new motion mitigation techniques for pencil beam scanning proton therapy *Phys. Med. Biol.* **62** 2486–504
Plautz T E, Zheng C, Noid G and Li X A 2019 Time stability of delta-radiomics features and the impact on patient analysis in longitudinal CT images *Med. Phys.* **46** 1663–76
Pogue B W and Patterson M S 2006 Review of tissue simulating phantoms for optical spectroscopy, imaging and dosimetry *J. Biomed. Opt.* **11** 041102
Price P, Sikora K and Illidge T 2008 *Treatment of Cancer. Fith Edition/Matematical Modelling and Its Aplication in oncology/RG Dale* (London: CRC Press)
Quadri S A, Waqas M, Khan I, Khan M A, Suriya S S, Farooqui M and Fiani B 2018 High-intensity focused ultrasound: past, present, and future in neurosurgery *Neurosurg. Focus* **44** E16
Rai R, Holloway L C, Brink C, Field M, Christiansen R L, Sun Y, Barton M B and Liney G P 2020 Multicentre evaluation of MRI-based radiomics features: a phantom study *Med. Phys.* **47** 3054–63
Rai R, Manton D, Jameson M G, Josan S, Barton M B, Holloway L C and Liney G P 2018 3D printed phantoms mimicking cortical bone for the assessment of ultrashort echo time magnetic resonance imaging *Med. Phys.* **45** 758–66
Rai R, Wang Y F, Manton D, Dong B, Deshpande S and Liney G P 2019 Development of multi-purpose 3D printed phantoms for MRI *Phys. Med. Biol.* **64** 075010
Rajagopal S, Sadhoo N and Zeqiri B 2015 Reference characterisation of sound speed and attenuation of the IEC agar-based tissue-mimicking material up to a frequency of 60 MHz *Ultrasound Med. Biol.* **41** 317–33
Rakow-Penner R, Daniel B, Yu H, Sawyer-Glover A and Glover G H 2006 Relaxation times of breast tissue at 1.5 T and 3T measured using IDEAL *J. Magn. Reson. Imaging* **23** 87–91
Ramnarine K V, Anderson T and Hoskins P R 2001 Construction and geometric stability of physiological flow rate wall-less stenosis phantoms *Ultrasound Med. Biol.* **27** 245–50
Ramnarine K V, Nassiri D K, Hoskins P R and Lubbers J 1998 Validation of a new blood-mimicking fluid for use in Doppler flow test objects *Ultrasound Med. Biol.* **24** 451–9
Reichert I L H, Robson M D, Gatehouse P D, He T, Chappell K E, Holmes J, Girgis S and Bydder G M 2005 Magnetic resonance imaging of cortical bone with ultrashort TE pulse sequences *Magn. Reson. Imaging* **23** 611–8
Rieke V and Butts Pauly K 2008 Echo combination to reduce proton resonance frequency (PRF) thermometry errors from fat *J. Magn. Reson. Imaging* **27** 673–7
Riel L-P, Dion S, Brouillette M, Bérubé S, Despatis M-A and Bousser É 2014 Characterization of calcified plaques retrieved from occluded arteries and comparison with potential artificial analogues *ASME 2014 Int. Mechanical Engineering Congress and Exposition* pp 1–11
Robinson C G, Samson P P, Moore K M S, Hugo G D, Knutson N, Mutic S, Goddu S M, Lang A, Cooper D H and Faddis M 2019 Phase I/II trial of electrophysiology-guided noninvasive cardiac radioablation for ventricular tachycardia *Circulation* **139** 313–21
Robinson A P *et al* 2016 Organ-specific SPECT activity calibration using 3D printed phantoms for molecular radiotherapy dosimetry *EJNMMI Physics* **3** 1–11
Rodrigues D B, Stauffer P R, Vrba D and Hurwitz M D 2015 Focused ultrasound for treatment of bone tumours *Int. J. Hyperth.* **31** 260–71
Rodríguez G P, Arenas A C, Hernández R A M, Stolik S, Orea A C and Sinencio F S 2002 Measurement of thermal diffusivity of bone, hydroxyapatite and metals for biomedical application *Analytical Sciences/Supplements Proc. 11th Int. Conf. of Photoacoustic and Photothermal Phenomena* (The Japan Society for Analytical Chemistry) pp s357–60
Rooney W D, Johnson G, Li X, Cohen E R, Kim S, Ugurbil K and Springer Jr C S 2007 Magnetic field and tissue dependencies of human brain longitudinal 1H2O relaxation in vivo *Magn. Reson. Med.* **57** 308–18
Rossman A H, Catenacci M, Zhao C, Sikaria D, Knudsen J E, Dawes D, Gehm M E, Samei E, Wiley B J and Lo J Y 2019 Three-dimensionally-printed anthropomorphic physical phantom for mammography and digital breast tomosynthesis with custom materials, lesions, and uniform quality control region *J. Med. Imaging* **6** 1
Rossmann C and Haemmerich D 2014 Review of temperature dependence of thermal properties, dielectric properties, and perfusion of biological tissues at hyperthermic and ablation temperatures *Crit. Rev. Biomed. Eng* **42** 467–92
Ruschin M, Davidson S R H, Phounsy W, Yoo T S, Chin L, Pignol J P, Ravi A and Mccann C 2016 Technical Note: multipurpose CT, ultrasound, and MRI breast phantom for use in radiotherapy and minimally invasive interventions *Med. Phys.* **43** 2508–14
Samavat H and Evans J A 2006 An ideal blood mimicking fluid for doppler ultrasound phantoms *J. Med. Phys.* **31** 275–8
Samei E *et al* 2019 Performance evaluation of computed tomography systems: Summary of AAPM Task Group 233 *Med. Phys.* **46** e735–e756
Sawbones 2016 Test materials and composite bones: biomechanical Product Catalog
Schoenfeld A A, Harder D, Poppe B and Chofor N 2015 Water equivalent phantom materials for 192Ir brachytherapy *Phys. Med. Biol.* **60** 9403–20
Schoenfeld A A, Thieben M, Harder D, Poppe B and Chofor N 2017 Evaluation of water-mimicking solid phantom materials for use in HDR and LDR brachytherapy dosimetry *Phys. Med. Biol.* **62** N561–72
Schoenfeld C M, Lautenschlager E P and Meyer P R 1974 Mechanical properties of human cancellous bone in the femoral head *Med. Biol. Eng.* **12** 313–7
Schopphoven S, Cavael P, Bock K, Fiebich M and Mäder U 2019 Breast phantoms for 2D digital mammography with realistic anatomical structures and attenuation characteristics based on clinical images using 3D printing *Phys. Med. Biol.* **64** 215005
Schreiber J J, Anderson P A, Rosas H G, Buchholz A L and Au A G 2011 Hounsfield units for assessing bone mineral density and strength: a tool for osteoporosis management *J. Bone Jt. Surg. Ser.* A **93** 1057–63

Seco J, Clasie B and Partridge M 2014 Review on the characteristics of radiation detectors for dosimetry and imaging *Phys. Med. Biol.* **59** R303–47
Seco J and Evans P M 2006 Assessing the effect of electron density in photon dose calculations *Med. Phys.* **33** 540–52
Shieh J, Chen S-R, Chen G-S, Lo C-W, Chen C-S, Chen B-T, Sun M-K, Huang C-W and Chen W-S 2014 Acrylic acid controlled reusable temperature-sensitive hydrogel phantoms for thermal ablation therapy *Appl. Therm. Eng.* **62** 322–9
Shin D S, Kang S H, Kim K H, Kim T H, Kim D S, Chung J B, Lucero S A, Suh T S and Yamamoto T 2020 Development of a deformable lung phantom with 3D-printed flexible airways *Med. Phys.* **47** 898–908
Simutec 2018 Dynamic multimodality heart phantoms
Singhrao K, Fu J, Wu H, Hu P, Kishan A U, Chin R K and Lewis J H 2020a A novel anthropomorphic multimodality phantom for MRI-based radiotherapy quality assurance testing *Med. Phys.* **47** 1443–51
Singhrao K, Ruan D, Fu J, Gao Y, Chee G, Yang Y, King C R, Hu P, Kishan A U and Lewis J H 2020b Quantification of fiducial marker visibility for MRI-only prostate radiotherapy simulation *Phys. Med. Biol.* **65** 1–46
Sirtoli V G, Morcelles K and Bertemes-Filho P 2017 Electrical properties of phantoms for mimicking breast tissue *2017: 39th Annual Int. Conf. of the IEEE Engineering in Medicine and Biology Society (EMBC)* (IEEE) pp 157–60
Snedeker J G, Niederer P, Schmidlin F R, Farshad M, Demetropoulos C K, Lee J B and Yang K H 2005 Strain-rate dependent material properties of the porcine and human kidney capsule *J. Biomech.* **38** 1011–21
Snyder W S, Cook M, Nasset E, Karhausen L, Howells G P and Tipton I 1975 ICRP Publication 23: report of the task group on reference man *Elmsford, NY Int. Comm. Radiol. Prot.* 97–200
Solc J, Vrba T and Burianova L 2018 Tissue-equivalence of 3D-printed plastics for medical phantoms in radiology *J. Instrum.* **13** 09018
Steidl P, Richter D, Schuy C, Schubert E, Haberer T, Durante M and Bert C 2012 A breathing thorax phantom with independently programmable 6D tumour motion for dosimetric measurements in radiation therapy *Phys. Med. Biol.* **57** 2235
Steinmann A, Alvarez P, Lee H, Court L, Stafford R, Sawakuchi G, Wen Z, Fuller C and Followill D 2019a MRIgRT dynamic lung motion thorax anthropomorphic QA phantom: design, development, reproducibility, and feasibility study *Med. Phys.* **46** 5124–33
Steinmann A, Alvarez P, Lee H, Court L, Stafford R, Sawakuchi G, Wen Z, Fuller C D and Followill D 2020 MRIgRT head and neck anthropomorphic QA phantom: design, development, reproducibility, and feasibility study *Med. Phys.* **47** 604–13
Steinmann A, O'Brien D, Stafford R, Sawakuchi G, Wen Z, Court L, Fuller C and Followill D 2019b Investigation of TLD and EBT3 performance under the presence of 1.5T, 0.35T, and 0T magnetic field strengths in MR/CT visible materials *Med. Phys.* **46** 3217–26
Steinmann A, Stafford R J, Sawakuchi G, Wen Z, Court L, Fuller C D and Followill D 2018 Developing and characterizing MR/CT-visible materials used in QA phantoms for MRgRT systems *Med. Phys.* **45** 773–82
Sun C *et al* 2012 The speed of sound and attenuation of an IEC agar-based tissue-mimicking material for high frequency ultrasound applications *Ultrasound Med. Biol.* **38** 1262–70
Surry K J M, Austin H J B, Fenster A and Peters T M 2004 Poly(vinyl alcohol) cryogel phantoms for use in ultrasound and MR imaging *Phys. Med. Biol.* **49** 5529–46
Tai B L, Kao Y T, Payne N, Zheng Y, Chen L and Shih A J 2018 3D printed composite for simulating thermal and mechanical responses of the cortical bone in orthopaedic surgery *Med. Eng. Phys.* **61** 61–68
Tai B L, Rooney D, Stephenson F, Liao P S, Sagher O, Shih A J and Savastano L E 2015 Development of a 3D-printed external ventricular drain placement simulator: technical note *J. Neurosurg.* **123** 1070–6
Tai B L, Wang A C, Joseph J R, Wang P I, Sullivan S E, Mckean E L, Shih A J and Rooney D M 2016 A physical simulator for endoscopic endonasal drilling techniques: technical note *J. Neurosurg.* **124** 811–6
Tan Z, Dini D, Rodriguez y Baena F and Forte A E 2018 Composite hydrogel: a high fidelity soft tissue mimic for surgery *Mater. Des.* **160** 886–94
Tan Z, Parisi C, Di Silvio L, Dini D and Forte A E 2017 Cryogenic 3D printing of super soft hydrogels *Sci. Rep.* **7** 1–11
Tanaka K, Yoshida T, Sato K, Kondo T, Yasukawa K, Miyamoto N and Taniguchi M 2012 Blood-mimicking fluid for testing ultrasonic diagnostic instrument *Jpn. J. Appl. Phys.* **51** 07GF18
Tavakoli V, Negahdar M J, Kendrick M, Alshaher M, Stoddard M and Amini A A 2012 A biventricular multimodal (MRI/ultrasound) cardiac phantom *Proc. Annu. Int. Conf. IEEE Eng. Med. Biol. Soc. EMBS* pp 3187–90
Taylor J C, Vennart N, Negus I, Holmes R, Bandmann O, Lo C and Fenner J 2018 The subresolution DaTSCAN phantom: a cost-effective, flexible alternative to traditional phantom technology *Nucl. Med. Commun.* **39** 268–75
Taylor M L, Smith R L, Dossing F and Franich R D 2012 Robust calculation of effective atomic numbers: the Auto-Z_{eff} software *Med. Phys.* **39** 1769–78
Taylor P A, S F K R Y, Alvarez P, Keith T, Lujano C, Hernandez N and Followill D S 2016 Results from iroc houston's anthropomorphic proton phantoms used for clinical trial credentialing *Int. J. Radiat. Oncol. Biol. Phys.* **95** 242
Taylor Z and Miller K 2004 Reassessment of brain elasticity for analysis of biomechanisms of hydrocephalus *J. Biomech.* **37** 1263–9
Technical Committee EPL/87 Ultrasonics 1995 BS EN 61206:1995 IEC 1206:1993 Ultrasonics — continuous-wave Doppler systems — test procedures
Technical Committee EPL/87 Ultrasonics 2001 BS EN 61685:2002 IEC 61685:2001 Ultrasonics - Flow measurement systems - Flow test object
Technical Committee EPL/87 Ultrasonics 2019 IEC TS 63081:2019 Ultrasonics – methods for the characterization of the ultrasonic properties of materials
Teirlinck C J, Bezemer R A, Kollmann C, Lubbers J, Hoskins P R, Ramnarine K V, Fish P, Fredeldt K E and Schaarschmidt U G 1998 Development of an example flow test object and comparison of five of these test objects, constructed in various laboratories *Ultrasonics* **36** 653–60
Thali M, Dirnhofer R and Vock P 2009 *The Virtopsy Approach: 3D Optical and Radiological Scanning and Reconstruction in Forensic Medicine* (Boca Raton, FL: CRC Press)
Thipayawat T, Minh D N, Prinable J, Mcewan A and Barry T 2019 Experimental validation of the multiphysics modelling of radiofrequency ablation using physical phantom *Proc. Annu. Int. Conf. IEEE Eng. Med. Biol. Soc. EMBS* pp 154–7
Thomas K, Thomas W, Faouzi K, Brian G and Timothy H 1998 Elastic moduli of breast and prostate tissues under compression *Ultrason. Imaging* **20** 260–74
Thomas S J 1999 Relative electron density calibration of CT scanners for radiotherapy treatment planning *Br. J. Radiol.* **72** 781–6
Tino R, Leary M, Yeo A, Brandt M and Kron T 2019a Gyroid structures for 3D-printed heterogeneous radiotherapy phantoms *Phys. Med. Biol.* **64** 21NT05
Tino R, Yeo A, Leary M, Brandt M and Kron T 2019b A systematic review on 3D-Printed imaging and dosimetry phantoms in radiation therapy *Technol. Cancer Res. Treat.* **18** 1–14

Tuong B and Gardiner I 2013 Development of a novel breast MRI phantom for quality control *Am. J. Roentgenol.* **201** 511–5
Ueguchi T, Ogihara R and Yamada S 2018 Accuracy of dual-energy virtual monochromatic CT numbers: comparison between the single-source projection-based and dual-source image-based methods *Acad. Radiol.* **25** 1632–9
Umale S, Deck C, Bourdet N, Dhumane P, Soler L, Marescaux J and Willinger R 2013 Experimental mechanical characterization of abdominal organs: liver, kidney & spleen *J. Mech. Behav. Biomed. Mater.* **17** 22–33
Valladares A *et al* 2019 Clinically valuable quality control for PET/MRI systems: consensus recommendation from the HYBRID Consortium *Front. Phys.* **7** 136
Valladares A, Beyer T and Rausch I 2020 Physical imaging phantoms for simulation of tumor heterogeneity in PET, CT, and MRI: an overview of existing designs *Med. Phys.* **7** 2023–37
Veltmann C, Lohmaier S, Schlosser T, Shai S, Ehlgen A L, Pohl C, Becher H and Tiemann K 2002 Original contribution evaluation of ultrasound contrast agents at very low flow velocities *Ultrasound Med. Biol.* **28** 625–34
Vidal F, El Mansouri O, Kouamé D and Basarab A 2019 On the design of a pelvic phantom for magentic resononance and utltrasound image fusion *2019 IEEE Int. Ultrasonics Symp. (IUS)* (IEEE) pp 2400–3
Vieira S L, Pavan T Z, Junior J E and Carneiro A A O 2013 Paraffin-gel tissue-mimicking material for ultrasound-guided needle biopsy phantom *Ultrasound Med. Biol.* **39** 2477–84
Vogt W C, Pfefer T J, Jia C, Wear K and Garra B 2017 Patent Application Publication PVCP Phantoms and their use
Vogt W C, Wear K A, Garra B S and Pfefer T J 2016 Biologically relevant photoacoustic imaging phantoms with tunable optical and acoustic properties phantoms with tunable optical and acoustic properties *J. Biomed. Opt.* **21** 101405/1–101405/11
Vrana N E, Yurong L, Mcguinness G B and Cahill P A 2008 Characterization of poly(vinyl alcohol)/Chitosan hydrogels as vascular tissue engineering scaffolds *Macromol. Symp*. Vol **269** pp 106–10
Walter W R, Burke C J, Diallo M and Adler R S 2018 Use of a simple, inexpensive dual-modality phantom as a learning tool for magnetic resonance imaging–ultrasound fusion techniques *J. Ultrasound Med.* **37** 2083–9
Wang Y, Tai B L, Yu H and Shih A J 2014 Silicone-based tissue-mimicking phantom for needle insertion simulation *J. Med. Device.* **8** 021001
Wang Y, Zhang P, Zhang R and An P 2019 Predictive value of quantitative uterine fibroid perfusion parameters from contrast-enhanced ultrasound for the therapeutic effect of high-intensity focused ultrasound ablation *J. Ultrasound Med.* **38** 1511–7
Wapler M C, Leupold J, Dragonu I, Von Elverfeld D, Zaitsev M and Wallrabe U 2014 Magnetic properties of materials for MR engineering, micro-MR and beyond *J. Magn. Reson.* **242** 233–42
Wear K A *et al* 2005 Interlaboratory comparison of ultrasonic backscatter coefficient measurements from 2 to 9 MHz *J. Ultrasound Med.* **24** 1235–50
Weir A J, Sayer R, Wang C and Parks S 2015 A wall-less poly(vinyl alcohol) cryogel flow phantom with accurate scattering properties for transcranial Doppler ultrasound propagation channels analysis *2015: 37th Annual Int. Conf. of the IEEE Engineering in Medicine and Biology Society (EMBC)* pp 2709–12
Wesolowska P, Georg D, Lechner W, Kazantsev P, Bokulic T, Tedgren A C, Adolfsson E, Campos A M, Alves V G L and Suming L 2019 Testing the methodology for a dosimetric end-to-end audit of IMRT/VMAT: results of IAEA multicentre and national studies *Acta Oncol. (Madr)* **58** 1731–9
White D R, Booz J, Griffith R V, Spokas J J and Wilson I J 1989 Report 44 *J. Int. Comm. Radiat. Units Meas.* **os23** NP–NP
White D R, Griffith R V and Wilson I J 1992 Report 46 *J. Int. Comm. Radiat. Units Meas.* **os24** NP
White D R, Martin R J and Darlison R 1977 Epoxy resin based tissue substitutes *Br. J. Radiol.* **50** 814–21
Wood S, Krishnamurthy N, Santini T, Raval S, Farhat N, Holmes J A and Ibrahim T S 2017 Design and fabrication of a realistic anthropomorphic heterogeneous head phantom for MR purposes *PloS One* **12** 1–16
Woodard H Q and White D R 1986 The composition of body tissues *Br. J. Radiol.* **59** 1209–18
Xu X G 2014 An exponential growth of computational phantom research in radiation protection, imaging, and radiotherapy: a review of the fifty-year history *Phys. Med. Biol.* **59** R233
Yamashiro A, Kobayashi M and Saito T 2019 Cerebrospinal fluid T1 value phantom reproduction at scan room temperature *J. Appl. Clin. Med. Phys.* **20** 166–75
Yea J W, Park J W, Kim S K, Kim D Y, Kim J G, Seo C Y, Jeong W H, Jeong M Y and Oh S A 2017 Feasibility of a 3D-printed anthropomorphic patient-specific head phantom for patient-specific quality assurance of intensity-modulated radiotherapy *PloS One* **12** 1–10
Yeh W C, Li P C, Jeng Y M, Hsu H C, Kuo P L, Li M L, Yang P M and Po H L 2002 Elastic modulus measurements of human liver and correlation with pathology *Ultrasound Med. Biol.* **28** 467–74
Yohannes I, Kolditz D, Langner O and Kalender W A 2012 A formulation of tissue- and water-equivalent materials using the stoichiometric analysis method for CT-number calibration in radiotherapy treatment planning *Phys. Med. Biol.* **57** 1173–90
Yuan Y, Wyatt C, Maccarini P, Stauffer P, Craciunescu O, Macfall J, Dewhirst M and Das S K 2012 A heterogeneous human tissue mimicking phantom for RF heating and MRI thermal monitoring verification *Phys. Med. Biol.* **57** 2021–37
Yunker B E, Cordes D, Scherzinger A L, Dodd G D, Shandas R, Feng Y and Hunter K S 2013 An investigation of industrial molding compounds for use in 3D ultrasound, MRI, and CT imaging phantoms *Med. Phys.* **40** 1–9
Zeqiri B, Cook A, Rétat L, Civale J and Ter Haar G 2015 On measurement of the acoustic nonlinearity parameter using the finite amplitude insertion substitution (FAIS) technique *Metrologia* **52** 406–22
Zeqiri B, Scholl W and Robinson S P 2010 Measurement and testing of the acoustic properties of materials: a review *Metrologia* **47** S156–S171
Zhang F, Zhang H, Zhao H, He Z, Shi L, He Y, Ju N, Rong Y and Qiu J 2019 Design and fabrication of a personalized anthropomorphic phantom using 3D printing and tissue equivalent materials *Quant. Imaging Med. Surg.* **9** 94–100
Zimmerman B E and Cessna J T 2010 Development of a traceable calibration methodology for solid 68Ge/68Ga sources used as a calibration surrogate for 18F in radionuclide activity calibrators *J. Nucl. Med.* **51** 448–53
Zimmerman B E, Pibida L, King L E, Bergeron D E, Cessna J T and Mille M M 2013 Calibration of traceable solid mock 131I phantoms used in an international SPECT image quantification comparison *J. Res. Natl. Inst. Stand. Technol.* **118** 359
Zimmerman B E, Pibida L, King L E, Bergeron D E, Cessna J T and Mille M M 2014 Development of a calibration methodology for large-volume, solid 68Ge phantoms for traceable measurements in positron emission tomography *Appl. Radiat. Isot.* **87** 5–9
Zwirner J, Scholze M, Waddell J N, Ondruschka B and Hammer N 2019 Mechanical properties of human dura mater in tension – an analysis at an age range of 2 to 94 years *Sci. Rep.* **9** 1–11